

Thesis for the degree of Licentiate of Technology
Sundsvall 2017

Measuring Water Droplets to Detect Atmospheric Icing

Staffan Rydblom

Supervisor: Professor Mattias O'Nils,
Associate Professor Benny Thörnberg

Department of Electronics Design, in the
Faculty of Science, Technology and Media
Mid Sweden University, SE-851 70 Sundsvall, Sweden

ISSN 1652-8948

ISBN 978-91-88527-29-5

Mid Sweden University Licentiate Thesis 134



Akademisk avhandling som med tillstånd av Mittuniversitetet i Sundsvall framläggs till offentlig för avläggande av licentiatexamen i elektronik **onsdagen den 1 november 2017, klockan 10.00** i sal **O102**, Mittuniversitetet Sundsvall. Seminariet kommer att hållas på engelska.

Measuring Water Droplets to Detect Atmospheric Icing

Staffan Rydbom

©Staffan Rydbom, 2017

Faculty of Science, Technology and Media, Mid Sweden University,
SE-851 70 Sundsvall Sweden

Telephone: +46 (0)60 148422

Printed by Mid Sweden University, Sundsvall, Sweden, 2017

For Sara, Alva and Ludvig.



ABSTRACT

This thesis describes the exploration of a method to measure the droplet size and the concentration of atmospheric liquid water. The purpose is to find a cost effective technique to detect the conditions for icing on structures.

Icing caused by freezing atmospheric water can be a significant problem for infrastructure such as power lines, roads and air traffic. About one third of the global installed wind power capacity is located in cold climates, where icing of rotor blades is one of the major challenges.

The icing process is complex and the result depends on a combination of the aerodynamic shape of the structure or airfoil, the velocity of the air and its contained water, the temperature, the mixing of snow and water, the concentration of liquid water and the Droplet Size Distribution (DSD).

The measurement method is based on a shadowgraph imaging system using light emitting diode (LED) light as background illumination and digital image processing. A prototype instrument has been constructed. The components were selected keeping the possibility of low-cost volume production in mind. The applications of a commercial instrument based on this technique are e.g. real-time in-situ icing condition measurements and assimilation and verification of data in numerical weather models.

The work presented shows that measurements of the size and concentration of water droplets using shadowgraph images can be used for the comparison and validation of Numerical Weather Prediction (NWP) models and other instruments. The accuracy of the particle size measurement is high. The accuracy of the concentration measurement has the potential to become high due to the single-particle measurement range calibraiton. The precision of the instrument depends mainly on the number of images that is used to find each measurement value. The real-time performance of the instrument is limited by the image retrieval and processing speed and depends on the precision required.

SAMMANFATTNING

Den här avhandlingen beskriver hur en metod för att mäta storlek och koncentration av vattendroppar i atmosfären. Målet är att hitta en kostnadseffektiv teknik som kan förutsäga isbildning.

Ibildning som orsakas av atmosfäriskt vatten kan vara ett allvarligt problem för infrastruktur som t.ex. kraftledningar, vägar och flygtrafik. Omkring en tredjedel av världens vindkraft finns i klimat som definieras som kalla, där nedisning av rotorbladen är en av de största utmaningarna.

Nedisningsprocessen är komplex och resultatet beror på en kombination av strukturen eller vingens aerodynamiska form, den förbi passerande luftens hastighet, luftens och ytans temperatur, eventuell blandning av snö och vatten, koncentrationen av flytande vatten och vattendropparnas storleksdistribution.

Den valda mätmetoden baseras på skuggfotografering med en LED som bakgrundsbelysning samt digital bildbehandling. Ett prototypinstrument har konstruerats med hjälp av kommersiellt tillgängliga komponenter. Valet av komponenter möjliggör låg produktionskostnad av en serieproducerad variant av detta instrument. Exempel på applikationer för ett kommersiellt instrument baserat på denna teknik är villkorssättning för nedisning i realtid samt assimilation och verifikation av data i numeriska vädermodeller.

Arbetet som presenteras visar att mätning av storlek och koncentration av vattendroppar med hjälp av skuggfotografering kan användas för validering av numeriska vädermodeller (NWP) och andra instrument. Noggrannheten hos storleksmätningen är hög. Noggrannheten av koncentrationsmätningen har potential att bli hög eftersom varje droppe får en individuellt kalibrerad mätvolym. Precisionen hos mätinstrumentet beror till största delen på hur många bilder och vattendroppar som används för att skapa varje mätvärde. Instrumentets prestanda för att mäta i realtid begränsas av kamerans bildhastighet och bildbehandlingstiden samt vilken mätvärdesprecision som önskas.

CONTENTS

ABSTRACT	v
SAMMANFATTNING	vii
CONTENTS	viii
LIST OF FIGURES	x
LIST OF TABLES	xiii
LIST OF PAPERS	xv
ACKNOWLEDGEMENTS	xvii
1 INTRODUCTION	1
1.1 Scientific Contribution	3
1.2 Atmospheric Water and Icing	3
1.3 Justification and Narrative	4
1.4 Related Work of Measurement	6
2 THEORY	9
2.1 Forming of Ice	9
2.2 Liquid Water Content and Median Volume Diameter	10
2.3 Practical Problems with Measuring Atmospheric Water	11
2.4 Light Scattering and Absorption	13
3 MATERIALS AND METHODS	15
3.1 The Shadowgraph System	15
3.2 Overview and Process	16
3.3 Image Segmentation	18
3.4 Light Source	22
3.5 Image Noise	23
3.6 Calibration and Validation of the Calibration	24

3.7	The Fog Chamber	27
3.8	The Klövsjö Installation	28
3.9	Numerical Weather Prediction	29
4	RESULTS	33
4.1	Measurement of Polymer Microspheres	33
4.2	Comparison of DII and CDP Data	34
4.3	Comparison of Measured and Modeled Data	38
5	DISCUSSION	43
5.1	Cause of Systematic Difference	43
5.2	Model Data	44
5.3	Starting Studies	44
5.4	Image Noise and SNR	47
5.5	Aerodynamics	48
5.6	Difficulties in the Polymer Microspheres Measurement	49
5.7	LED Illumination	51
5.8	Statistics	53
5.9	Droplet Size and Distributions	53
5.10	Icing	56
6	SUMMARY OF THE THESIS	59
6.1	Conclusions	59
6.2	Future Work	61
6.3	Authors' Contributions	62
	ACRONYMS	63
	BIBLIOGRAPHY	65

LIST OF FIGURES

1.1	The research work flow and the related research questions (RQ1 to RQ4).	2
2.1	Supercooled water droplets on collision course with an aerodynamic profile.	10
3.1	Principle of shadowgraphy. 1. Camera. 2. Telecentric lens. 3. Parallel focused light beam. 4. Collimating lens. 5. LED.	16
3.2	The experimental setup with a dot micrometer scale as test object mounted on a translation stage.	16
3.3	The illumination and detector is mounted inside two Bosch camera housings facing each other with heating inside the housings and on the front glass.	17
3.4	Electrical interfaces and system overview.	17
3.5	Flowchart illustrating the method of image processing step by step.	19
3.6	The same dot viewed with different background light: 455 nm (left) and 850 nm (right).	23
3.7	Calculation of the SNR. \bar{y}_j is determined by calculating the average of the darkest third of all pixels inside the edge detected dot.	24
3.8	Measuring range (mm) vs. diameter for two different thresholds (0.005 and 0.002).	25
3.9	The 50 micrometer dot with front illumination imaged using 40x magnifying lens.	26
3.10	Fog chamber with connected droplet generator (blue container) and a multimeter used for fan power measurement. A Beaglebone Black microcontroller (blue box) is used for fan speed regulation.	28
3.11	Installation in Klövsjö.	29
3.12	Ice and snow on the front side of the installed instruments. The CDP is more efficient at preventing ice.	30

3.13 Graphical presentation of data from the HARMONIE-AROME NWP covering Klövsjö and the surrounding mountains at a specific point in time using 500 m resolution. Yellow areas are where the model predicts an LWC more than $0.1 \text{ g} \cdot \text{kg}^{-1}$. (Grams of water per kg air.) Simulation and figure by SMHI.	31
4.1 Histograms of the four measured distributions. The dashed line is a fitted lognormal of the weighted distribution.	33
4.2 MVD minute values measured by the DII and the CDP for 46 hours on 28-02-2017–01-03-2017.	35
4.3 LWC measured by the DII and the CDP for 46 hours on 28-02-2017–01-03-2017.	36
4.4 Relation between the wind speed and the quote between the LWC measured by the CDP and the DII. The vertical scale is cropped at 1 and 100. 238 values are above 100 and 121 below 1 out of a total of 2760.	37
4.5 LWC and MVD measured by the DII and the CDP 11-12-2016. HARMONIE-AROME model data using 500 meter resolution.	39
4.6 LWC and MVD measured 03-02-2017–06-02-2017 by the DII. HARMONIE-AROME model data using 2.5 km resolution, stored every 60 minutes.	41
4.7 LWC and MVD measured by the DII and the CDP 10-02-2017. HARMONIE-AROME model data using 2.5 km resolution, stored every 60 minutes.	42
5.1 Reflections and interference patterns by droplets in 450nm laser light. The light source is placed at a position about 135 degrees from the optical center.	46
5.2 Mean pixel value and standard deviation of ambient for a light measurement at 22000 lux.	47
5.3 SNR for a ten micrometer dot image using two wavelengths and seven gain level settings. Shorter wavelength and lower gain gives less noise.	48

List of Figures

5.4 An example showing an image of clogs of five micrometer microspheres. One of the clogs are measured as a single particle, since it is round enough for the roundness qualifying criteria.	49
5.5 Difference between an ice particle and a water droplet that is 62 μm in diameter. Larger ice and snow particles tend to be more complex in shape. Ice particles smaller than 10 μm in diameter may be difficult to distinguish from water droplets.	51
5.6 Spectrum of the Mightex 455nm LED using two different driving currents. The band width is slightly wider for the higher current.	52
5.7 A 74 μm droplet detected at 04:41 on 05-02-2017.	56
5.8 Two droplets, 19 and 62 μm in diameter detected in the same image at 16:48 on 05-02-2017.	56

LIST OF TABLES

3.1	Micro dot verification measurement. All values are in μm . Here, eccentricity is the maximum difference in μm between the smallest and the largest measured diameter.	27
4.1	Summary of the result from the measurement of NIST certified microspheres. All values are in μm .	34
6.1	Authors' contributions per article. MA = Main Author, CA = Co-Author, PM = Project Member, LR = Language Review.	62

LIST OF PAPERS

This thesis is based on the following papers, herein referred to by their Roman numerals:

PAPER I

- Liquid Water Content and Droplet Sizing Shadowgraph Measuring System for Wind Turbine Icing Detection
S. Rydblom, B. Thörnberg, IEEE Sensors Journal, 2015 73

PAPER II

- Droplet Imaging Instrument - Metrology Instrument for Icing Condition Detection
S. Rydblom, B. Thörnberg, IEEE International Conference on Imaging Systems and Techniques (IST) Proceedings, 2016 . . 87

PAPER III

- Comparative Field Study of LWC and MVD using two Droplet Measuring Instruments and an NWP Model
S. Rydblom, B. Thörnberg, E. Olsson, Under Review for Cold Regions Science and Technology, 2017 95

ACKNOWLEDGEMENTS

I would like to express the greatest gratitude to my supervisor, Benny Thörnberg, for his trust and encouragement especially when things did not turn out the way they were expected. I would also like to thank Mattias O'Nils and Claes Mattsson at the Department of Electronics Design for making the project possible and giving me the possibility to finish the thesis.

I owe a big thanks to the Swedish Energy Agency for funding most of the work; Patrik Jonsson, Björn Ollars and Olof Carlsson at Combitech for their work with integration of the rotating mast and the CDP; and Esbjörn Olsson at SMHI for sharing his knowledge about the weather physics and his work with the NWP model data.

To my wonderful family; the greatest love and gratitude that have sacrificed a lot and supported me in beginning, fulfilling and finishing this work. Without you this would not have been possible.

Special thanks to Lotta Frisk, Fanny Burman, Carolina Blomberg, Christine Grafström and Maria Rumm for all the administrative work, inspiration and positive energy at the Department of Electronics Design.

Not forgetting my mentor Magnus Engholm, Vincent Skerved, Göran Tungström, Börje Norlin, David Kraphol, Kent Bertilsson, Henrik Andersson, Javier Brugés, Najeem Lawal, Igor Fedorov, Irida Shalhari, Anwar Qaiser, Krister Aldén, Muhammad Imran, Hiba Alqaysi, Cristian Giménez, Sebastian Bader, Jan Thim, Enkeleda Balliu, Muhammad Abu Bakar, Amir Yousuf, Johan Sidén and everyone else at the Mid Sweden University that I forgot to mention. Finally big thanks to Lisa Velander for doing the language review.

— Chapter 1 —

INTRODUCTION

This thesis describes the exploration of a method to detect the conditions for icing on structures. The research target was to find a reliable and cost effective method to directly measure the size and concentration of atmospheric liquid water droplets, described by Liquid Water Content (LWC) and Median Volume Diameter (MVD), using advanced image sensors.

The chosen measurement method is based on digital image processing and a shadowgraph imaging system using a LED as background illumination. A prototype instrument was manufactured; components were selected to facilitate low-cost volume production. The applications of a commercial instrument based on this technique are e.g. real-time in-situ icing condition measurements and assimilation and verification of data in numerical weather models.

Main research questions:

- RQ1 How can the size of water droplets and their concentration be measured effectively?
- RQ2 Can the method be applied in a cost-effective instrument that meets relevant environmental and real-time requirements? How should this instrument be made physically and which components should be used?
- RQ3 How can the instrument be tested and its function verified in a laboratory environment?
- RQ4 How can the measured LWC and MVD be compared and verified in field? What difference will there be using the different methods and/or instruments?
- RQ5 Can the developed instrument be used for prediction of icing?

The research work flow is shown in Figure 1.1. RQ1-RQ4 can be answered by the work described in this thesis. To fully answer research question RQ5, a new measurement should be done by measuring

Chapter 1. Introduction

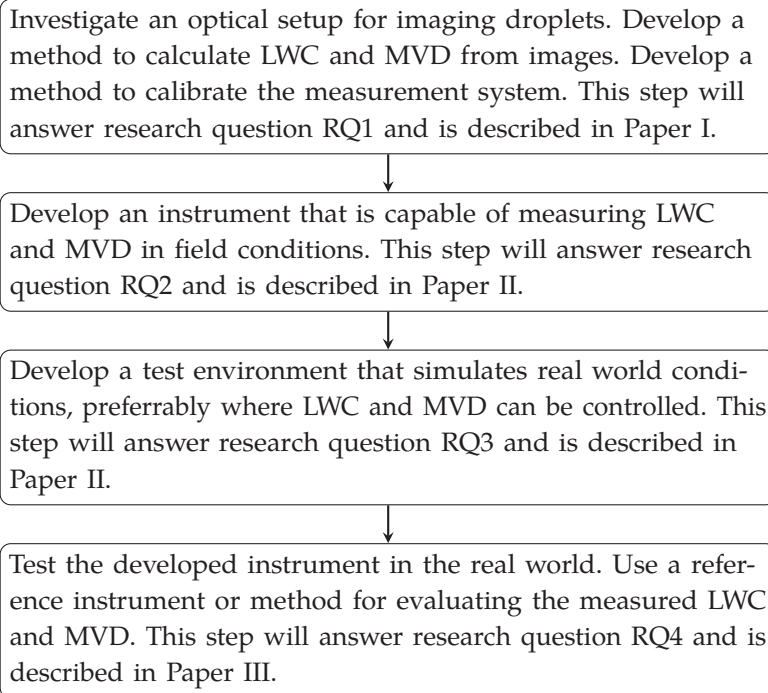


Figure 1.1: The research work flow and the related research questions (RQ1 to RQ4).

LWC and MVD in combination with sensors capable of detecting ice on structures in real world conditions.

Paper I describes a shadowgraph system that uses edge detection to define a measurement range depending on the size of a particle and the image signal to noise ratio (SNR). Paper II describes the size measurement method, an evaluation of the instrument's physical design with weather protection and a measurement of LWC and the MVD in a purpose-built fog chamber. Paper III describes a verification of the size measurement using polymer microspheres in calibrated distributions traceable from the National Institute of Standards and Technology (NIST) and a field study of LWC and MVD close to the ground using the Droplet Imaging Instrument (DII) and a comparative study using the Cloud Droplet Probe (CDP).

1.1 Scientific Contribution

The attached papers describe in detail the method of measuring LWC and MVD. They also describe the design, construction and validation of the weather protected instrument based on the developed method. The calculation of concentration is based on a particle-by-particle estimation of the measurement volume.

A comparison is made between the measured values of LWC and MVD, and the values predicted by a state of the art NWP model.

1.2 Atmospheric Water and Icing

Measuring or controlling the properties of a fog of water droplets has been of interest and the focus of many studies for at least half a century. Applications can be found in a variety of fields, such as atmospheric studies, aircraft and road traffic safety, medicin, infrastructure, and military. When a mass of air is saturated with water vapour the abundant water will be in either liquid or solid form. In order for water to freeze, or change from liquid to solid state, it needs to be below zero degrees Celsius at the standard atmospheric pressure (273.15 K at 101.325 kPa). For an ice crystal to form in the atmosphere, unless the temperature is below -40°C, the presence of an ice nucleus is also required. If no ice nucleus is present, the water droplet will remain liquid but supercooled. In this state, the water freezes very quickly when it comes in contact with a cold surface. The icing is called in-cloud icing, freezing rain or wet snow icing, depending on the size of the droplets. Combinations of these weather conditions are common.

Icing caused by freezing atmospheric water can be a critical problem in cold climates, affecting infrastructure such as wind turbines, power lines, road and air traffic. With the increasing importance of electric power generated by wind, there is a demand for predictions of icing on wind turbines. Icing on the blades of a turbine lowers the efficiency, increases noise and may force the turbine to a complete stop [14, 20, 29, 32]. Aircraft, power lines, as well as any other weather exposed structure, share this problem. Efforts have been made to create models for how the ice is formed [47, 49, 61] and how it can be

included in weather prediction models [64, 39]. The severity of the icing depends on many factors, e.g. the duration, the shape and surface of the structure, the wind speed, the atmospheric concentration of liquid water, the DSD and the mix of ice and snow [39, 47, 49, 28, 25]. Of particular interest for the prediction of effect loss on a wind turbine is the phase of ice accretion [15].

The Liquid Water Content (LWC) in atmospheric studies is usually given in either $\text{g} \cdot \text{m}^{-3}$ [59] or as the mass quote of water and air $\text{g} \cdot \text{kg}^{-1}$. The DSD when considering the collision efficiency is most effectively estimated by the Median Volume Diameter (MVD) [21]. The MVD is the point in the DSD where half of the total amount of water in the DSD is above the diameter, while the other half is below. Weather models today include the LWC and the MVD, making it possible to estimate the risk of icing based on general weather data [64]. The LWC and the MVD at ground level greatly depends on the local geographical topology, and measurements using in situ instruments are quite rare. There have been attempts to verify NWP models using in-situ data [5]. The LWC and the MVD can be estimated by analyzing satellite or radar images, but a precise estimation of the DSD based on radar reflectivity is difficult. The difficulty is partly explained by DSD modelling errors, but also by errors originating from the in-situ measurement probes currently used for verification of the models [52].

In-situ measurements are rarely simple or straightforward, especially considering the occurrence of the mixed conditions mentioned. Despite the development of various measurement techniques and instruments, in-situ measurements are still quite rare. Some instruments are expensive and most instruments require installation expertise, maintenance and periodic calibrations. The result from this thesis shows that LWC and MVD can be accurately measured by a cost effective instrument for in-situ measurements.

1.3 Justification and Narrative

Regions where icing events or periods with temperatures below the standard operational limits occur are of great interest for the installation of wind power. About one third of the global installed

1.3. Justification and Narrative

wind power capacity is located in what is considered as cold climates, where icing of rotor blades is one of the major challenges [8].

The work leading to this thesis started with an open mindset and a goal to find a method to detect icing on wind turbines by measuring the optical properties of liquid water in clouds. The reflectance and the absorption of light change depending on the wavelength. The absorption of light is comparatively high for some wavelengths in near and far infrared, but low in the visible blue and green. Clouds consist of water droplets, but the absorption of a single droplet is very small. Most of the light energy will be scattered, hit another drop, scatter again and so on, which is why clouds appear gray at a distance.

Light with strong coherence, like that from lasers, will be affected by interference. Coherent and incoherent light sources in wavelengths from visible (450 nm) to near infrared (850 nm) were tested. Illumination angles were tested from 90 (sideways) to 180 (backlit) degrees. After evaluating the different techniques, 180 degrees backlit illumination using blue LED was selected.

Optical measurement of water droplets has been researched and resulted in numerous publications in the last decades. Shadowgraphy is also used in particle velocimetry, to analyze sprays in various applications. While much has been published on these subjects, there is no instrument readily available that is affordable, reliable and possible to operate near the highest point where icing usually occurs, e.g. one hundred meters up on a wind turbine, or a mast. An instrument for measuring icing parameters for wind turbines should both be able to detect supercooled cloud droplets from five to a few hundred micrometers in diameter and be able to determine the concentration to get an accurate measure of the LWC.

The Droplet Imaging Instrument (DII) was designed to find a simple, cost effective and robust technique to measure LWC and MVD in order to predict icing on structures. An automatic sensor based on this technique could be used to trigger ice protection systems used for wind turbines in cold climates [42]. It was calibrated using a micrometer dot scale with dots of verified sizes printed on a transparent glass. The sizing is verified using four samples of polymer microspheres, calibrated in turn by the National Institute of Standards and Tech-

nology (NIST). The functional simplicity and robustness of the DII makes it possible to mass produce and distribute Internet connected instruments based on this technique on a larger geographical scale.

During the winter of 2016-2017, the prototype instrument was placed on the Klövö mountain, Sweden, at one of the Sveriges meteorologiska och hydrologiska institut, (Swedish Meteorological and Hydrological Institute) (SMHI)'s measuring stations, position $62^{\circ}29'41''\text{N}$, $14^{\circ}9'27''\text{E}$, 802 meters above sea level. Measurements are available from November 2016 to March 2017. Results from this measurement together with a parallel measurement of LWC and MVD using a CDP-2 (CDP) from Droplet Measurement Technologies (DMT) are presented in Paper III as well as in this thesis.

1.4 Related Work of Measurement

In 1970, Knollenberg [35] described an electro-optical technique to measure cloud and precipitation particles using a laser illuminated linear array of photo detectors. The photo detectors are used to make a two-dimensional image of the particles' shadows as they pass the light beam. Systems based on this technique are called Optical Array Probe (OAP)s or two-dimensional imaging probes. Development of this technique include using image sensors to save gray scale images of the detected particles [41, 71]. The DII developed and described in this thesis is based on this technique.

Light scattered from a focused laser [2, 17] is another technique that can be used to measure single particles, where a laser beam illuminates passing particles. When a particle is detected, its size is determined by comparing the variations in light with a pattern derived from the Mie scattering solutions [51]. The CDP used as a reference instrument, is based on this technique.

The OAP, imaging and the light scattering spectrometers each have advantages over the other technique depending on the nature of the aerosol. E.g. an instrument that can measure micrometer-sized droplets may not be useful for finding large drops or snowflakes. For accurate airborne measurements of LWC, MVD, and ice content, several instruments and techniques are often combined in a single probe [4, 3].

1.4. Related Work of Measurement

An optical technique that is very similar to shadowgraphic imaging is based on in-line holography [44]. In principle this is a shadowgraph imaging system that uses laser background illumination to create two-dimensional images of the diffraction patterns created by the passing particles. These patterns are measured to reconstruct images of the particles. This is a fairly calculation intensive process, which may be one of the reasons why instruments based on this technique are quite rare as of yet [26]. An advantage of the holographic technique is the increased measurement range, i.e. the useable depth in each image [33].

Sizing of the droplets using Mie spectrometry is a complex operation even for coherent light [6], and although it is possible to study Mie scattering from white light [69], the complexity, small droplet size range and sample volume makes it less attractive for this application, as the optical resolution is usually too low. This also makes it difficult to determine the exact particle size and the usable depth of field for incoherent shadowgraph systems. The shadow from a particle can e.g. appear smaller or larger when out of focus.

Shadowgraph imaging of particles using incoherent illumination instead of laser has been tried e.g. in particle shadow velocimetry (PSV) [18], or spray characterization [73]. There are quantitative and comprehensive studies of other droplet measurement techniques [17, 26, 13].

Kuhn et. al. [40] have described a method to characterize ice particles using Fourier shape descriptors [23, 68]. This system uses a microscope-like technique to achieve a high resolution level, in the order of one micrometer. Although not specifically designed to measure water droplets, the principal design is similar to the DII.

— Chapter 2 —

THEORY

This chapter begins with an introduction to the physics behind the forming of ice on structures. The next two sections briefly describe the measurement parameters and some practical problems of measuring icing. The last section is about scattering of light by small particles.

2.1 Forming of Ice

Cold climate areas, according to the definition by IEA [8] are regions that experience frequent atmospheric icing or periods with temperatures below the operational limits of standard IEC 61400-1 ed3 wind turbines. Atmospheric icing is the period of time where atmospheric conditions are present for the accretion of ice or snow on structures [8].

An icing event can be divided into three phases: the incubation, the accretion and the persistence/ablation. Meteorological icing, which is the main interest of this thesis, is the period during which the meteorological conditions (temperature, wind speed, liquid water content, DSD) allow ice accretion. The incubation is the time in meteorological icing before the accretion starts. The length of each of these phases, and the severeness of the icing depends on a combination of the aerodynamic shape and temperature of the structure or airfoil, the velocity of the air and its contained water, the air temperature, the mixing of snow and water, the concentration of liquid water and the DSD.

Whether a particle is likely to follow the flow or collide depends on the flow velocity, the size and shape of the obstacle and the density and drag coefficient of the particle. This relationship is known in fluid mechanics as the Stokes number (Stk). Small droplets or particles with $Stk \ll 1$ may continue with the airflow around the profile, while large droplets or particles with $Stk \gg 1$, due to their inertia, collide with the structure. A supercooled droplet colliding with a structure is likely to freeze upon impact. Figure 2.1 illustrates the

Chapter 2. Theory

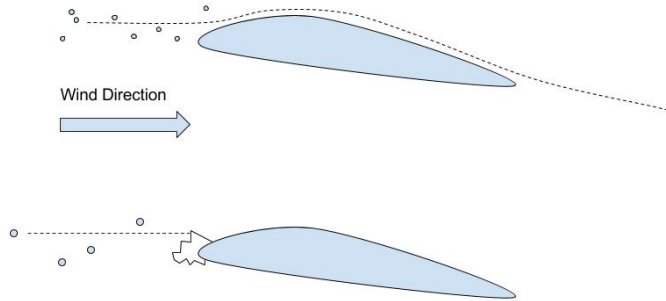


Figure 2.1: Supercooled water droplets on collision course with an aerodynamic profile.

difference between large and small supercooled droplets passing an aerodynamic profile.

Icing is a slightly different problem for wind turbines than for aircraft. Unlike aircrafts, the turbine is stationary and cannot stop the icing, or de-ice by moving to a different position. The same conditions may persist for days or weeks. The turbine blade moves concentrically making the tip of the blade the fastest, and highest located moving part. The remote and exposed position makes it difficult to detect ice directly when it is initially formed [27].

2.2 Liquid Water Content and Median Volume Diameter

The liquid water content (LWC) and the water droplets median volume diameter (MVD) are parameters that can be used to predict or model icing. The MVD is given at the point where half of the total volume of liquid content in a fixed air volume consists of droplets with larger diameters, and half with smaller diameters. The MVD has been assumed to give the best approximation to the spectrum of diameters in a DSD, when considering the collision efficiency [21]. To estimate the amount of icing created by supercooled water droplets, the MVD has been shown to be a good indicator in most cases [47]. The MVD as approximation to the DSD can be used to simulate ice accretion on wind turbines [16].

2.3. Practical Problems with Measuring Atmospheric Water

In practice, the LWC and MVD are rarely measured at a planned or existing wind turbine [55, 46]. Measuring these properties accurately and frequently would be an advantage for the planning of new wind mill farms or for the application of anti-icing arrangements on existing power stations. It may be of particular interest as input to weather prediction models, by which both LWC and MVD can be computed [64, 53]. In combination with information about the aerodynamic properties of the wind turbine, it can give more accurate predictions of icing or even result in better design of wind turbines and anti-icing methods.

While icing caused by large supercooled droplets, with diameters from approximately 50 µm to more than 1000 µm, is often considered severe due to its shape and quick build-up, icing may occur even with droplets as small as 5 µm [58, 11, 28]. In most cases though, icing is caused by cloud droplets measuring between 10 µm and 30 µm in diameter [46, 11].

Although optical imaging and other techniques for measuring aerosol properties are continuously improving, the choice of instrument is still very much dependent on the application's requirements [30, 2, 3, 41]. An instrument for measuring icing parameters for wind turbines should be able to detect supercooled cloud droplets as small as five micrometer and determine an accurate measure of LWC. Since measurements are needed in multiple remote locations, it should also be affordable, reliable, and, ideally it should be possible to place it near the highest point of the turbine [27].

2.3 Practical Problems with Measuring Atmospheric Water

The varying nature of atmospheric water particles mentioned in the previous chapter makes it very difficult to measure all kinds and sizes of particles using a single instrument. Therefore, atmospheric aerosol studies are often done with one or several instruments combining different techniques. Each technique with its own limitations and problems. It is also difficult to find a reference sample with the same but known properties as the water. Free floating water droplets are affected by gravity, they eventually collide and coalesce, evaporate or

Chapter 2. Theory

stick to adjoining surfaces. This makes it difficult to measure and find out the physical properties without affecting the sample.

The size of water droplets range from a few micrometers to several mm in diameter. An imaging instrument is limited by the optical system's resolution, its field of view and the usable depth of field or the measuring range.

Many existing instruments suffer from errors caused by the instrument itself during sampling, e.g. when droplets get stuck on the inlet [62]. At higher wind speeds particles shatter into smaller droplets or bounce on the supporting structure making up the instrument [12, 19]. All droplets or particles approaching an obstacle are affected by the change in pressure and wind direction surrounding it, a fact which complicates measuring the concentration of particles in unaffected air. Measurement probes working by extraction of air using a mechanical air pump would expect a loss of particles with large Stokes numbers. Ideally, the measuring device should be designed to have as little effect on the free flow of particles as possible [3].

An example of an instrument that makes use of the fact that supercooled water droplets will freeze upon impact, is the rotating cylinders used by Makkonen [46]. By exposing cylinders of different diameters, depending on the amount of ice accumulated on each cylinder, the MVD and LWC can be calculated using a theoretical model. While this technique provides an alternative to the single particle measurements its drawback is that it requires a certain extent of manual operation, in addition to the fact that only freezing water can be measured.

Measuring particles via aircraft is complicated by the high air speed. The sample is affected by the change in pressure surrounding the aircraft and by particles hitting parts of the probe, splintering or changing direction, causing anisokinetic sampling [3]. An instrument fixed to the ground on the other hand is affected by the wind speed relative to the ground. This means that it needs to be directed in the direction of the wind. Particles may also enter the measurement zone from different directions depending on their Stokes number, which has been shown to have an effect on the measured liquid water content [26].

Instruments based on Mie calculations of light scattering some-

times struggle to deal with with a non-linear relation between scattering response and diameter. Aliasing in the sample bin resolution can lead to spikes in the DSD. Particularly interesting is the 10 to 15 μm range, where two particles with diameters differing more than one micrometer can have the same scattering intensity response [17, 62, 6].

2.4 Light Scattering and Absorption

In visible light, water is almost transparent. This means that the imaginary part of the refractive index, i.e. the absorption, is very small, while for some wavelengths it increases many times. This fact is used in two-color lidar measurements [72]. The real part of the refractive index for water is much more stable; approximately 1.3 in the visible to near infrared range [24, 38].

For a shadowgraph system, it is possible to assume that the refractive index of air is equal to one. A droplet works as a spherical lens with a very short focal length. Exposed to a background illumination it will scatter almost all of the light that reaches the droplet, causing a shadow that appears as a black disc except for the light passing straight through the center. Some of the light will also be absorbed, but the absorption of light by a single water droplet is negligible due to its small volume.

When the light source is large compared to the size of the droplets, as in the case of using a collimated LED, the intensity of the center Arago spot caused by Fresnel diffraction is small [57].

The combined effect of scattering and absorption is the extinction [6]. Due to this combined effect, clouds look nontransparent from a distance. Measuring the light's extinction is possible, e.g. by using a Raman LIDAR [1].

MATERIALS AND METHODS

The methods in this chapter can be seen as the answers to research question RQ1-RQ3 from Chapter 1. To begin with, a few different light sources and illumination angles were investigated. In section 5.3, the lighting alternatives that were considered, are described. It was settled that a shadowgraph system with background illumination from an LED was to be used. The experimental setup was tested using different water droplet generators and a test target consisting of micrometer sized lines and dots. Analyzing the optical system and testing different segmentation algorithms, we found a simple way to define the sample volume for each individual droplet. To test the ability of measuring concentration we needed to build a weather protected prototype that could be used in parallel with a second instrument. The prototype needed to be fully automatic, able to analyze images in real time 24 hours a day for several months and store the results in a compressed format. To calibrate the size measurement and the measurement range, the previously mentioned dots of different sizes were used. The size measurement was also verified using distributions polymer microspheres, applied by blowing compressed air through a glass dispenser.

3.1 The Shadowgraph System

The instrument is a shadowgraph system using a monochrome Complementary Metal Oxide Semiconductor (CMOS) camera with a 4x magnifying telecentric lens and a LED with a collimating lens illuminating the background. Figure 3.1 shows a sketch of the system. The system was first tested in the experimental setup seen in Figure 3.2.

The blue LED, shown to the right in Figure 3.2, was initially powered by a SignaTech Strobe Controller from Advanced Illumination. The SignaTech Controller can produce up to 4A at 100V. For the prototype instrument, another current driver, the Picolas LDP-V 10-70

Chapter 3. Materials and Methods

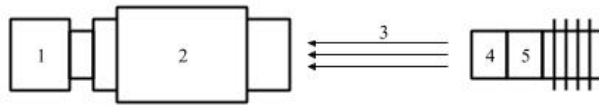


Figure 3.1: Principle of shadowgraphy. 1. Camera. 2. Telecentric lens. 3. Parallel focused light beam. 4. Collimating lens. 5. LED.

was chosen. This driver can produce short 12A pulses. For controlling the pulse length, a microcontroller is used.

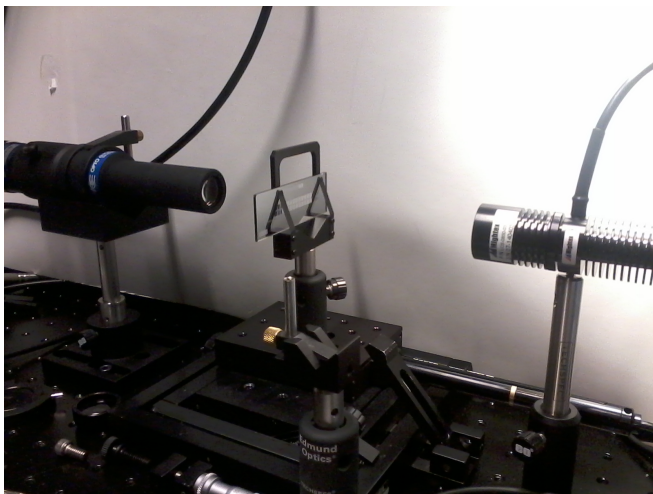


Figure 3.2: The experimental setup with a dot micrometer scale as test object mounted on a translation stage.

The complete system was mounted in a weather proof shell using two standard camera housings and a separate box for the analyzing computer and power supply. Figure 3.3 shows the system mounted in weather proof camera housings.

3.2 Overview and Process

A stage micrometer scale was used for characterization of the system and simulation of water droplets. This characterization holds true given that the optical silhouette of a droplet is comparable to a dot of

3.2. Overview and Process



Figure 3.3: The illumination and detector is mounted inside two Bosch camera housings facing each other with heating inside the housings and on the front glass.

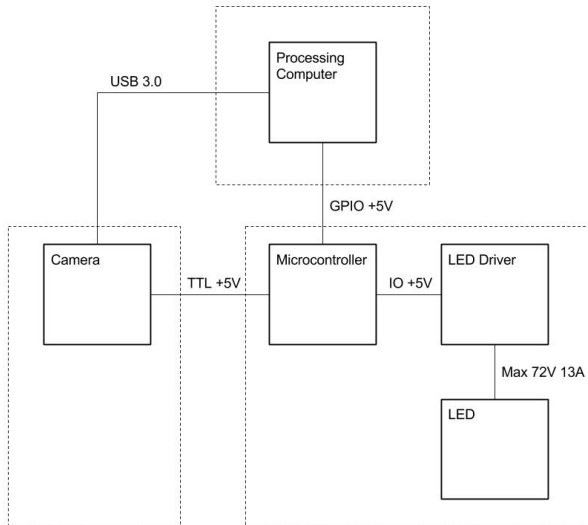


Figure 3.4: Electrical interfaces and system overview.

equal diameter printed on a silicon glass. It is not a new concept and has been proved experimentally by comparing beads of glass and water droplets of known sizes [37, 36]. Light passing a transparent sphere is affected by its refraction, reflection, diffraction and absorption. Of these four components, the shadow will be defined mainly by the diffracted, as long as the distance between the sphere and the lens is much greater than the sphere's diameter [37, 71].

Chapter 3. Materials and Methods

The design using a weakly collimated LED that illuminates an area slightly larger than the field of view makes the system quite insensitive to misalignment of the camera and the light source. Temporal or permanent changes in light intensity caused by a minor misalignment are automatically compensated for by continuous measurement of the total exposure level. If the level of exposure is increasing or decreasing, the length of the light pulse is changed correspondingly. The light intensity can also be affected by dirt on the front glass of the housings.

Since many images do not contain any droplets at all, we increase the processing speed by sorting out the images that do not contain any interesting information. This is done by constructing an average image from 20 images. All new images are compared with this average, and if any pixel differs from the average, by more than a specific value that is significantly higher than the noise level, the image is analyzed. The average image is re-constructed periodically.

Spatial dissimilarities in the light intensity that are not caused by noise are compensated for by calculating the local average intensity of the background around each measured droplet. This way, a variable threshold [22] is constructed. The size of a droplet is then based on the intensity dip caused by the shadow compared with its local background.

3.3 Image Segmentation

If the image contains an object detected by the thresholding, the sample volume is calculated for each droplet individually depending on its size. By using a Laplacian of Gaussian [50, 22] edge detection and a suitable threshold, we can create closed curves around objects where the edge is in or near focus. Other edge detection operators like Roberts, Prewitt, Sobel [22] and Canny [9] did not seem to give the same consistent performance in different lighting conditions. The objects that create closed curves, selected by a boundary fill function, are said to be within the measuring range. The measuring range together with the field of view defines the sampling volume. The measurement volume is described in Paper I. Since the Laplacian of Gaussian can be seen as value of the second derivative of the edge

3.3.1. Exposure Check and Flash Intensity Adjustment

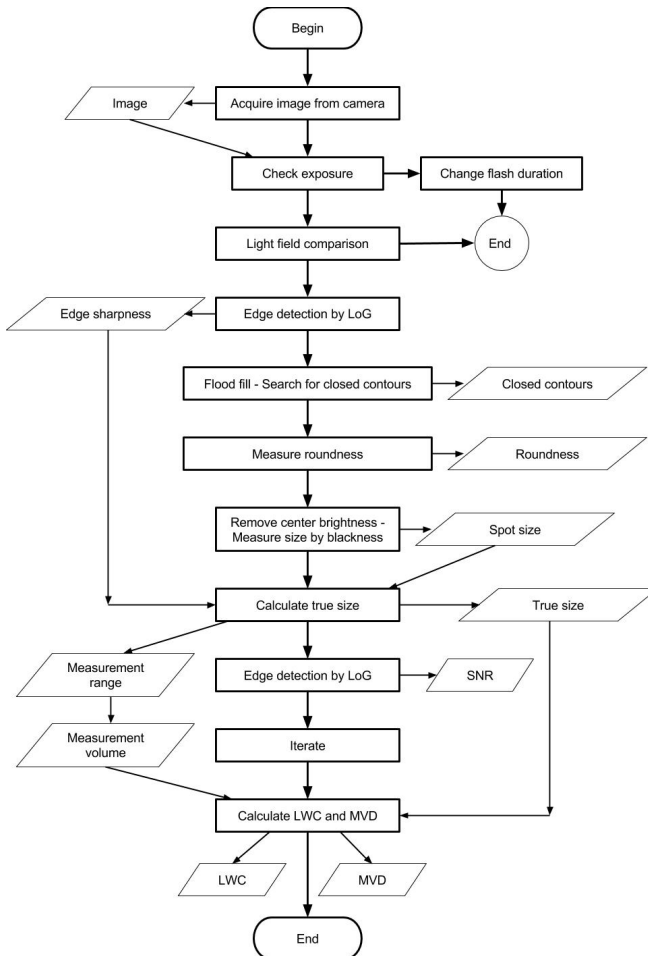


Figure 3.5: Flowchart illustrating the method of image processing step by step.

gradient, it is also used together with the diameter to calculate the true size of the droplet. This is described in Paper II.

3.3.1 Exposure Check and Flash Intensity Adjustment

Let $I_{i,j}$ denote the two-dimensional image captured by the camera. The mean value \bar{i} of all pixels in the image $I_{i,j}$ gives an estimation of the exposure level in the whole image.

Chapter 3. Materials and Methods

The flash duration is adjusted automatically by the microcontroller at each exposure to keep the exposure level between a low and a high threshold, th_L and th_H . The duration is changed in steps of 13 ns corresponding to one clock cycle of the microcontroller. If $\bar{i} > th_L$ and $\bar{i} < th_H$ the image is analyzed. If $\bar{i} \geq th_H$ the flash duration is decreased by steps of 12 ns. If $\bar{i} \leq th_L$ the flash duration is increased. The total flash duration is approximately 250 ns. Here th_L is set to 0.7 and th_H is set to 0.8 in a normalized (0,1) dynamic range.

3.3.2 Edge Detection and Edge Sharpness

To detect the intensity changes created by the shadow of a water droplet, an image is processed using the Laplacian of Gaussian (LoG) described by Marr and Hildreth [50]. The method works by looking for zero crossings in the image resulting from calculating $\nabla^2 G(x, y) * I(x, y)$. $G(x, y)$ is a two-dimensional Gaussian distribution with standard deviation σ and ∇^2 is the Laplacian operator, defined as the divergence of the gradient in two dimensions.

$$G(x, y) = \frac{1}{\pi\sigma^2} e^{-\frac{x^2+y^2}{2\sigma^2}} \quad (3.1)$$

$$\nabla^2 = \nabla \cdot \nabla = \frac{\delta^2}{\delta x^2} + \frac{\delta^2}{\delta y^2} \quad (3.2)$$

We implement a discrete approximation to $\nabla^2 G(x, y) \approx \nabla^2 G_{i,j}$ as a 13x13 sized convolution kernel.

$$\nabla^2 G_{i,j} = -\frac{1}{\pi\sigma^4} \left(1 - \frac{i^2 + j^2}{2\sigma^2}\right) e^{-\frac{i^2+j^2}{2\sigma^2}} \quad (3.3)$$

By applying the convolution to the normalized image $I_{i,j}$ we get the image $P_{i,j}$.

$$P_{i,j} = \nabla^2 G_{i,j} * I_{i,j} \quad (3.4)$$

$P_{i,j}$ is thus a matrix that contains the second order derivative of the image $I_{i,j}$. A spherical object will result in an edge where the intensity change is similar around a spherical object, but dependent on the distance from the optimal focus. Assuming the Gaussian of the image I is twice differentiable at any point (i, j) , the maximum (or

3.3.3. Comparing Transparent Microspheres and Dots

minimum) of the second derivative includes the amplitude of the first derivative at the point where the second derivative is equal to zero, i.e. where the edge is strongest. This can be intuitively understood; when the edge is sharper, the gradient, or first derivative value, is larger. And if the gradient value is larger, the rate of change, i.e. the second derivative, needs to be larger at each side of the edge. Therefore, we store a value of the maximum second derivative, $\max(P_{i,j})$, around each analyzed object and use this as a measure of the edge sharpness. This value in turn is used as input to a calibration function. We also construct a new binary image Q in which the pixel value $Q_{i,j} = 1$ if any of $|P_{i+1,j} - P_{i,j}|, |P_{i-1,j} - P_{i,j}|, |P_{i,j+1} - P_{i,j}|, |P_{i,j-1} - P_{i,j}| > th$, where $th = 0.002$. $Q_{i,j} = 0$ elsewhere. th is the gradient of the second derivative at the point where the second derivative is zero, i.e. on the edge. Particles are found by searching for closed contours in this binary image.

3.3.3 Comparing Transparent Microspheres and Dots

A spherical lens scatters almost all the incident light in different directions, leaving only a bright spot in the middle where the light is transferred directly through. For larger particles in focus, this bright spot can result in a second circular closed contour inside the outer edge.

Small water droplets can be seen as transparent microspheres. The composition changes the refractive index, but this has little effect on the shadow. The outer contour is the same following the same reasoning as dots used for calibration in Paper I. Diffraction patterns depend on the wavelength of the light and the size of the sphere. The resolution of the constructed system is not high enough for these patterns to be visible.

By using a flood-fill function on the binary image containing the detected contour, starting at a point at a minimum distance from an object, the edge of the filled area will border to the outer contour. This makes it possible to select the outer closed contours of possible particles.

Chapter 3. Materials and Methods

3.3.4 Removing the Center Bright Spot

The center bright spot will make the shadow of a transparent sphere brighter in average than a solid dot. This will have an impact on the size calculation, since the size calculation is based on the shadow impact and the calibration is done using solid dots. Therefore, we apply a mask on the image before calculating the size of the shadow. The mask is done by replacing all the centermost pixels in the shape of a circular disc with the intensity of the darkest pixel in the spot. The diameter of the masked disc is the arc length of the edge contour divided by π . The bright spot is measured by calculating the difference between the least value and the center pixel. Only particles with a difference greater than 0.1 (ten percent) will have the mask applied

3.3.5 Measuring Roundness

There may be clogs of small microspheres or dust in the samples that are measured. Microspheres, or small water droplets are close to spherical. We try to exclude all objects that the program finds that are not circular. After the detection of object edges, we measure the roundness of each object. A measure of the mean square roundness deviation similar to the one described by ISO [54] can be achieved by calculating the quote between the area of the contour and the square of the total arc length. See (3.5).

$$roundness = 4\pi \frac{A_{contour}}{arcLength^2} \quad (3.5)$$

$A_{contour}$ is the pixel area of the filled contour and $arcLength$ is the perimeter of the measured closed contour. In the calibration and field measurements described, an object is only considered spherical if $roundness \geq 0.85$.

3.4 Light Source

Although water is a good absorber of electromagnetic radiation in most spectral wavelengths except for the visible, the volume of water droplets is too small for the absorption to be measurable. In visible

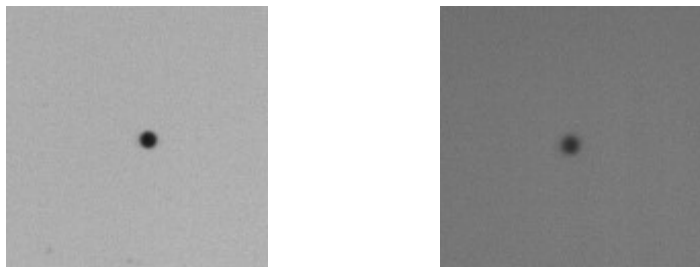


Figure 3.6: The same dot viewed with different background light: 455 nm (left) and 850 nm (right).

light, the water droplet can be regarded as a spherical lens with a very short focal length, thus spreading most of the light in diverging directions. Since the camera used is designed for both visible and near infrared light, we tested and compared two different wavelenghts, 455 nm and 850 nm using the same optical setup. The shorter wavelength gave sharper images and higher SNR.

3.4.1 *Laser Light*

For conventional imaging of small particles the coherence of laser light mainly causes problems as diffraction patterns will be strong and visible. Therefore this was only briefly investigated. In section 5.3.2 there is a discussion of the result from this investigation.

3.4.2 *Ambient Light*

In daylight, there is always some ambient light. Although the camera is never aimed directly at the sun and has a telecentric lens, we wanted to be sure that this light would not affect the measurement. For an indication the amount of ambient light, the system was tested in daylight, using a fog generator in front of the lens to reflect light into the lens.

3.5 Image Noise

We had an idea that it should be possible to measure the signal to noise relation, if the shadow image of the droplet represents the signal. In

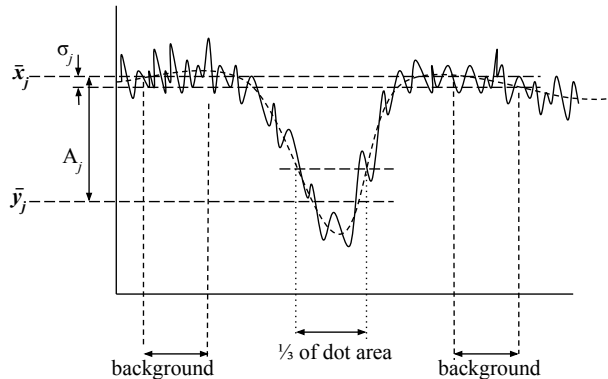


Figure 3.7: Calculation of the SNR. \bar{y}_j is determined by calculating the average of the darkest third of all pixels inside the edge detected dot.

theory, the SNR could be used as an input to the size or concentration calculation, to increase the accuracy of the measurement.

An estimation of the image noise in the whole image was done by making a number of images using only the background illumination. The standard deviation was calculated in each pixel of the 2048x2048 sized image, resulting in an average variation coefficient of about nine percent.

A function was created that calculates the noise level locally around each analyzed droplet image. Assuming that the area surrounding a droplet is evenly illuminated, the SNR can be estimated for each droplet j , as the relation between the signal and the ambient noise. The signal is the light amplitude, A_j , and the noise is the standard deviation of the surrounding noise, σ_j . See (3.6) and Figure 3.7.

$$snr_j = 20 \log \frac{A_j}{\sigma_j} \quad (3.6)$$

3.6 Calibration and Validation of the Calibration

Because of the diffraction, the edge of an object is difficult to measure directly by thresholds, even if the coherence length of the light is

3.6. Calibration and Validation of the Calibration

small and the object is in focus. The edge will appear blurry. For objects out of focus, the blurring will increase even more. Therefore the size measurement is calibrated by both measured diameter and a value of the edge sharpness, or gradient.

Also the measuring range needs to be calibrated. The measuring range is here defined as the distance in which the edge detection by Laplacian of Gaussian operator and a threshold makes a closed curve in the resulting binary image. This will be different especially for smaller objects.

The system was calibrated using a stage micrometer scale with 13 circular dots printed in chrome on a silicon glass. The dots range from 2 to 100 μm in diameter. Each dot was moved linearly in steps of one micrometer in the direction orthogonal to the lenses, thus creating a function where the gradient of the edge depends on the distance from optimum focus. A threshold on the second derivative gradient strength limits the measured particles to be within a specific measuring range. The threshold should be selected carefully. If the value of the threshold is too low, there will be many false edges in the image. If it is too high, the measuring range will be too small. The difference between two different thresholds, 0.002 and 0.005 is illustrated by Figure 3.8. The lower threshold was used in the following measurements.

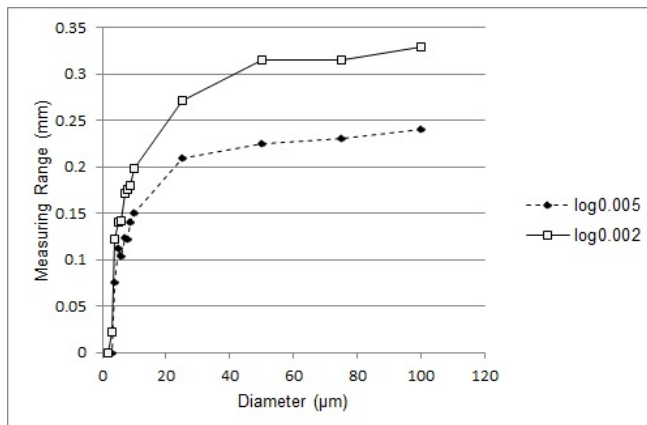


Figure 3.8: Measuring range (mm) vs. diameter for two different thresholds (0.005 and 0.002).

Chapter 3. Materials and Methods

The edge sharpness will affect the position of the edge and the measured shadow slightly. We use the maximum value of the second derivative $P_{i,j}$ for each droplet as a measure of the edge sharpness and include this in the calibration functions, together with the diameter measured from the shadow intensity.

Two second degree approximation surfaces, (3.7) and (3.8), are calculated using the “fit” command in Matlab. z_1 approximates dot diameters from 2 to 10 micrometers and z_2 diameters from 10 to 100 micrometers. x is the maximum second derivative, d^M is the diameter measured from the shadow intensity, p_{xx} and q_{xx} are constants.

$$z_1 = p_{00} + p_{10}x + p_{01}d^M + p_{20}x^2 + p_{11}xd^M + p_{02}(d^M)^2 \quad (3.7)$$

$$z_2 = q_{00} + q_{10}x + q_{01}d^M + q_{20}x^2 + q_{11}xd^M + q_{02}(d^M)^2 \quad (3.8)$$

By measuring the calibrated microspheres a validation can be made with the expected diameter.

3.6.1 Verification of Dot Size

The dots on the micrometer scale were measured visually using a Leica microscope connected to a digital camera. This was done to find accurate values of the diameter of the dots to use in the calibration. An example image that was measured can be seen in Figure 3.9.

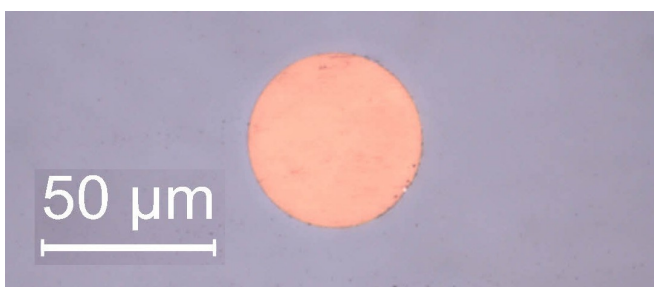


Figure 3.9: The 50 micrometer dot with front illumination imaged using 40x magnifying lens.

This measurement was done using lenses with two different magnifications: 40x and 100x. All the dots average diameters, except

3.7. The Fog Chamber

the 100 μm dot were found to be within $\pm 0.2 \mu\text{m}$ of their nominal diameter. They are not all perfectly round, but the size accuracy should be good enough to use as calibration reference. The result from this measurement is presented in Table 3.1.

Nominal Diameter	Excentricity	Diam. 40x	Diam. 100x
5	0.2	5	4.8
6	0.6	5.8	5.8
7	0	7	6.6
8	0	8	7.9
9	0	9	8.8
10	0	10.1	9.8
25	0	24.9	24.7
50	0.4	50.1	49.8
75	0.2	75.2	74.8
100	2.5	100	98.7

Table 3.1: Micro dot verification measurement. All values are in μm . Here, eccentricity is the maximum difference in μm between the smallest and the largest measured diameter.

3.7 The Fog Chamber

Natural fogs tend to not coincide with when we are ready to test. The fog chamber was needed to create a test environment for the instrument.

The constructed chamber has a frame made of 30 mm aluminum profiles, fitted with transparent 6 mm polycarbonate walls on all sides using rubber sealing strips. The droplets are produced using an ultrasonic fog generator pushing the droplets to the chamber through a flexible tube approximately 30 mm in diameter and 500 mm long. Next to the fog inlet, there is a dry air inlet with a speed adjustable fan. On the back of the chamber there is a similar-sized outlet for air and moisture. See Figure 3.10.

Chapter 3. Materials and Methods

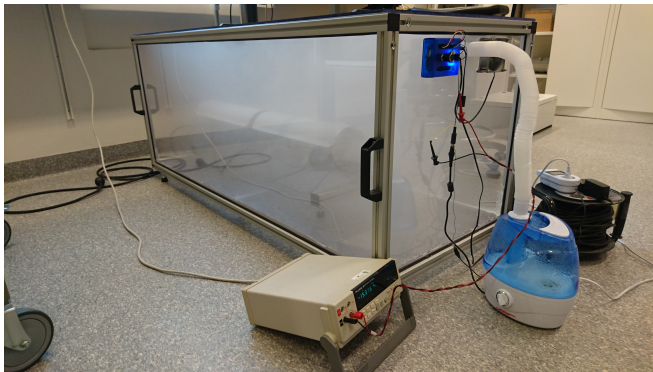


Figure 3.10: Fog chamber with connected droplet generator (blue container) and a multimeter used for fan power measurement. A Beaglebone Black microcontroller (blue box) is used for fan speed regulation.

Unfortunately, we could not fit a second instrument in the fog chamber for verification of the LWC. The CDP requires an airflow with a known speed to be able to calculate the particle concentration. The fog chamber worked very well as a functional test and a verification of the instrument's water ingress resistance.

3.8 The Klövsjö Installation

Figure 3.11 shows a complete installation of the DII and the CDP at the Klövsjö mountain. The two camera houses of the DII are placed on the top, and the smaller CDP right underneath. The Lambrecht Eolos weather sensor is placed to the far left, mounted on an horizontal boom. In the middle, to the right of the Eolos, the mobile communication antenna is located. The top of the shortened lattice mast can be seen just below the center. Behind the mast, the top of the box containing the DII processing computer, the CDP data collection computer, and the communications router can be seen. The whole installation is about five meters high. An electric servomotor mounted at the base of the pole inside the lattice mast rotates the two instruments automatically to follow the horizontal direction of the wind.

Figure 3.12 shows a mix of ice and snow on the front side of the installation.

3.9. Numerical Weather Prediction



Figure 3.11: Installation in Klövsjö.

3.9 Numerical Weather Prediction

For a second validation, we carry out weather simulations around the site using the HIRLAM (High Resolution Local Area Mod-

Chapter 3. Materials and Methods



Figure 3.12: Ice and snow on the front side of the installed instruments. The CDP is more efficient at preventing ice.

elling)-ALADIN (Aire Limitée Adaptation dynamique Développement InterNational) Research on Mesoscale Operational NWP (Numerical Weather Prediction) in Europe (HARMONIE)-Application de la Recherche à l'Opérationnel à Méso Echelle, (Application of Research to Operations at Mesoscale) (AROME) numerical weather prediction (NWP) model. The model is described in Paper III.

SMHI agreed to run a special model domain locally with 500 meters horizontal resolution for a limited time. The operational forecasts are run at 2.5 km horizontal resolution, and they were used as initial conditions and lateral boundaries for the detailed simulations.

At SMHI, the HARMONIE-AROME model is used for short range operational forecasting. It is run in cooperation with the Norwegian Meteorological Institute. The initial conditions and boundaries for the operational forecasts are provided by the European Centre for Medium-Range Weather Forecasts (ECMWF) global model.

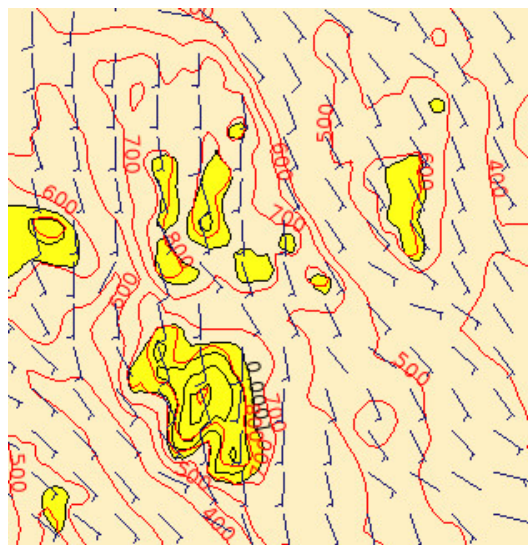


Figure 3.13: Graphical presentation of data from the HARMONIE-AROME NWP covering Klövsjö and the surrounding mountains at a specific point in time using 500 m resolution. Yellow areas are where the model predicts an LWC more than $0.1 \text{ g} \cdot \text{kg}^{-1}$. (Grams of water per kg air.) Simulation and figure by SMHI.

RESULTS

The contents of this chapter are also found in Paper III. This result shown here can be seen as the answers to research question RQ4, and partly RQ5 from Chapter 1.

4.1 Measurement of Polymer Microspheres

Four NIST calibrated distributions of microspheres, approximately 5, 10, 20 and 50 μm in diameter were used, resulting in four different measured size distributions. All images were saved and visually inspected, resulting in some measurement outliers due to clogging of smaller particles or contamination of small particles among larger. The outliers that were identified as not of the real distribution are not included in the result shown. Histograms of the measurement can be found in Figure 4.1. A summary of the result is shown in Table 4.1.

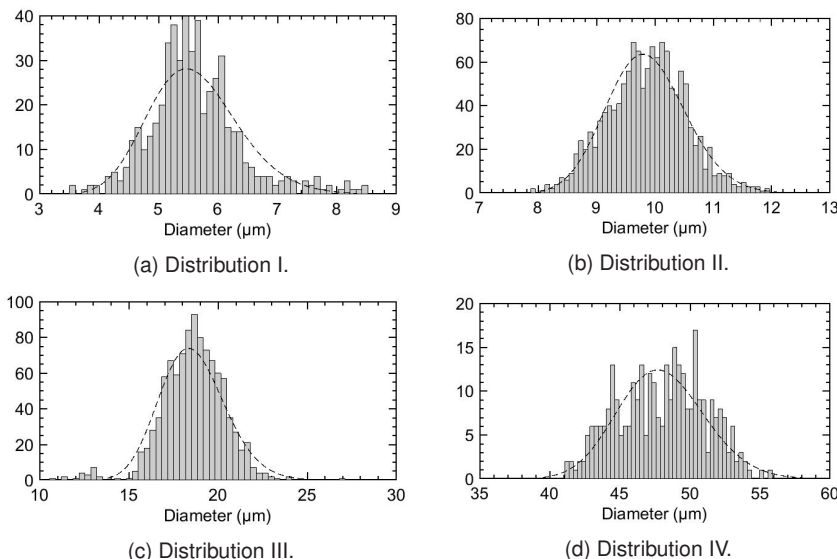


Figure 4.1: Histograms of the four measured distributions. The dashed line is a fitted lognormal of the weighted distribution.

Distribution	I	II	III	IV
Stated mean diam.	5.3 (± 0.3)	10.3 (± 0.4)	19.1 (± 0.7)	49.4 (± 1.6)
Measured mean diam.	5.6	9.9	18.6	48.0
Stated std. dev.	0.5	0.9	1.7	3.5
Measured std. dev.	0.77	0.67	1.7	3.1

Table 4.1: Summary of the result from the measurement of NIST certified microspheres. All values are in μm .

4.2 Comparison of DII and CDP Data

Figure 4.2b shows the MVD measured by the CDP compared with the DII. The least squares method applied on the data set results in a slope of 0.77 and a very small offset of -0.3 μm . Ideally, if both instruments were measuring the true diameter, the slope here would be equal to 1. A straight line with a slope that is not equal to 1 means that there is a systematic difference between the CDP and the DII in the size measurement.

We compare the instruments by studying the data from 28 February to 1 March. See Figure 4.3 and 4.2. Figure 4.3b shows the LWC measured by the CDP compared with LWC measured by the DII. Using the least square method on the whole data set gives an average quote of 0.27. The quote is drawn in the plot as a straight line from the origin. Here too, the ideal case is a straight line with the slope equal to 1. The difference is discussed in Section 5.1.

4.2. Comparison of DII and CDP Data

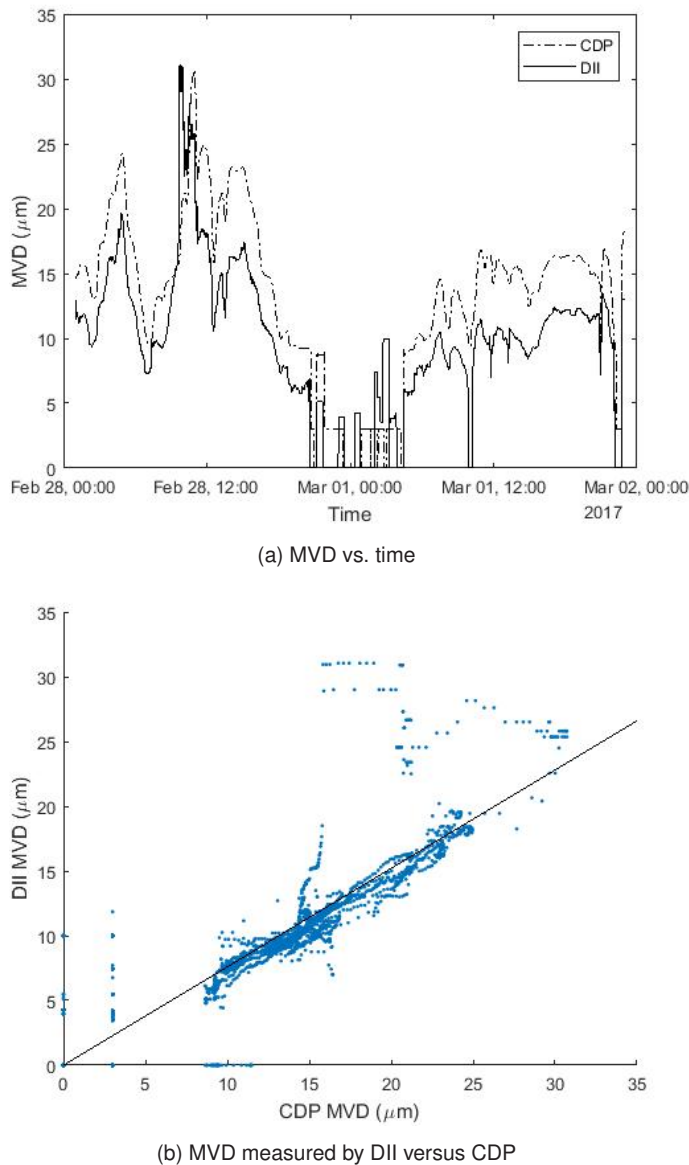


Figure 4.2: MVD minute values measured by the DII and the CDP for 46 hours on 28-02-2017–01-03-2017.

Chapter 4. Results

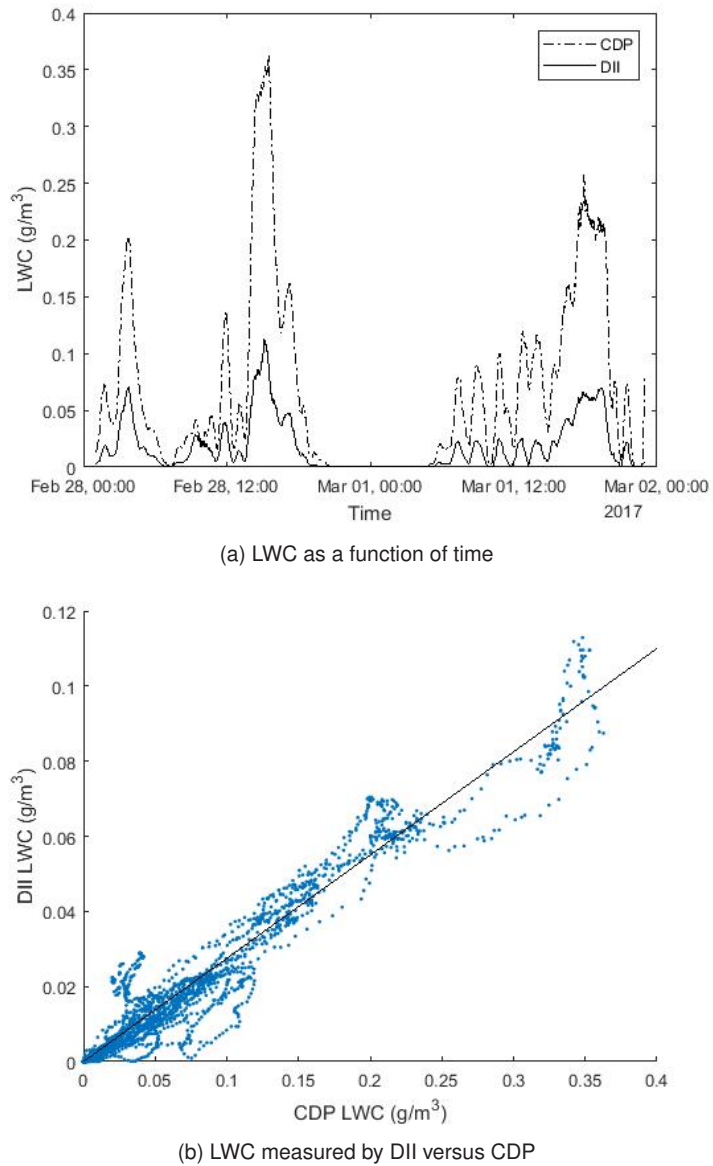


Figure 4.3: LWC measured by the DII and the CDP for 46 hours on 28-02-2017–01-03-2017.

4.2. Comparison of DII and CDP Data

The quote between the LWC values of the two instruments is plotted together with the wind speed in Figure 4.4. The least square average is plotted as a horizontal line at 3.65 (CDP LWC/DII LWC). The logarithmic scale is cropped with 238 quote values above 100 and 121 values below 0.1 out of a total of 2760.

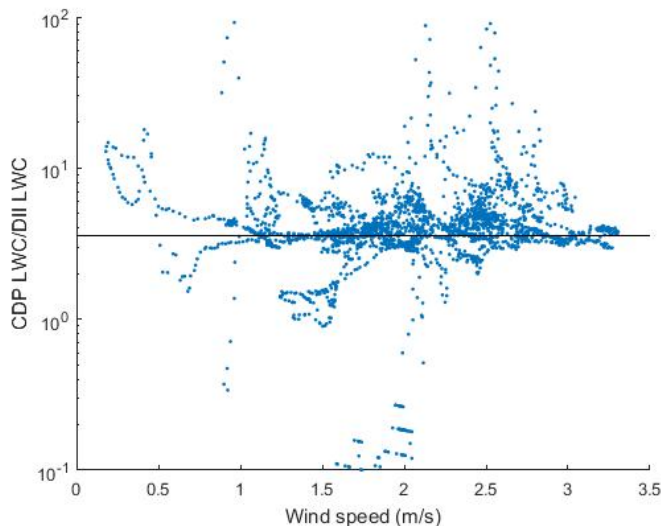
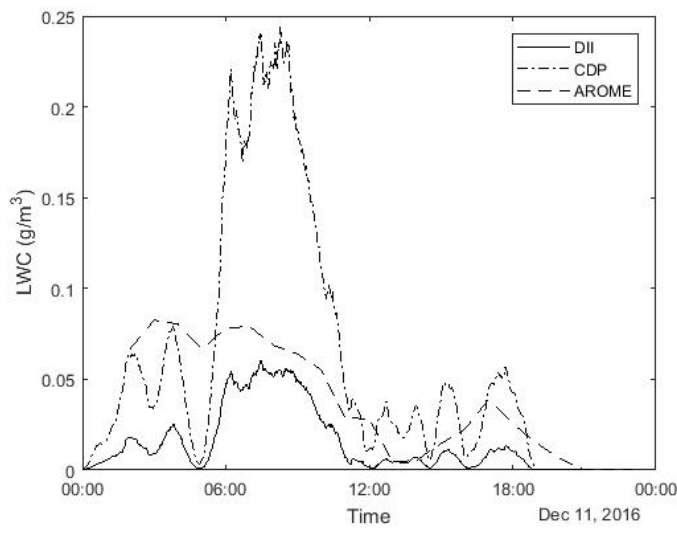


Figure 4.4: Relation between the wind speed and the quote between the LWC measured by the CDP and the DII. The vertical scale is cropped at 1 and 100. 238 values are above 100 and 121 below 1 out of a total of 2760.

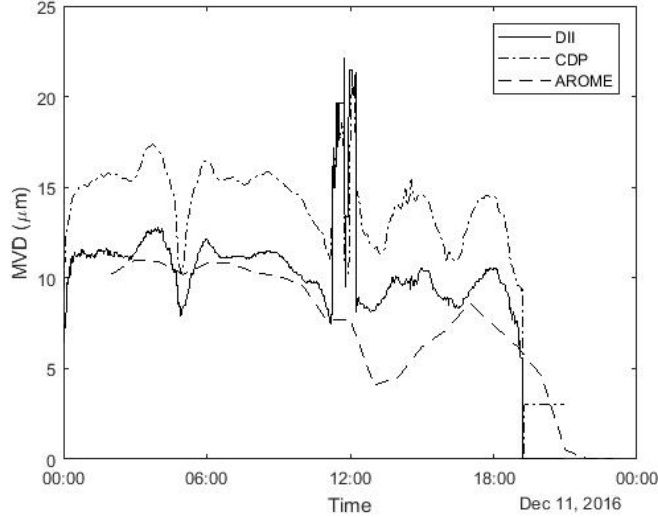
4.3 Comparison of Measured and Modeled Data

Figure 4.5 shows the LWC and the MVD from the two instruments compared with the data from the HARMONIE-AROME model at 500 m resolution. The fog lasted for about 19 hours on 12-11-2016. The difference between the two instruments follows the same systematic pattern during this specific measurement, as in all the other observations. The HARMONIE-AROME model data of the LWC follows the general data of the LWC but fails to detect the large increase in LWC between 05:00 and 12:00. The predicted MVD of the model is closer to the actual values of the DII than the CDP.

4.3. Comparison of Measured and Modeled Data



(a) LWC vs. time



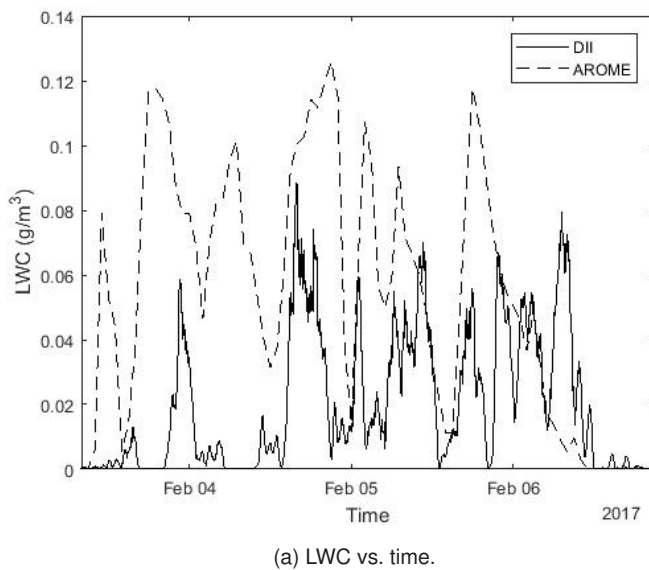
(b) MVD vs. time

Figure 4.5: LWC and MVD measured by the DII and the CDP 11-12-2016. HARMONIE-AROME model data using 500 meter resolution.

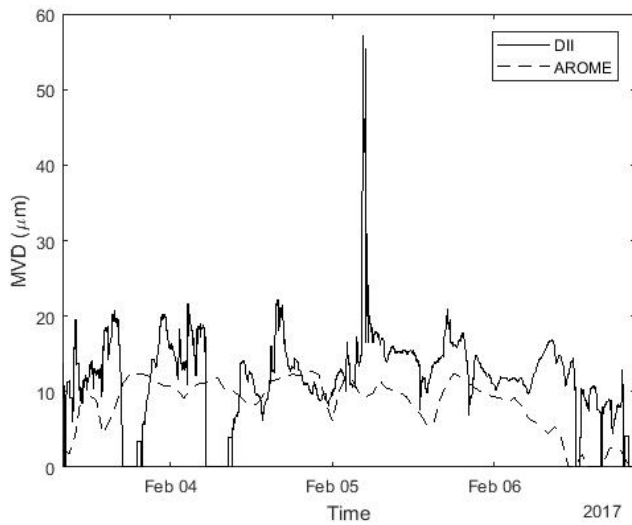
Chapter 4. Results

Figure 4.6 shows the result from measurement 03-02-2017–06-02-2017. Unfortunately, no data from the CDP was saved at this point, due to a full memory. The double spike in the MVD diagram 4.6b at 04:17 and 04:41 on 05-02-2017 is mainly caused by two droplets, 51 and 74 μm (see Figure 5.7) in combination with a number of large droplets between 30 and 40 μm in diameter.

4.3. Comparison of Measured and Modeled Data



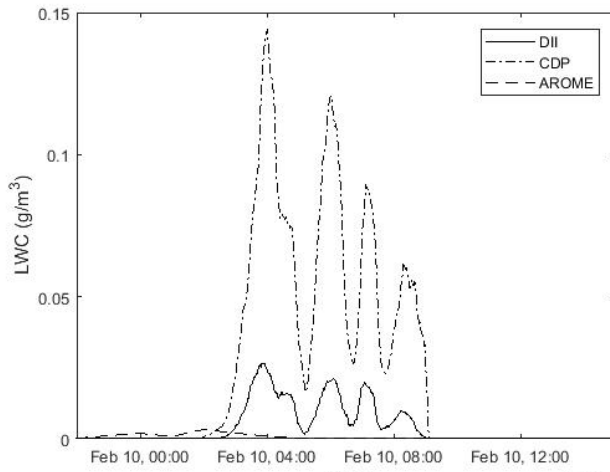
(a) LWC vs. time.



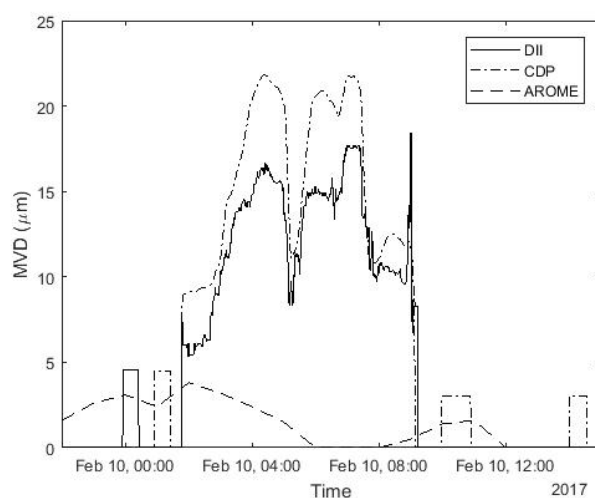
(b) MVD vs. time.

Figure 4.6: LWC and MVD measured 03-02-2017–06-02-2017 by the DII. HARMONIE-AROME model data using 2.5 km resolution, stored every 60 minutes.

Chapter 4. Results



(a) LWC vs. time.



(b) MVD vs. time.

Figure 4.7: LWC and MVD measured by the DII and the CDP 10-02-2017. HARMONIE-AROME model data using 2.5 km resolution, stored every 60 minutes.

DISCUSSION

This chapter includes an extends the discussion of the result mainly published in Paper III, also included here in Chapter 4. It also includes a discussion about the initial choice of method and some details that are not fully covered in the attached papers.

The chapter begins with a discussion on the systematic difference noticed between the CDP and the DII. It continues with a reflection on the two NWP model resolutions used.

After this, there is a section about some of our first questions regarding lighting and imaging of small particles, a section on the image noise and a description of some difficulties that was encountered during the size measurement verification using polymer microspheres. The use of LED light and the measurement accuracy based on statistical data are discussed.

Finally, the droplet size, the sampling speed (including the measurement volume) and the DSD are discussed.

5.1 Cause of Systematic Difference

The measured LWC of the DII and the CDP in Figure 4.3b differs by a factor of approximately 3.65 (CDP LWC / DII LWC). There may be several reasons for this difference.

Comparing the measured MVD of the DII and the CDP we get a quote between the two instruments of 0.77. This means that the MVD of the CDP is on average 30 percent higher than the DII. Since the LWC is proportional to the third power of the droplet size, an increase in the diameter of 30 percent will increase the LWC by $1.3^3 = 2.2$. Unless the droplets are affected by the instruments themselves, there are two possible explanations. One is that the two instruments measure the sizes of the droplets differently. The other is that the sampling volume differs depending on the size of each droplet for one or both instruments.

The CDP and its predecessors, have shown a tendency of oversizing droplets when calibrated by glass or polymer spheres [70, 43]. This

could still explain some of the difference. The precision of the CDP size measurement is also limited by the fixed size bins, and by the pulse amplitude of the scattered light calculated from Mie theory [43, 6]. A small disturbance, like a slight misalignment of the laser beam, may cause a shift in the optical response pushing the size to the next or previous size bin [43]. The sampling area, i.e. the illuminated area that the particles must pass through to be recorded, is an average value given by the manufacturer on delivery.

From Figure 4.4 we conclude that there is no relation between the difference between the two instruments and the wind speed when the wind speed is below four meters per second.

The LWC value depends on an accurate estimation of the sampling volume. While the image area can be determined accurately, the measuring range depends both optical factors and the image processing and segmentation. The measuring range depends e.g. on the light exposure. It may also depend on the distance from the object to the optical center. Since the calibration of the measurement range was only done once, close to the optical center, the sampling volume of the DII may actually be smaller than estimated. How much smaller? Dividing the image area in segments and make a calibration in each segment would give the answer.

5.2 Model Data

By comparing the results from 11. December with other dates, it seems that the high resolution gives values of LWC that are close to the measured, while the low resolution gives a LWC that indicates fog, but fails to accurately predict the amount or the time of occurrence. To predict icing at a particular location, the 500 m model resolution gives better agreement than the 2.5 km resolution. It is likely that the difference is caused by the complex topography at and around the measurement site.

5.3 Starting Studies

The feasibility study of different illumination wavelengths and coherent lighting, the result from the measurement of energy required for

5.3.1. Infrared and Visible Light

image exposure and the influence of ambient light on the measurement is discussed.

5.3.1 *Infrared and Visible Light*

The amount of absorbed light in a small water droplet is close to negligible compared to the scattered light. In a large ensemble of droplets, such as a cloud, the total absorption will still be significant, especially for wavelengths in the near and far infrared. We had the opportunity to make a quick comparison of illumination using blue light (ca 450nm) and near infrared (ca 850nm). The blue light gave the sharpest image; possibly because of the higher theoretical resolving power as described by Rayleigh's criterion. But it might also partly be explained by the difference in the sensor's sensitivity for the different wavelengths. See Paper I.

5.3.2 *Laser Light*

Lasers are used in numerous optical instruments for droplet measurement, and there is good reason to. Prices for high power semiconductor lasers have become very attractive. With a laser it is possible to achieve a short light pulse with high energy. The coherency causes strong diffraction patterns, something that is used when reconstructing images in holographic imaging instruments. This makes it possible to achieve a larger measuring range than what is possible in conventional imaging, as mentioned in section 1.4.

Laser illumination was tried using two wavelengths, 450 and 850 nm, and placed in different positions. Figure 5.1 shows an example image with a 450 nm laser placed about 135 degrees from the optical center. Direct size and concentration measurement is difficult for at least following reasons:

1. The measurement volume is difficult to define because the laser light intensity is spatially inhomogenous.
2. The light intensity in the measurement point is difficult to control. Overexposure makes the glare appear larger.

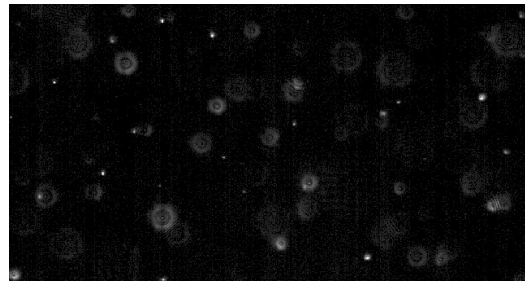


Figure 5.1: Reflections and interference patterns by droplets in 450nm laser light. The light source is placed at a position about 135 degrees from the optical center.

3. Interference patterns from particles outside the measurement volume is disturbing the measurement.

For conventional imaging of small particles the coherence mainly causes problems. Although it is possible to make the laser incoherent e.g. by using diffusers or optical fibres, it is just one of the things that makes the complete system slightly more complex.

5.3.3 *Ambient Light*

The shortest possible exposure time according to the camera specification is 0.038 ms, slightly depending on other camera settings. For each measurement 152 images were captured, with an increasing exposure time from ca 0.04 to 1.99 ms. A delay of 1 second was set between each image. Figure 5.2 shows the mean pixel value and the standard deviation of the value for one of the measurements at 22000 lux ambient light.

Using this setup it was found that an exposure time of at least one second is needed to give a signal that is comparable to the noise level under normal exposure. At the same time, in order to image small droplets, the exposure time needs to be less than one μ s. Therefore we concluded that the ambient daylight would likely have no effect on the measurement.

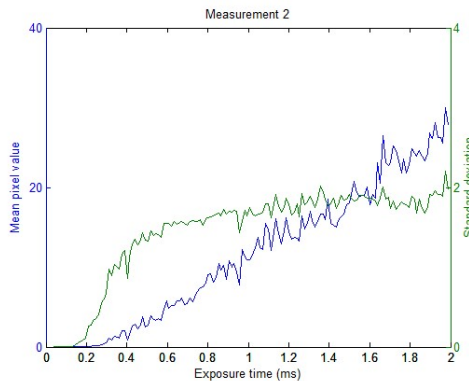


Figure 5.2: Mean pixel value and standard deviation of ambient for a light measurement at 22000 lux.

5.4 Image Noise and SNR

We observed a correlation between the SNR and the corresponding measuring range in Paper I. A higher SNR results in an increased measuring range. Even though the SNR is measured for every droplet, a compensation is not yet implemented for this. However, as was illustrated in Paper I, a higher SNR can be achieved by increasing the light intensity. Consequently, the sampling volume for every image could be increased by increasing the light intensity.

The SNR for a ten micrometer dot image was calculated using seven gain level settings of the image sensor. For each gain level, the illumination time was adjusted so that the level of exposure was the same. This measurement was done using both the 455 and the 850 nm illumination. The result can be seen in Figure 5.3. Lower gain levels require longer light pulses, but result in higher SNR. It can also be seen that the SNR for 455 nm is systematically higher than for 850 nm.

The design using a weakly collimated LED that illuminates an area slightly larger than the field of view makes the system quite insensitive to misalignment of the camera and the light source. Temporal or permanent changes in light intensity caused by a minor misalignment can be automatically compensated for by continuous measurement of

Chapter 5. Discussion

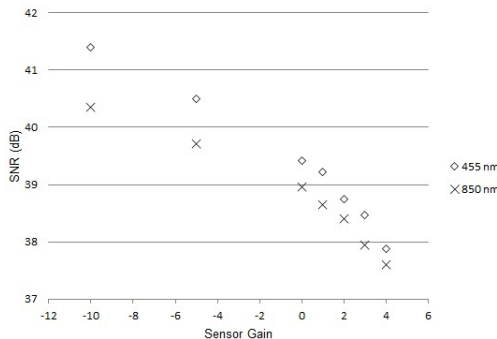


Figure 5.3: SNR for a ten micrometer dot image using two wavelengths and seven gain level settings. Shorter wavelength and lower gain gives less noise.

the total exposure level. If the level of exposure increases or decreases, the length of the light pulse is changed correspondingly. The light intensity can also be affected by dirt on the front glass of the housings.

Spatial dissimilarities in the light intensity that are not caused by noise can be compensated for by calculating the local average intensity of the background around each measured droplet. The size of a droplet is then based on the intensity dip, or modulation in amplitude, caused by the shadow compared with its local background noise, as illustrated in Figure 3.7.

5.5 Aerodynamics

Many existing instruments suffer from errors caused by the instrument itself during sampling, e.g. when droplets get stuck on the inlet or shatters into smaller droplets. The DII is not as small and aerodynamically shaped as the CDP, therefore a difference between the instruments would be expected depending on the air speed. However, a comparison between the measured values of LWC showed no correlation between the wind speed and the difference in the measured LWC. The wind speed during the comparison was only $1\text{--}4 \text{ m} \cdot \text{s}^{-1}$, which probably explains why the less aerodynamic shape of the DII compared with the CDP has no noticeable effect. This could change dramatically when measuring at higher wind speeds.

5.6. Difficulties in the Polymer Microspheres Measurement

5.6 Difficulties in the Polymer Microspheres Measurement

To verify the sizing algorithm, a measurement using polymer microspheres of four known calibrated size distributions was done. To simulate real conditions as far as possible the microspheres were applied using the same dispenser used for the calibration of the CDP. The smallest microspheres had a tendency of clogging, sometimes leading to a measurement of a clog as a single particle. Therefore all images were visually checked for false measurements. The outliers caused by false measurements were removed.

5.6.1 Clogging of Microspheres

Small microspheres form larger clogs that are measured as single microspheres. The reason may be static electricity or humidity. As was seen in the measurement of five micrometer spheres, the result of some clogs becomes outliers in the expected distribution. An example is shown in Figure 5.4. This needs to be considered when solid microspheres are used as reference objects. Colliding liquid water droplets would of course coalesce into larger droplets, thereby changing the diameter.

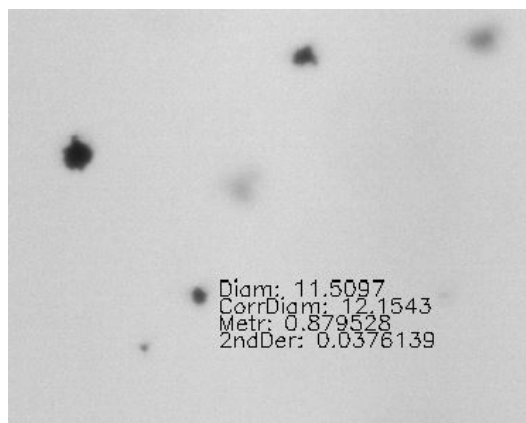


Figure 5.4: An example showing an image of clogs of five micrometer microspheres. One of the clogs are measured as a single particle, since it is round enough for the roundness qualifying criteria.

Chapter 5. Discussion

The equipment and the dispenser was thoroughly cleaned using compressed air between each measurement. Still, microspheres or other contaminations could remain, changing the distribution slightly.

Measured mean and standard deviation of all distributions were found to be within the stated calibrated values. This can be seen as a confirmation that the instrument calibrated only by the micrometer dot scale measures the microsphere samples correctly.

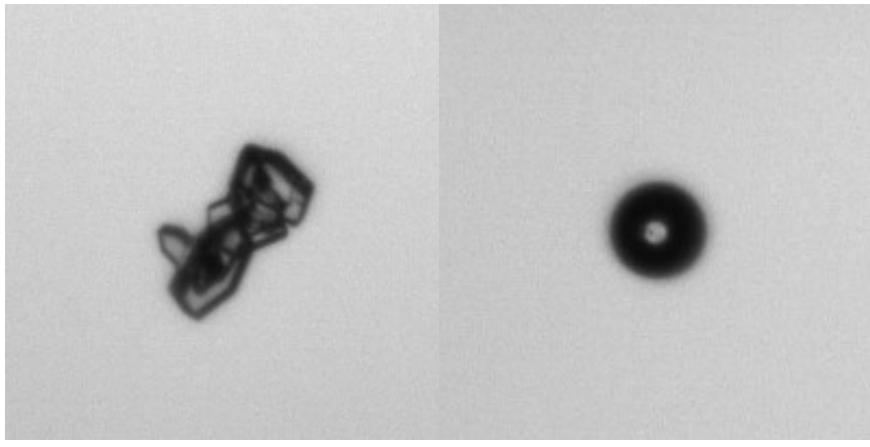
5.6.2 *Roundness*

A perfectly circular disc measured using an infinite resolution would have an expected roundness value equal to one. In practice, this is not possible to achieve in a digital image. But the contour is only used as detection criteria. Instead, the diameter is calculated using the negative shadow intensity. Therefore the contour roundness itself should have no great impact on the accuracy.

The roundness criteria defined in section 3.3.5. The roundness (3.5) limit set at 0.85 in this measurement, seems to work fine. It excludes most irregular objects, like clogs in the five micrometer measurement. When measuring fogs in cold climates, the water droplets will be mixed with ice crystals. While larger crystals will mostly be sorted out by the roundness criteria, crystals smaller than ten micrometer could present a challenge, and five micrometer ice crystals are more or less impossible to distinguish from liquid water droplets, unless they are very different in shape.

5.6.3 *Calibration Validation*

The calibration functions derived from the measurement of known-sized dots is an approximation and an interpolation. It is assumed that light scatters similarly on the edge independently of the size of the object. However, this is not quite true, especially for smaller particles [6]. For particles around ten micrometer or less in diameter we would expect a diffraction pattern with intensity variations. The pattern would be stronger the more coherent the illumination and more dominant the smaller the particle. In this system, using LED illumination, the coherence length is so short that no diffraction



(a) Ice particle.

(b) Droplet.

Figure 5.5: Difference between an ice particle and a water droplet that is $62 \mu\text{m}$ in diameter. Larger ice and snow particles tend to be more complex in shape. Ice particles smaller than $10 \mu\text{m}$ in diameter may be difficult to distinguish from water droplets.

patterns are directly visible. This may also be explained by limitations of the optical resolution. Still changes to the edge for the smallest diameters cannot be entirely ruled out.

The experiment using calibrated spheres described in Paper II, confirmed that the measurement of droplet diameters was accurate. It was, however, not a confirmation of the measurement volume, since we did not know the concentration of microspheres. This was done using the CDP as described in Paper III.

5.7 LED Illumination

Using a high power LED instead of laser reduces the interference effects used in e.g. holography [26], but since it is a monochromatic source, interference could not be completely ruled out. The coherence length for the blue LED is calculated in Paper I.

One would expect diffraction patterns depending on the spectral bandwidth of the light source. The narrower the bandwidth, the stronger the diffraction. A spectrum analysis of the LED showed that the coherence length of the blue LED is about $6.8 \mu\text{m}$. Therefore the

Chapter 5. Discussion

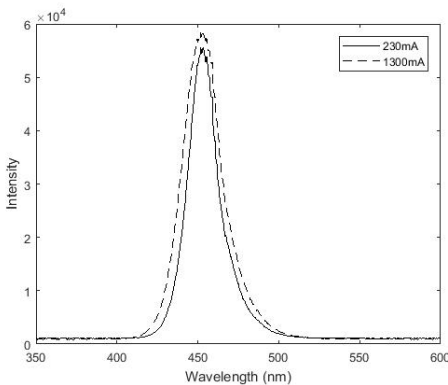


Figure 5.6: Spectrum of the Mightex 455nm LED using two different driving currents. The band width is slightly wider for the higher current.

spectrum was measured using a spectrum analyzer. The result can be seen in Figure 5.6.

LEDs can sometimes be used with currents far above the specifications, as long as the pulse length is short and the duty cycle is low enough to permit the heat generated to be transported away between the pulses. However, driving the LED with currents above the specification may affect the efficiency and aging of the LED. LED emittance also depends on the temperature. Depending on the capacitance of the diode, the rise time may limit the current, although there are techniques to shorten the LED pulses [63, 67].

The LED used was fully functional after four months of measurements using a current in the short flashes that was 12 times higher than the maximum continuous current specified by the manufacturer. At 12 ampere driving current, the flash duration could be lowered to approximately 250 ns, still using the normal settings of amplification in the camera. The LED was not tested in higher currents, but it seems possible that it could work. A question is how much current the LED can handle, and how its lifetime is affected by higher driving currents.

5.8 Statistics

A value of both LWC and MVD can be derived from a series of images and since the number of measured droplets will depend on the concentration, the accuracy and precision will depend on the number of samples from the total population of droplets.

In Paper I, we made an estimation of the precision an instrument could have using the most ideal scenario, where the “distribution” was simulated using a single dot of a known size, measured multiple times. This can be seen as a measure of the highest possible precision, defined by the physical limitations of the system components. The coefficient of variation for the LWC was estimated to 1.6 percent for droplets 25 μm in diameter, and 2.4 percent for droplets 10 μm in diameter. In practice it is difficult to compare this with the measured LWC from a real distribution of droplets. To know the exact LWC, and measure the same content is practically impossible.

In Paper III, a comparison is made by measuring polymer microspheres in distributions calibrated by NIST. As can be seen in Table 4.1, the difference between the measured mean diameter and the stated mean diameter is small. This proves that the size measurement is accurate. It was not possible to estimate the concentration of measured microspheres with the method we used. Possibly, a known concentration could be produced in a water dispersion, but then the optical ambient conditions would also be different.

5.9 Droplet Size and Distributions

Droplets that are very close are likely to coalesce, thereby decreasing the number concentration at a rate that appears to increase for larger droplets and more complex DSD [7].

Due to the small depth of the measurement volume, i.e. the measuring range compared with the field of view, the likelihood of finding two droplets very close in the image is very low due to the low number concentration of droplets we are measuring. A solution could be to measure the droplet’s circularity and add this as selection criteria for the measurement. This solution also works as a filter for ice or snow particles.

The DSD of cloud droplets 3-50 µm in diameter has usually been considered to follow a lognormal or gamma curve [52, 45, 59]. This also applies to rain [66]. However, more recent measurements of DSDs show that the distributions greatly varies [31, 60, 56, 10]. Consequently, the results will depend on the measurement method and the sampling volume.

5.9.1 Sampling Speed and Measurement Volume

Since the DII has no external trigger for the imaging, the sampling speed, i.e. the volume of air and droplets that is scanned per time unit, depends on the measuring volume of each image and the imaging speed.

The sampling speed of the CDP is linearly dependent on the wind speed. The sample area also depends on the size of the measured droplets, but the factory calibration value is given for all sizes. The sampling speed of the DII depends primarily on the image frame rate and the measurement range for each droplet size. At a wind speed of 2 m/s, the sampling speed of the CDP is $4.1 \cdot 10^{-7} \text{ m}^3 \cdot \text{s}^{-1}$. This is 39 times higher than the sampling speed of the DII for 20 µm particles. To achieve the same sampling speed, the frame rate of the DII would need to be almost 200 s^{-1} .

Despite the relatively low sampling speed and the small sampling volume of the DII, it seems that by averaging the LWC and the MVD over a period of 30 minutes, enough precision is achieved to be able to compare the two instruments. Since the purpose of the DII is primarily to detect conditions for icing on wind turbines, and provide in-situ observational data for NWP models, the achieved sampling speed may even be good enough, at least for the latter. If the speed is good enough to decide when to switch on de-icing on the blades depends on how quickly the ice builds up, and what de-icing method is used. During icing, high LWC and high MVD are expected.

When comparing the 30 min moving average values for the period 28 February – 1 March, shown in Figure 4.3a and Figure 4.2a, there is very good agreement between the curves, with the exception of 11.30-12.00 when at least ten droplets 25-35 um in diameters were measured by the DII, resulting in a significantly higher MVD and

5.9.2. Large Droplets

LWC measured by the DII than the CDP. The reason why the CDP did not measure any similarly sized particles on this particular occasion is not known. There is also a difference in the MVD when the LWC is very low resulting in a small number of measured droplets.

The sampling speed could be raised by e.g. changing the optical magnification, but then at the cost of a lower optical resolving power. It could also be increased by raising the output power of the LED, as discussed in Section 5.4 and Section 5.7.

Another way of increasing the sampling speed is to increase the imaging speed. There are cameras with a high imaging speed, and the flash pulse is so short that it would still be a low duty cycle for the LED. The most limiting factor is probably the processing time. This can be solved by implementing parts of the image processing in hardware.

Ideas to increase the sampling speed of the DII are also discussed in the attached papers.

Finally, the speed requirement depends on the application. If the instrument is used for the verification of NWP models, the sampling speed of the prototype may be enough. If the instrument is to be used for trigger de-icing, the sampling speed may need to be increased.

5.9.2 *Large Droplets*

Large droplets are important to understand the total size distribution of liquid water droplets and may play an important role during icing. The CDP does not measure particles larger than 50 µm. But if the DSD followed a lognormal, or gamma curve [52, 45] also for particles larger than 50 µm, enough large droplets should have been detected by the CDP to see an increase in the measured MVD. As demonstrated, this was not always the case. A possible explanation is that the larger cloud droplets do not follow the lognormal distribution when they are above a certain size. If this is true, the predicted MVD may be less useful for the description of a cloud DSD, as well as for conclusions about possible icing. In the case with supercooled large droplets, the LWC may be more important to measure than the MVD. But to fully understand this, a parallel measurement using an ice load instrument is required.

Figure 5.7 and Figure 5.8 show supercooled large droplets measured during the fog on 05-02-2017.

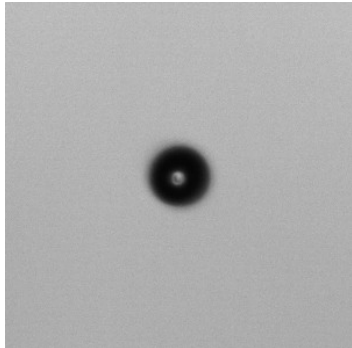


Figure 5.7: A 74 μm droplet detected at 04:41 on 05-02-2017.



Figure 5.8: Two droplets, 19 and 62 μm in diameter detected in the same image at 16:48 on 05-02-2017.

5.10 Icing

The risk of icing increases with increasing wind speed [47].

During the field study there were several instances when the LWC and MVD was high enough to lead to icing. A study to further investigate the connection between these parameters and the ice load according to ISO 12494 [48] should be carried out. An ice monitoring device, like the Combitech IceMonitor [20, 65] can be used for this. This

should preferably be done in combination with a third independent LWC and MVD measurement, e.g. by using rotating cylinders [46, 34]. A heated hygrometer measuring the True Water Content (TWC) can be used as an alternative verification of the LWC measurement when all the atmospheric water is in liquid form [62].

SUMMARY OF THE THESIS

While many of the initial questions have been answered, one is still partly unanswered. To know if the developed instrument can be used for prediction of icing, a measurement of the ice load should be done in combination with LWC and MVD. This and other possible future tasks are listed in Section 6.2

6.1 Conclusions

These are the conclusions related to the research questions RQ1-RQ5, listed in Chapter 1:

6.1.1 *RQ1*

How can the size of water droplets and their concentration be measured effectively?

- Shadowgraph imaging can be used for comparison and validation of NWP models. The technique can also be used for size reference measurement of instruments based on other techniques. The accuracy of the particle size measurement is high.

6.1.2 *RQ2*

Can the method be applied in a cost-effective instrument that meets relevant environmental and real-time requirements? How should this instrument be made physically and which components should be used?

- The DII was proven to withstand and function in a very humid environment.
- The real-time performance of the instrument is limited by the image retrieval and processing speed. There is a negative relation between the real-time performance and the precision.

Chapter 6. Summary of the Thesis

- The used LED was capable of emitting light using at least 12 times higher currents than the specified maximum.
- A better calibration of the measurement range depending on the spatial position of the measured particle, the lighting condition or the SNR is needed for a better estimation of the measurement volume.

6.1.3 RQ3

How can the instrument be tested and it's function verified in a laboratory environment?

- The test using polymer microspheres confirmed that the DII, calibrated by a micrometer dot scale measures the size of the tested samples correctly. The size distributions achieved by this instrument are within the tolerances specified by the manufacturer of the microspheres.
- The LWC in a fog chamber can be controlled by regulating the fan speed and the power of an ultrasonic humidifier.

6.1.4 RQ4 and RQ5

How can the mesasured LWC and MVD be compared and verified in field? What difference will there be using the different methods and/or instruments? Can the developed instrument be used for prediction of icing?

- The accuracy of the concentration measurement is questioned due to the systematic difference to the reference instrument, but the accuracy has the potential to become high due to the single-particle measurement range calibraiton. The precision of the instrument depends mainly on the number of images that is used to achieve each measurement value.
- The DII proved to be fully operational without site attendance for four months of continuous measurement. The instrument speed and resolution seems to be good enough to detect and measure icing conditions.

6.2. Future Work

- Both the CDP and the DII make precise measurements of the LWC using a 30 minute average window. Supercooled droplets with diameters above 50 μm in fogs where MVD is lower than predicted were measured.
- The CDP achieved higher values of the droplet diameters compared with the DII. The conclusion is that the CDP is overestimating the droplet diameter by a factor of approximately 30 percent on average.
- The predicted LWC and MVD data from HARMONIE-AROME have better agreement with the measured values when using a 500 meter horizontal resolution than the usual 2.5 km resolution.

6.2 Future Work

1. A simultaneous measurement of ice load, or ice monitoring device, should be done to find out more about the relationship between MVD, LWC and ice load. This would fully answer the last research question, RQ5.
2. A new measurement of dots to study the measurement range should be done, including e.g. different spatial positions, lighting conditions and SNR. This may find an answer to the systematic difference of the LWC measurement in Paper III.
3. The DII should be improved by increasing the image processing speed. This can be done e.g. by implementing pre-processing algorithms in hardware or by switching to a more powerful processing computer.
4. A new study may encounter higher wind speeds, which may require an even shorter flash pulse. This could require changing the hardware that drives the LED to achieve a higher current.
5. Further verification could be done using a third independent LWC and MVD measurement, e.g. by rotating cylinders [46].

Chapter 6. Summary of the Thesis

6.3 Authors' Contributions

Contributions from the authors and others are summarized in the table below.

Contributor	Paper I	Paper II	Paper III
Staffan Rydblom	MA		Survey of existing instruments and techniques for droplet measurement. Problem formulation. Estimation of the optical limitations for measurement. Choice of technique for imaging. Choice of image processing method and implementation in Matlab. Laboratory setup and method of calibration. Statistical analysis of precision.
	MA		Design and integration of the instrument and the fog chamber. Implementation of the real time measurement and analysis program in Linux/C++ with OpenCV. Measurement of polymer microspheres as reference objects. Measurement of a fog using the instrument inside the developed fog chamber and flow control.
	MA		Integration of the DII for real world measurements. Choice of reference instrument. Optimization of the measurement and analysis application. Commissioning of the DII on site and supervision of the data collection.
Benny Thörnberg	CA		Supervision of the work, discussions and advice about methods, optics and statistics. Discussion regarding the Fourier analysis of a theoretical model of a droplet.
	CA		Supervision of work. Integration of the power module for the LED flash.
	CA		Supervision. Choice of mechanics and motor for the rotation. Commissioning on site.
Esbjörn Olsson SMHI	PM		System requirements discussion and analysis.
	CA		Choice of measurement site. Theory of NWP models and implementation of the high resolution model. Weather simulations.
Patrik Jonsson Combitech	PM		Project leader at Combitech and commissioning on the measurement site.
Björn Ollars Combitech	PM		Mechanical integration of the complete rotational system on the mast and commissioning on site.
Olof Carlsson Combitech	PM		Setup and commissioning of the CDP data logging unit.
Lisa Velander	LC		

Table 6.1: Authors' contributions per article. MA = Main Author, CA = Co-Author, PM = Project Member, LR = Language Review.

ACRONYMS

AROME

Application de la Recherche à l'Opérationnel à Méso Echelle,
(Application of Research to Operations at Mesoscale)

CDP

Cloud Droplet Probe

CMOS

Complementary Metal Oxide Semiconductor

DII

Droplet Imaging Instrument

DMT

Droplet Measurement Technologies

DSD

Droplet Size Distribution

ECMWF

European Centre for Medium-Range Weather Forecasts

HARMONIE

HIRLAM (High Resolution Local Area Modelling)–ALADIN
(Aire Limitée Adaptation dynamique Développement InterNa-
tional) Research on Mesoscale Operational NWP (Numerical
Weather Prediction) in Europe

LED

light emitting diode

LWC

Liquid Water Content

Acronyms

MVD

Median Volume Diameter

NIST

National Institute of Standards and Technology

NWP

Numerical Weather Prediction

OAP

Optical Array Probe

SMHI

Sveriges meteorologiska och hydrologiska institut, (Swedish Meteorological and Hydrological Institute)

SNR

signal to noise ratio

TWC

True Water Content

BIBLIOGRAPHY

- [1] Albert Ansmann, Maren Riebesell, and Claus Weitkamp. "Measurement of atmospheric aerosol extinction profiles with a Raman lidar". In: *Optics letters* 15.13 (1990), pp. 746–748.
- [2] D. Baumgardner. "An Analysis and Comparison of 5 Water Droplet Measuring-Instruments". In: *Journal of Climate and Applied Meteorology* 22.5 (1983), pp. 891–910.
- [3] D. Baumgardner et al. "Airborne instruments to measure atmospheric aerosol particles, clouds and radiation: A cook's tour of mature and emerging technology". In: *Atmospheric Research* 102.1-2 (2011), pp. 10–29.
- [4] D Baumgardner et al. "The cloud, aerosol and precipitation spectrometer: a new instrument for cloud investigations". In: *Atmospheric research* 59 (2001), pp. 251–264.
- [5] Hans Bergström et al. *Wind power in cold climates: Ice mapping methods*. Elforsk AB, 2013.
- [6] Craig F Bohren and Donald R Huffman. *Absorption and scattering of light by small particles*. John Wiley & Sons, 2008.
- [7] Róbert Bordás et al. "Droplet collisions and interaction with the turbulent flow within a two-phase wind tunnel". In: *Physics of Fluids (1994-present)* 23.8 (2011), p. 085105.
- [8] Rolv Erlend Bredesen et al. *IEA Wind Recommended Practices 13, Edition 2: Wind Energy Projects in Cold Climates*. Tech. rep. 2017.
- [9] John Canny. "A computational approach to edge detection". In: *Pattern Analysis and Machine Intelligence, IEEE Transactions on* 6 (1986), pp. 679–698.
- [10] Stewart G Cober and George A Isaac. "Characterization of aircraft icing environments with supercooled large drops for application to commercial aircraft certification". In: *Journal of Applied Meteorology and Climatology* 51.2 (2012), pp. 265–284.

Bibliography

- [11] Stewart G Cober, George A Isaac, and J Walter Strapp. "Characterizations of aircraft icing environments that include supercooled large drops". In: *Journal of Applied Meteorology* 40.11 (2001), pp. 1984–2002.
- [12] Ruben D Cohen. "Shattering of a liquid drop due to impact". In: *Proceedings of the Royal Society of London A: Mathematical, Physical and Engineering Sciences*. Vol. 435. The Royal Society, 1991, pp. 483–503.
- [13] Paul J. Connolly et al. "Calibration of the Cloud Particle Imager Probes Using Calibration Beads and Ice Crystal Analogs: The Depth of Field". In: *Journal of Atmospheric and Oceanic Technology* 24.11 (2007), pp. 1860–1879.
- [14] N Dalili, A Edrisy, and R Carriveau. "A review of surface engineering issues critical to wind turbine performance". In: *Renewable and Sustainable Energy Reviews* 13.2 (2009), pp. 428–438.
- [15] Neil Davis et al. "Forecast of icing events at a wind farm in Sweden". In: *Journal of Applied Meteorology and Climatology* 53.2 (2014), pp. 262–281.
- [16] S Dierer, R Oechslin, and R Cattin. "Wind turbines in icing conditions: performance and prediction". In: *Advances in Science and Research* 6 (2011), p. 245.
- [17] James E Dye and Darrel Baumgardner. "Evaluation of the forward scattering spectrometer probe. Part I: Electronic and optical studies". In: *Journal of Atmospheric and Oceanic Technology* 1.4 (1984), pp. 329–344.
- [18] Jordi Estevadeordal and Larry Goss. "PIV with LED: particle shadow velocimetry (PSV)". In: *43rd AIAA aerospace sciences meeting and exhibit, meeting papers*. 2005, pp. 12355–12364.
- [19] PR Field, AJ Heymsfield, and A Bansemer. "Shattering and particle interarrival times measured by optical array probes in ice clouds". In: *Journal of Atmospheric and Oceanic Technology* 23.10 (2006), pp. 1357–1371.

- [20] S Fikke et al. "COST 727: Atmospheric Icing on structures". In: *Measurements and data collection on icing: State of the Art, Publication of MeteoSwiss* 75.110 (2006), pp. 1422–1381.
- [21] Karen J Finstad, Edward P Lozowski, and Lasse Makkonen. "On the median volume diameter approximation for droplet collision efficiency". In: *Journal of the atmospheric sciences* 45.24 (1988), pp. 4008–4012.
- [22] Rafael C Gonzales and Richard E Woods. *Digital Image Processing, 2-nd Edition*. 2002.
- [23] Gösta H Granlund. "Fourier preprocessing for hand print character recognition". In: *IEEE transactions on computers* 100.2 (1972), pp. 195–201.
- [24] George M Hale and Marvin R Querry. "Optical constants of water in the 200-nm to 200- μm wavelength region". In: *Applied optics* 12.3 (1973), pp. 555–563.
- [25] Yiqiang Han, Jose Palacios, and Sven Schmitz. "Scaled ice accretion experiments on a rotating wind turbine blade". In: *Journal of Wind Engineering and Industrial Aerodynamics* 109 (2012), pp. 55–67.
- [26] J Henneberger et al. "HOLIMO II: a digital holographic instrument for ground-based in situ observations of microphysical properties of mixed-phase clouds". In: *Atmospheric Measurement Techniques* 6.11 (2013), pp. 2975–2987.
- [27] Matthew C. Homola, Per J. Nicklasson, and Per A. Sundsbø. "Ice sensors for wind turbines". In: *Cold Regions Science and Technology* 46.2 (2006), pp. 125–131.
- [28] Matthew C. Homola et al. "Effect of atmospheric temperature and droplet size variation on ice accretion of wind turbine blades". In: *Journal of Wind Engineering and Industrial Aerodynamics* 98.12 (2010), pp. 724–729.
- [29] Matthew C Homola et al. "Performance losses due to ice accretion for a 5 MW wind turbine". In: *Wind Energy* 15.3 (2012), pp. 379–389.

Bibliography

- [30] Robert F Ide. *Comparison of Liquid Water Content Measurement Techniques in an Icing Wind Tunnel*. Tech. rep. DTIC Document, 1999.
- [31] AR Jameson and AB Kostinski. "What is a raindrop size distribution?" In: *Bulletin of the American Meteorological Society* 82.6 (2001), pp. 1169–1177.
- [32] William J Jasinski et al. "Wind turbine performance under icing conditions". In: *Journal of Solar Energy Engineering* 120.1 (1998), pp. 60–65.
- [33] Ville A Kaikkonen, Dmitry Ekimov, and Anssi J Makynen. "A holographic in-line imaging system for meteorological applications". In: *IEEE Transactions on Instrumentation and Measurement* 63.5 (2014), pp. 1137–1144.
- [34] Daniel Knezevici, Richard Kind, and Myron Oleskiw. "Determination of Medium Volume Diameter (MVD) and Liquid Water Content (LWC) by Multiple Rotating Cylinders". In: *43rd AIAA Aerospace Sciences Meeting and Exhibit*. 2005, p. 861.
- [35] Robert G Knollenberg. "The optical array: An alternative to scattering or extinction for airborne particle size determination". In: *Journal of Applied Meteorology* 9.1 (1970), pp. 86–103.
- [36] AV Korolev, JW Strapp, and GA Isaac. "Evaluation of the accuracy of PMS optical array probes". In: *Journal of Atmospheric and Oceanic Technology* 15.3 (1998), pp. 708–720.
- [37] AV Korolev et al. "Evaluation of measurements of particle size and sample area from optical array probes". In: *Journal of Atmospheric and Oceanic Technology* 8.4 (1991), pp. 514–522.
- [38] Linhong Kou, Daniel Labrie, and Petr Chylek. "Refractive indices of water and ice in the 0.65-to 2.5- μm spectral range". In: *Applied optics* 32.19 (1993), pp. 3531–3540.
- [39] Bjørn Egil Kringlebotn Nygaard, Jón Egill Kristjánsson, and Lasse Makkonen. "Prediction of In-Cloud Icing Conditions at Ground Level Using the WRF Model". In: *Journal of Applied Meteorology and Climatology* 50.12 (2011), pp. 2445–2459.

- [40] Thomas Kuhn, Igor Grishin, and JJ Sloan. "Improved imaging and image analysis system for application to measurement of small ice crystals". In: *Journal of Atmospheric and Oceanic Technology* 29.12 (2012), pp. 1811–1824.
- [41] Pramod Kulkarni, Paul A Baron, and Klaus Willeke. *Aerosol measurement: principles, techniques, and applications*. John Wiley & Sons, 2011.
- [42] Fayçal Lamraoui et al. "Atmospheric icing impact on wind turbine production". In: *Cold Regions Science and Technology* 100 (2014), pp. 36–49.
- [43] S Lance et al. "Water droplet calibration of the Cloud Droplet Probe (CDP) and in-flight performance in liquid, ice and mixed-phase clouds during ARCPAC". In: *Atmospheric Measurement Techniques* 3.6 (2010), pp. 1683–1706.
- [44] RP Lawson and RH Cormack. "Theoretical design and preliminary tests of two new particle spectrometers for cloud microphysics research". In: *Atmospheric research* 35.2 (1995), pp. 315–348.
- [45] Seungwon Lee, Brian H Kahn, and João Teixeira. "Characterization of cloud liquid water content distributions from CloudSat". In: *Journal of Geophysical Research: Atmospheres* 115.D20 (2010).
- [46] L. Makkonen. "Analysis of Rotating Multicylinder Data in Measuring Cloud-Droplet Size and Liquid Water-Content". In: *Journal of Atmospheric and Oceanic Technology* 9.3 (1992), pp. 258–263.
- [47] Lasse Makkonen. "Models for the growth of rime, glaze, icicles and wet snow on structures". In: *Philosophical Transactions of the Royal Society of London A: Mathematical, Physical and Engineering Sciences* 358.1776 (2000), pp. 2913–2939.
- [48] Lasse Makkonen, Pertti Lehtonen, and Mika Hirviniemi. "Determining ice loads for tower structure design". In: *Engineering Structures* 74 (2014), pp. 229–232.

Bibliography

- [49] Lasse Makkonen et al. "Modelling and prevention of ice accretion on wind turbines". In: *Wind Engineering* 25.1 (2001), pp. 3–21.
- [50] David Marr and Ellen Hildreth. "Theory of edge detection". In: *Proceedings of the Royal Society of London. Series B. Biological Sciences* 207.1167 (1980), pp. 187–217.
- [51] Gustav Mie. "Beiträge zur Optik trüber Medien, speziell kolloidaler Metallösungen". In: *Annalen der physik* 330.3 (1908), pp. 377–445.
- [52] Natasha L Miles, Johannes Verlinde, and Eugene E Clothiaux. "Cloud droplet size distributions in low-level stratiform clouds". In: *Journal of the atmospheric sciences* 57.2 (2000), pp. 295–311.
- [53] B. E. K. Nygaard, J. E. Kristjansson, and L. Makkonen. "Prediction of In-Cloud Icing Conditions at Ground Level Using the WRF Model". In: *Journal of Applied Meteorology and Climatology* 50.12 (2011), pp. 2445–2459.
- [54] International Standardization Organization. *ISO 12181-1: 2011, Geometrical Product Specifications (GPS)-Roundness-Part 1: Vocabulary and parameters of roundness*. 2011.
- [55] Olivier Parent and Adrian Ilinca. "Anti-icing and de-icing techniques for wind turbines: Critical review". In: *Cold regions science and technology* 65.1 (2011), pp. 88–96.
- [56] Gerhard Peters et al. "Profiles of raindrop size distributions as retrieved by microrain radars". In: *Journal of applied meteorology* 44.12 (2005), pp. 1930–1949.
- [57] T Reisinger et al. "On the relative intensity of Poisson's spot". In: *New Journal of Physics* 19.3 (2017), p. 033022.
- [58] Wayne R Sand et al. "Icing conditions encountered by a research aircraft". In: *Journal of climate and applied meteorology* 23.10 (1984), pp. 1427–1440.
- [59] John H Seinfeld, Spyros N Pandis, and Kevin Noone. *Atmospheric chemistry and physics: from air pollution to climate change*. 1998.

- [60] RA Shaw, AB Kostinski, and ML Larsen. "Towards quantifying droplet clustering in clouds". In: *Quarterly journal of the royal meteorological society* 128.582 (2002), pp. 1043–1057.
- [61] Jaiwon Shin and Thomas H Bond. *Results of an icing test on a NACA 0012 airfoil in the NASA Lewis Icing Research Tunnel*. National Aeronautics and Space Administration, 1992.
- [62] J. K. Spiegel et al. "Evaluating the capabilities and uncertainties of droplet measurements for the fog droplet spectrometer (FM-100)". In: *Atmospheric Measurement Techniques* 5.9 (2012), pp. 2237–2260.
- [63] Hiroyuki Tanaka, Yohtaro Umeda, and Osamu Takyu. "High-speed LED driver for visible light communications with drawing-out of remaining carrier". In: *Radio and Wireless Symposium (RWS), 2011 IEEE*. IEEE, 2011, pp. 295–298.
- [64] Gregory Thompson et al. "Using the Weather Research and Forecasting (WRF) model to predict ground/structural icing". In: *13th International Workshop on Atmospheric Icing on Structures, METEOTEST, Andermatt, Switzerland*. 2009.
- [65] Petra Thorsson, Stefan Söderberg, and Hans Bergström. "Modelling atmospheric icing: A comparison between icing calculated with measured meteorological data and NWP data". In: *Cold Regions Science and Technology* 119 (2015), pp. 124–131.
- [66] Carlton W Ulbrich. "Natural variations in the analytical form of the raindrop size distribution". In: *Journal of Climate and Applied Meteorology* 22.10 (1983), pp. 1764–1775.
- [67] Omar Veledar et al. "Simple techniques for generating nanosecond blue light pulses from light emitting diodes". In: *Measurement Science and Technology* 18.1 (2007), p. 131.
- [68] Timothy P Wallace and Paul A Wintz. "An efficient three-dimensional aircraft recognition algorithm using normalized Fourier descriptors". In: *Computer Graphics and Image Processing* 13.2 (1980), pp. 99–126.

Bibliography

- [69] AD Ward, M Zhang, and O Hunt. "Broadband Mie scattering from optically levitated aerosol droplets using a white LED". In: *Optics express* 16.21 (2008), pp. 16390–16403.
- [70] M Wendisch, A Keil, and AV Korolev. "FSSP characterization with monodisperse water droplets". In: *Journal of Atmospheric and Oceanic Technology* 13.6 (1996), pp. 1152–1165.
- [71] Manfred Wendisch and Jean-Louis Brenguier. *Airborne measurements for environmental research : methods and instruments*. Wiley Series in Atmospheric Physics and Remote Sensing. Weinheim: Wiley-VCH, 2013.
- [72] CD Westbrook et al. "Estimating drizzle drop size and precipitation rate using two-colour lidar measurements". In: *Atmospheric Measurement Techniques* 3.3 (2010), pp. 671–681.
- [73] C. Willert et al. "Pulsed operation of high-power light emitting diodes for imaging flow velocimetry". In: *Measurement Science and Technology* 21.7 (2010), p. 075402.

Paper I

Liquid Water Content and Droplet Sizing Shadowgraph Measuring System for Wind Turbine Icing Detection

S. Rydblom, B. Thörnberg

Liquid Water Content and Droplet Sizing Shadowgraph Measuring System for Wind Turbine Icing Detection

Staffan Rydblom and Benny Thörnberg

Abstract—This paper shows that the liquid water content (LWC) and the median volume diameter (MVD) can be derived from the images of water droplets using a shadowgraph imaging system with incoherent LED illumination. Icing on structures, such as a wind turbine, is the result of a combination of LWC and MVD, and other parameters, such as temperature, humidity, and wind speed. Today, LWC and MVD are not commonly measured for wind turbines. Systems for measuring these properties are often expensive or impractical in terms of location or remote reading. The aim of this paper is to gain knowledge about how to design a single instrument based on imaging that has the ability to measure these properties with enough precision and accuracy to detect icing conditions for wind turbines. A method to calculate both the LWC and the MVD from the same images is described in this paper. The size of one droplet is determined by measuring the shadow created by the droplet in background illumination. The concentration is calculated by counting the measured droplets and estimating the volumes in which these droplets can be observed. In this paper, the observation volume is shown to be dependent on the particle size and the signal-to-noise ratio for each measured particle. An expected coefficient of variation of the LWC depending on the droplet size is shown to be 2.4% for droplets 10 μm in diameter and 1.6% for 25- μm droplets. This is based on an error estimation of the laboratory measurements calibrated using a micrometer dot scale.

Index Terms—Clouds, image processing, machine vision, meteorology, optical microscopy, wind power generation.

I. INTRODUCTION

ICING caused by freezing atmospheric water is a problem for the generation of electrical energy from wind in cold climates. Unless prevented, it may lead to lower performance or to the wind turbines stopping completely [1]–[4]. Aircraft, power lines or any other weather exposed structure share this problem. Therefore big efforts have been made to create models for how the ice is formed [5], [6] and how it can be included in weather prediction models [7], [8].

The icing process is complex and the result depends on a combination of the aerodynamic shape of the structure or airfoil, the velocity of the air and its contained water, the temperature, the mixing of snow and water, the concentration of liquid water and the droplet size distribution. All droplets or particles passing the airfoil are affected by a force

created by the change in pressure surrounding the airfoil. To hit the surface and take part in the icing process they must have enough mass and density. Smaller droplets and less dense particles are pushed into a diverting, non-impact trajectory [5]. The liquid water content (LWC) and the water droplets median volume diameter (MVD) are essential input parameters to predict or model icing. Although there do exist methods, as we will discuss, to measure these properties, they are scarcely ever measured at a planned or existing wind turbine [9], [10]. Measuring them accurately and frequently would be an advantage for the planning of new wind mill farms or for the application of anti-icing arrangements on existing power stations. It may be of particular interest as input to weather prediction models by which both LWC and MVD can be computed [7], [8]. In combination with information about the aerodynamic properties of the wind turbine, it can give more accurate predictions of icing or even result in better design of wind turbines and anti-icing methods.

While icing caused by large supercooled droplets, with diameters from approximately 50 μm to exceeding 1000 μm , is often considered severe due to its shape and quick build-up, icing may occur even with droplets as small as 5 μm [11]–[13]. In most cases, though, icing is caused by cloud droplets measuring between 10 μm and 30 μm in diameter [10], [12].

Although optical imaging and other techniques for measuring aerosol properties is continuously improving, the choice of instrument is still very much dependent on the application's requirements [14]–[17]. An instrument for measuring icing parameters for wind turbines should be able to detect supercooled cloud droplets from five micrometer and determine an accurate measure of the LWC. Since measurements are needed in multiple remote locations it should also be affordable, reliable, have low power consumption, and ideally be possible to place near the highest point of the turbine [18].

A. Contributions

We describe a shadowgraph system consisting of a monochrome digital image sensor with a telecentric lens and a collimated LED illumination. A method for segmentation of objects from image background, based on the second derivative of the intensity is proposed.

We show that calibration of true droplet size and measuring range both depends on the measured size of the droplet shadow and the amount of light used for exposure. We show that it is possible to predict both the precision of the measured size and accuracy for measurement of droplet size.

Manuscript received November 25, 2015; revised January 12, 2016; accepted January 12, 2016. Date of publication January 18, 2016; date of current version February 24, 2016. This work was supported by Energimyndigheten. The associate editor coordinating the review of this paper and approving it for publication was Prof. Bernhard Jakoby.

The authors are with Mid Sweden University, Sundsvall 851 70, Sweden (e-mail: staffan.rydblom@miun.se; benny.thornberg@miun.se). Digital Object Identifier 10.1109/JSEN.2016.2518653

1558-1748 © 2016 IEEE. Translations and content mining are permitted for academic research only. Personal use is also permitted, but republication/redistribution requires IEEE permission. See http://www.ieee.org/publications_standards/publications/rights/index.html for more information.

A value of both MVD and LWC can be derived from a series of images and since the number of measured droplets will depend on the concentration, the accuracy and precision will depend on the number of samples from the total population of droplets.

Many existing instruments suffer from errors caused by the instrument itself during sampling, e.g. when droplets get stuck on the inlet [19], or shatters into smaller droplets [20]. An instrument should be designed in order to affect the free flow of particles as little as possible [16]. Therefore we also investigate the illuminative power required to get a good exposure with the tested system at a targeted maximum wind speed of 50 m/s.

In this study, we have used a stage micrometer scale for characterization of the system and simulation of water droplets. This characterization holds true given that the optical silhouette of droplet is comparable to a dot having equal diameter and being printed on a silicon glass. It is not a new concept and has at least once been proved experimentally for coherent light, by comparing with beads of glass and water droplets of known sizes [21]. The shadow image of water drops of any size will be defined mainly by the diffracted component, as long as the distance between the drop and the lens is much larger than the drop diameter. Only in a small bright spot in the middle will the refracted component be large enough to be visible in a shadowgraph system [21], [22].

Using the results of this study, a weather protected prototype may be built to perform a comparative study.

We believe that this study of a shadowgraph imaging system provides good analysis of its expected major limitations related to the measurement of liquid water content of air. This is also the scientific contribution of this publication.

B. Related Work

In 1970, Knollenberg [23] described an electro-optical technique to measure cloud and precipitation particles using a laser illuminated linear array of photo detectors. The photo detectors are used to make a two-dimensional image of the particles' shadows as they pass the light beam. Systems based on this technique are called Optical Array Probes (OAP) or two-dimensional imaging probes. Later development of this technique includes using image sensors to save gray scale images of the detected particles [17], [22].

One popular technique to measure single particles used in several instruments is to measure the light scattered from a focused laser [15], [24]. A laser beam is used to illuminate passing particles. When a particle is detected, its size is determined by comparing the variations in light with a pattern calculated from the Mie scattering theory [25].

Since the OAP, its successors and the scattering spectrometers have advantages over the other depending on the size and nature of the aerosol, instruments for airborne use have been developed that combine several techniques into one single probe [26] for accurate measuring of LWC and MVD [16].

A different optical technique for measuring water droplets is based on in line holography [27]. In principle this is a two-dimensional shadowgraph imaging system that use laser

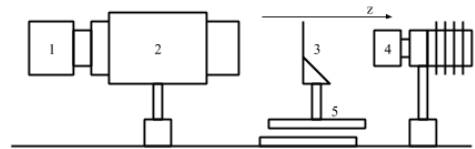


Fig. 1. The optical setup: 1) camera, 2) Lens, 3) Holder for micrometer scale, 4) LED with collimating lens, and 5) Translation stage.

background illumination to create images of the diffraction patterns created by the passing particles. These patterns are measured to reconstruct images of the particles. This is a fairly calculation intensive process, which may be one of the reasons why instruments based on this technique are not so common [28].

Sizing of the droplets using Mie spectrometry is a complex operation even for coherent light [29], and although it is possible to study Mie scattering from white light [30], the complexity, small droplet size range and sample volume makes it less attractive in this application. The optical resolution is usually too low. Therefore it is also difficult to determine the exact particle size and the usable depth of field for incoherent shadowgraph systems. The shadow from a particle can e.g. appear smaller or larger when out of focus.

Shadowgraph imaging of particles using incoherent illumination instead of laser has been tried e.g. in particle shadow velocimetry (PSV) [31], [32], or spray characterization [33]. Quantitative and comprehensive studies of other droplet measurement techniques exist [24], [28], [34]. But to our knowledge there is no publication providing an equal analysis of a shadowgraph system using incoherent light for droplet measurement. We believe this study provides a good base for the design of a shadowgraph system for particle measurement using incoherent illumination.

II. MATERIALS AND METHODS

The experimental setup is illustrated in Fig. 1. The camera (1) is mounted on a telecentric lens (2) and fixed in line with a holder for a test object (3) and the backlight illumination (4). The object holder was mounted on a translation stage (5) to move the object in the z-direction.

A. Materials and Methods

The camera used throughout this study was the uEye UI-3370CP-NIR. It contains a monochrome CMOS digital image sensor, CMOSIS CMV4000, with 12 μm epilayer for improved spectral response in the near infrared (700 to 900 nm). The sensor has 2048 \times 2048 active pixels on a 5.5 μm pitch. The image array has pipelined global shutter pixels which allow exposure during read out, while performing CDS (correlated double sampling) operation. The image sensor has sixteen 10- or 12-bit serial outputs. It also integrates a programmable gain amplifier and offset regulation. Each channel runs at 480 Mbps maximum which results in 180 fps frame rate at full resolution (10-bit mode).

The background illumination was produced using an LED, Mightex LCS-0455-03, with a 22 mm collimating lens. The LED produces low-coherent light in a spectra with its peak intensity at 455 nm (blue). The 22 mm lens produced a square beam approximately 8 times 8 mm. According to Mightex, the half diverging angle using 22 mm aperture is 1.7 degrees.

The lens was a telecentric lens, Opto Engineering TC4M004-C, with 4.04 \times magnification according to the delivery test report. With the described camera it gives an object field of view of 2.79 times 2.79 mm. The working f/# is 22 and the depth of field is given to approximately 0.1 mm. Depth of field is discussed more extensively in chapter IV. The given lens was tested at delivery for telecentricity in four image zones, from the center to the edge, giving a telecentric slope from 0.015 and 0.091 degrees. This means that the maximum error for a displacement of 1 mm would be less than 1.5 micron in a corner of the lens, and less than 0.3 micron in the center.

A stage micrometer scale, Edmund Optics #58-606, with dots printed in chrome on a silicon glass was used as reference object. The pattern scale featured printed dots in diameters of 2 μ m, 3 μ m, 4 μ m, 5 μ m, 6 μ m, 7 μ m, 8 μ m, 9 μ m, 10 μ m, 25 μ m, 50 μ m, 75 μ m and 100 μ m. It was mounted on a translation stage that was used to automatically move the object in steps of two micrometers between the images. The distance between each step is called the delta distance Δz . See Fig. 5. The measuring range corresponds to the delta distance at which the reference object could be detected using the proposed method for image segmentation.

B. Image Edge Detection

The reason for using edge detection is that the edge response can be used both for measuring the size of the droplets and to define the measurement volume. Droplets with too weak edge response would be outside the measurement volume.

In this study we have used a Laplacian of Gaussian [35] edge detection filter implemented as a 13 \times 13 size convolution kernel. This method is attractive in digital image processing applications since the Laplacian derivation and the Gaussian blurring filter can be combined in a single convolution kernel, thus reducing the necessary number of multiplications to process a complete image. Blurring before derivation is needed to reduce the sensitivity to noise in the image. The result is an image of the second order derivative that is near zero very close to an edge and in regions far away from an edge. The Laplacian for a two dimensional function (image) $f(x,y)$ is defined in Eq 1.

$$\nabla^2 f = \frac{\delta^2 f}{\delta x^2} + \frac{\delta^2 f}{\delta y^2} \quad (1)$$

The second order derivative is positive on one side of the edge and negative on the other side [36]. We look for zero crossings in the x- and y-directions of the filtered image, i.e. where the value is negative/positive on one side and positive/negative on the other. A threshold is set to the absolute value of the difference between the negative and positive value greater than zero and these crossings are marked in a new image. The result

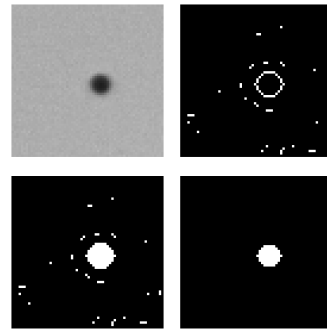


Fig. 2. Ten micrometer dot (upper left), edge detected (upper right), filled (lower left) and subtracted to a single blob (lower right).

is a binary image with contours marking the objects that have sharp edges. See Fig 2, upper right.

C. Object Identification

Using the edge detected binary image, we apply a boundary fill function (Fig. 2, lower left). The boundary fill detects closed contours in binary images like the one shown (Fig. 2, upper right), that are not in contact with the edge of the image and alters the value of the pixels within the boundary. The filled boundaries are identified as objects to be measured by subtracting the filled image with the original edge binary (Fig. 2, lower right).

D. Object Size Measurement

The cross sectional area of each identified object is determined by counting the number of pixels in its filled boundary. From the cross sectional area we calculate the uncorrected diameter by using the magnification of the lens and the pixel size of the image sensor.

E. Measuring Signal to Noise Ratio

The noise in an image is the non-deterministic modulation σ_j stemming from photon quantization, thermal energy, spatial sensitivity variations and more. Its magnitude depends both on the camera sensor's SNR and the variation in intensity of the light beam. In particular the intensity may differ from one image to another, depending on e.g. the LED temperature, the length and power of the electrical pulse and external disturbances in the optical path. Therefore we construct a method to calculate the signal to noise ratio (snr_j) for every measured particle j . The noise σ_j is measured from the background signal around each particle j . The signal is the impact, or the amplitude, A_j , of the shadows caused by the drop. The snr is the relation between the signal and the noise.

$$\text{snr}_j = 20 \log \frac{A_j}{\sigma_j} \quad (2)$$

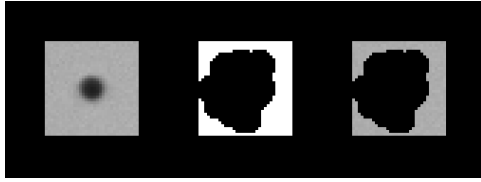


Fig. 3. Background noise. The image is cropped to a square (left) around the particle j (arrowed). The size of the square depends on the size of the particle. A black mask (middle) is calculated to get the background noise signal (right) containing all $x_{i,j}$ for particle j .

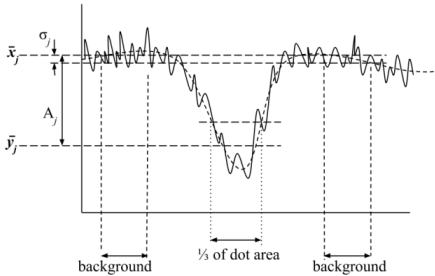


Fig. 4. SNR calculation. \bar{y}_j is determined by calculating the average of the darkest third of all pixels inside the edge detected dot.

where

$$A_j = |\bar{x}_j - \bar{y}_j| \quad (3)$$

and

$$\sigma_j = \sqrt{\frac{1}{N} \sum_{i=1}^N (x_{i,j} - \bar{x}_j)^2} \quad (4)$$

A_j is the difference between \bar{x}_j and \bar{y}_j . \bar{y}_j is the mean of one third of the smallest values in the area covered by the filled blob constructed from the edge detection. See illustrations in Fig. 2, and Fig. 4. $x_{i,j}$ is each of the N pixel values of the background noise surrounding particle j . To exclude pixels that may be affected by the diffraction from the light passing, we used a five pixel large disk shaped structure to dilate the original boundary. Therefore the pixels immediately next to the edge-detected boundary are not counted in the SNR calculation. \bar{x}_j is the mean of $x_{i,j}$ for each particle j . See Fig. 3 and Fig. 4.

The background is limited to an equal-sided square surrounding each measured object with the side equal to the size of the edge detected multiplied by two, plus ten pixels.

Defining the SNR in this way makes it possible to determine an individual SNR for every measured object in an image. True size and detection range can then be calibrated depending on its measured size and SNR.

F. Creating Calibration Tables

A translation stage is used to move the object in steps from closer than in focus to further away than the focus of the lens. All the dot images are then analyzed using the same method

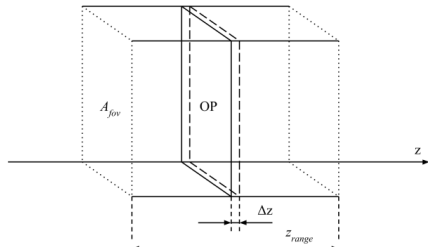


Fig. 5. The imaginary measurement volume confined by the area A_{fov} and the measuring range z_{range} . A_{fov} is the visible area limited by the field of view. z_{range} is the average number of detection events during a linear translation of the object in the z-direction times the translation delta Δz . OP is the plane of the reference object.

as the one that will be used to measure droplets. Since the dots are of known size and are expected to give a similar shadowgraph image as the droplets, the results are translated into two calibration tables.

The first calibration table is a list of the mean deviation between measured and actual diameter. This table is interpolated and expressed as a function, or correction factor f of the measured diameter, d^M . The true diameter, d^T , can be derived by subtracting the correction factor.

$$d^T = d^M - f(d^M) \quad (5)$$

The second calibration table is a list of the ranges in the distance from the camera where the droplets of a given size are expected to be detected with the chosen method. Given a method (camera, optics, and detection algorithm) this range, z_{range} , will depend on both the true diameter, d^T , and the signal to noise ratio snr_j .

$$z_{range} = g(d^T, \text{snr}_j) \quad (6)$$

Therefore, to estimate the measurement volume of a particle, the true diameter d^T , and the snr_j , must first be calculated.

G. Measurement Volume and Measuring Range

Fig. 5 illustrates the imaginary volume. Since the camera lens is telecentric, the field of view defined by the area A_{fov} is approximately the same in all positions on the z-axis. The maximum telecentric error of the lens is 0.091 degrees at the corners. At the maximum measured distance from object plane, 1.5 mm, the maximum lateral error would then be $1500 \sin 0.091 = 2.4 \mu\text{m}$. On the area A_{fov} , this corresponds to an error of less than 0.17 percent. When an object is translated in fixed steps in the z-direction, the number of detections will define a range, z_{range} , that together with A_{fov} confines a measuring volume, V_i , for a particle i of a given size.

$$V_i = z_{range} A_{fov} \quad (7)$$

This volume is the imaginary volume in which one particle with the same shadow image as the reference object, if present,

should be detected on average. If m calibration objects are detected when moved in steps of Δz in the complete depth of field, the measuring range $z_{range} = m \Delta z$.

A boundary fill function was used to distinguish closed contours from not closed contours. The range is given by the number of closed contours from one or several image series within the range times the step size between each translation in the direction from the camera. Contours that are not closed will not be counted in the range.

H. Liquid Water Content

Each detected particle with mass m_j , has a corresponding expected detection volume, V_j , which is determined by the area of view and the range in focus where the particles of that size are expected to be detected.

The LWC from one image is given by the sum of all the n detected particles' masses of that image, divided by their respective expected detection volumes in that image.

$$LWC = \sum_{j=1}^n \frac{m_j}{V_j} \quad (8)$$

If several images are made, the mean LWC is given by the sum divided by the number of images.

Using the method described to find droplets one may need to consider the case where two or more droplets are close enough to be interpreted as one. To deal with this possibility we use a threshold on the symmetry, the major axis divided by the minor axis, and the compactness [37], to exclude non-circular objects from the calculation. In Chapter IV, we discuss this further.

I. Median Volume Diameter

The median volume diameter, MVD, is given at the point where half of the total volume of liquid content in a fixed air volume consists of droplets with diameters larger and the other half has smaller diameters. Compared with the mean volume droplet diameter and the mean droplet diameter, the MVD has been shown to give the best approximation to the mean collision efficiency of supercooled droplets [38].

To get the MVD from one image, we first calculate the LWC for that image. Then we sort all $\frac{m_j}{V_j}$ and count the index number j until we get the sum $LWC/2$. The MVD is given by the mean of the last counted particle's diameter and the diameter of the next uncounted particle.

To average the MVD of several images we need to weigh the MVD with the LWC for each image. If we have m images, and give the properties of each image the index k , the average MVD for all images is:

$$\overline{MVD} = \frac{\sum_{k=1}^m (MVD_k LWC_k)}{\sum_{k=1}^m LWC_k} \quad (9)$$

J. Measurement of Droplets in Air

Before a measurement starts, the calibration tables f and g for size and volume determination are read. The tables

are translated into calibration lookup tables using linear interpolation.

The image is captured and transferred from the camera or the disk memory, and edge detected using an edge detection algorithm.

After the edge detection, objects are qualified as droplets, and an uncorrected diameter is determined for each of these. For each detected droplet j the signal to noise ratio, snr_j , is determined.

Given the measured diameter d^M of every particle, a corrected true diameter d^T is calculated by subtracting the corresponding value in the calibration lookup table.

Using the true diameter, d^T , the particle's volume and mass is calculated. Its mass, m_j , is determined from the density of water, which in this study is approximated to $\rho = 1 \text{ g/cm}^3$.

LWC and MVD are calculated using the data from one or several images.

K. Investigation of Ambient Light

The level of ambient light in the optics lab was too low to give any contribution to the exposure during the experiment. Therefore, an experiment was carried out outside in daylight. An ultrasonic fog generator was used to simulate a fog spreading the ambient light into the telecentric lens. The generator was set on maximum power. Two measurements (1 and 2) were done in semi-sunny conditions, and two measurements (3 and 4) were done in direct sunlight.

The shortest possible exposure time according to the camera specification is 0.038 ms, slightly depending on other camera settings. For each measurement 152 images were captured, with increasing exposure time from 0.04 to 2.0 ms. A delay of 1 second was set between each image.

L. Light Intensity Levels

To analyze the effect of different signal to noise ratios, the flashlight intensity, and camera gain settings were adjusted to make eight different exposure cases. Since the camera had fixed levels for the master and the analogue gain, the flashlight energy levels were adjusted from these gain levels to achieve similar image gray scale levels for all cases. The duration time of flashes, and the driving currents of the LED, were altered until the maximum gray level of any pixel was high but well below the saturation point; approximately 90 percent of the maximum in 12-bit mode. The gain levels could be adjusted by changing either "analogue gain" between -10 and 4 or "master gain" to 100, 200, 300 or 400. The eight cases are labeled G-10MG100, G-5MG100, G0MG100, G2MG100, G4MG100, G4MG200, G4MG300 and G4MG400.

The light energy at each exposure level was investigated using a thermal power sensor (Thorlabs S302C) and a pulsed signal, 3-10 μs , 9-36 kHz. To reduce the thermal effect of the heated glass and the ambient light, the power was measured immediately before and after start and stop. The pulse length was measured using a semiconductor light sensor connected to an oscilloscope. The result is shown in Fig. 9.

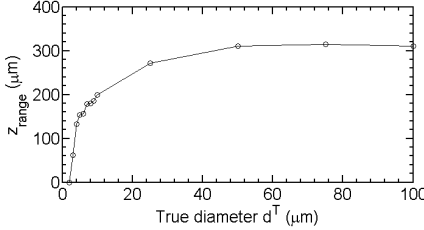


Fig. 6. Results of measuring range z_{range} depending on true diameter using Laplacian of Gaussian 13×13 and threshold of 0.002 applied on dots of 2, 3, 4, 5, 6, 7, 8, 9, 10, 25, 50, 75 and $100 \mu\text{m}$ diameter in one exposure case.

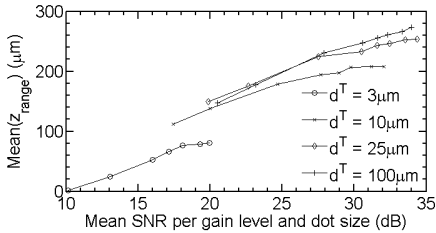


Fig. 7. Results of measuring range z_{range} depending on mean snr_j using Laplacian of Gaussian 13×13 and threshold of 0.002 applied on dots of 3, 10, 25 and $100 \mu\text{m}$ diameter with eight different exposure cases. Every marker is the mean z_{range} of 100 series of images.

III. RESULTS

A. Estimating Measuring Range

The measuring range z_{range} was first determined for one exposure case, G0MG100, by measuring the dots of all available sizes in the range covered by the optical focus. It is determined by the number of detected dots times the step length between each measurement. The result of this measurement is presented in Fig. 6.

Fig. 7 shows the mean measuring range $mean(z_{range})$ depending on snr_j for multiple measurements of the dots with true diameters, $d^T = 3, 10, 25$ and $100 \mu\text{m}$. For each of the eight exposure cases, the dots were measured 100 times in range steps of two micrometers, resulting in 80,000 images for the $3 \mu\text{m}$ dot, and 160,000 images each for the other three sizes. Images creating a closed contour from the Laplacian of Gaussian edge detection, threshold 0.002 are counted. As each step was two micrometers, the measuring range (in micrometers) is the number of detected dots within the range times two.

Fig. 8 shows the measuring range coefficient of variation $CV(z_{range})$ for the 100 measuring ranges, rng , calculated for each SNR case.

$$CV(z_{range})(snr) = \frac{\sum_{rng=1}^{100} (z_{range} - mean(z_{range}))^2}{mean(z_{range})} \quad (10)$$

The coefficient of variation is the ratio of the standard deviation to the mean. The standard deviation decreases with increasing SNR.

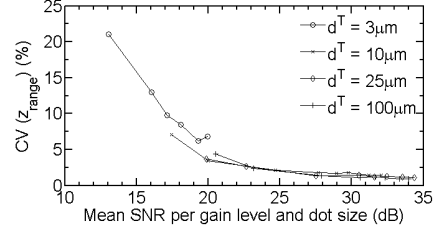


Fig. 8. Coefficient of variation for the mean measuring range.

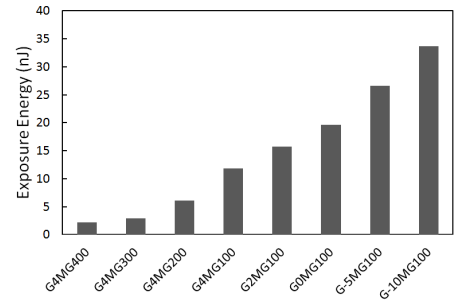


Fig. 9. Light energy (nJ) for exposure in each of the eight gain levels used. The energy was tuned manually up to a level of high exposure, but not saturating any point in the image.

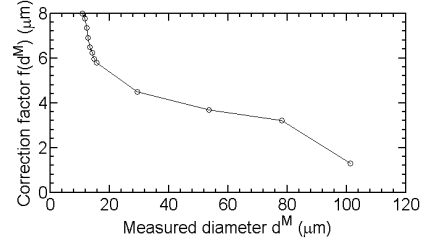


Fig. 10. Difference between measured and actual diameter, $f(d^M)$, using the Laplacian of Gaussian 13×13 with threshold 0.002 to define the measured area by edge detection.

B. Estimating True Diameter

The difference between the measured and the true diameter from the micrometer scale was used to create the lookup table for size calibration. Fig. 10 illustrates the correction factor $f(d^M)$ using the Laplacian of Gaussian 13×13 with threshold 0.002 to define the measured area by edge detection.

Fig. 11 shows the coefficient of variation $CV(d^M)$ for the measured diameter d^M when measured on the 3, 10, 25 and $100 \mu\text{m}$ dots in eight different exposure cases. For the three micrometer dot, the two lowest exposure levels did not result in a measurement. The other decreased from 0.72 percent (G4MG200, SNR 13dB) to 0.22 percent (G-10MG100, SNR 20dB). The variation coefficient of the

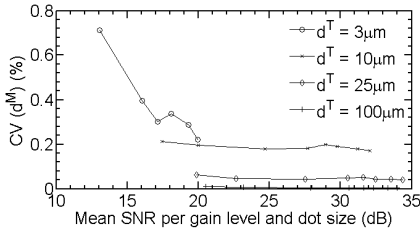


Fig. 11. Coefficient of variation from 100 series of measured diameters d^M for the 3, 10, 25 and 100 μm dots.

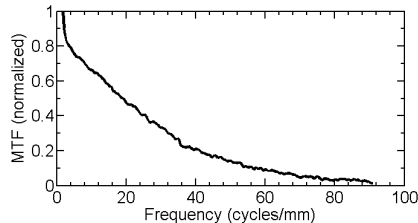


Fig. 12. MTF curve of the system measured at optimal focus by using FFT analysis of the gradient of the step response for a sharp edge in the center of the field of view. Frequency is given in sinus cycles per mm and the contrast is normalized between the darkest and lightest parts of the image.

ten micrometer dot decreased from 0.22 to 0.17 percent. The variation coefficient of the 25 μm dot varied between 0.063 and 0.044 percent and for the 100 μm dot it varied between 0.0085 and 0.0032 percent.

C. Energy Required for Exposure

The illumination energy required to get a good exposure for each of the eight gain setting levels is shown in Fig. 9. 34 nJ is required for the area in view (7.8 mm^2) for the lowest gain setting, which results in the highest SNR. The area in view is about 8 times smaller than the illuminated area of the collimated LED, which was measured to about $8 \times 8 \text{ mm}$.

D. Measuring the Optical Transfer Function

The MTF curve was measured using FFT (Fast Fourier Transform) analysis in Matlab on the gradient (impulse response) of images of a straight edge on the micrometer scale. The micrometer scale was moved in steps of five micrometers in z-direction, creating one MTF curve for every step. The result from one position (at optimal focus) is shown in Fig. 12, and the resolution limit at 30 percent contrast depending on the distance from optimal focus is shown in Fig. 14.

IV. DISCUSSION AND ANALYSIS

A. The Optical System Limitations

The optical resolution of the system is limited by the wavelength of the illuminating light, the lens resolution and the spatial resolution of the sensor.

The number of detected droplets per image depends on the density of the droplet distribution, and a less dense fog will

require a larger ensemble of images to measure equally many droplets. Therefore we sought a camera with not only high sensitivity and high signal to noise ratio, but also high imaging rate and transfer speed. Global shutter is essential since the droplets in reality are moving and the exposure only occurs during the short illuminating flash. The frame rate is limited by the achievable transfer rate from the camera to the analyzing computer and the analyzing time for every image.

The 5.5 μm pixels of the CMV4000 sensor are equipped with micro lenses, raising the efficiency from 42 percent (fill factor without micro lens) to 60 percent (quantum efficiency times fill factor at 550 nm) according to the manufacturer's data sheet. The micro lenses would also mean a smaller risk for digital aliasing. Spatial resolution of a digital image system can be given in the unit of line pairs per mm (lp/mm). A 5.5 μm pixel pitch means that the finest resolvable frequency at the focal plane according to Nyquist-Shannon sampling theorem is $1/(2 \cdot 0.0055) = 91$ line pairs/mm (lp/mm).

A telecentric lens simplifies measuring as the magnification is constant with varying distance to the object. The TC4M004-C has a magnification of $4 \times$ and a working f/# of 22. A similar lens with lower magnification but with the same working f/# would increase the depth of field, thus creating a larger measuring volume. Since the depth of field is approximately inversely proportional to the square of the magnification, a similar lens with $2 \times$ magnification would give a $16 \times$ larger measuring volume for every image, albeit on the cost of resolution.

Rayleigh's criterion can be used as an estimation of the smallest resolvable distance in the object plane, Δl .

$$\Delta l \approx 1.22 \lambda \frac{1}{1 + |m|} wF/\# \quad (11)$$

With $wF/\# = 22$, $\lambda = 455 \text{ nm}$, and $m = 4$ we get $\Delta l = 2.44 \mu\text{m}$. In the focal plane, with $4 \times$ magnification, this would correspond to a theoretical maximum diffraction limited resolution of $(1/0.00244)/4 = 102$ lp/mm. Due to imperfections in the lens design and manufacturing, the usable resolution is less, especially closer to the sensor edges. Compare with the system MTF measured at optimal focus shown in Fig. 12. This curve indicates a resolution of only about 58 lp/mm at 10 percent contrast.

Using a high power LED instead of laser reduces the interference effects used in e.g. holography [28], but since it is a monochromatic source, interference may not be completely ruled out. The coherence length, provided a Gaussian spectrum, can be approximated by Eq. 12 [39]:

$$l_c \approx \sqrt{\frac{2 \ln 2}{\pi}} \frac{\lambda_0^2}{\Delta \lambda} \quad (12)$$

$\Delta \lambda$ is the -3 dB spectral bandwidth and was measured to 20nm for the blue LED used in this study. The actual peak was measured to 453nm. Applying this in Eq. 12 we estimate the coherence length to about 6.8 μm .

LEDs can sometimes be used with currents far above the specifications, as long as the pulse length is short and the duty cycle is low enough to permit the heat generated to be transported away between the pulses. Using the LED above

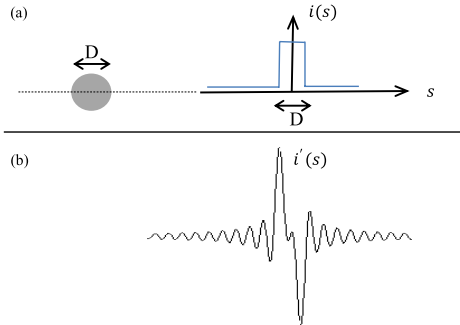


Fig. 13. (a) Shows a simplification of an imaged particle with diameter D as a square pulse in one dimension. (b) Shows the first derivate $i'(s)$ achieved by assuming the lens works as a low pass filter in the frequency domain.

specifications may though affect the efficiency and aging of the LED. LED emittance also depends on the temperature. Depending on the capacitance of the diode, the rise time may limit the current, although there exist some techniques to shorten the LED pulses [40], [41].

B. Laplacian and Boundary Fill as Selection Criteria

In this study we use the Laplacian of Gaussian for edge detection and noise filter. In brief comparison with other edge detection algorithms, like Canny [42], it gives the best result. This is not to say there is no room for optimization. We define the edge where the second derivate of the between zero and one normalized image is above 0.002. Lowering the threshold to 0.001 gives too much response from noise and raising the threshold reduces the measuring range.

The 13×13 size convolution kernel is a digital approximation of the true Laplacian of Gaussian function. Increasing the size of the kernel would mean more calculations for each processed image, and a smaller usable field of view, but could also lower the noise sensitivity.

Subtracting the edge detected binary image from the same image with binary fill applied, sorts out the boundaries that have closed contours. As this works as selection criteria for which droplets to count and which not to count, it will also define the measuring range. The precision of the measuring range is estimated by taking series of images of the same dot, and moving the dot a distance Δz between each image in every series. In each of the image series, we use the standard deviation as a measure of the precision. This was done for 100 series of images of the 3, 10, 25 and 100 μm dots.

As was shown in Section II., the Laplacian is a second order derivate. This means that a particle can be segmented as long as the edge of an imaged droplet has strong enough gradient, as shown in Fig. 2. To explain this we can imagine an imaged particle of size D where the intensity profile in one dimension s is graphed as $i(s)$. See Fig. 13 (a). This is an ideal optical system having infinite resolution. The Fourier transform F of $i(s)$ becomes $I(\omega) = F[i(s)] = \frac{2}{\omega} \sin \frac{\omega D}{2}$ where ω is the angular frequency. The strength of the first order

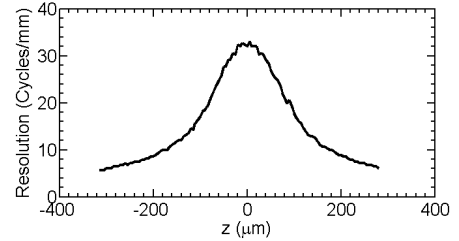


Fig. 14. Resolution limit at 30% contrast measured by FFT on an edge at different distances from the optimum focus.

gradient $\frac{di(s)}{ds} = i'(s)$ is assumed to give information about how sharp the droplet is imaged. The frequency transform of $i'(s)$ is $I'(\omega) = j\omega \cdot I(\omega)$. We now limit the resolution of the optical system to ω_g . This limit allows computation of the first order gradient as the reverse Fourier transform $i'(s) = F^{-1}\{I'(\omega)\}$ for $-\omega_g < \omega < \omega_g$. In this simplified analysis we are assuming that the lens system behaves as an ideal low pass filter having a limited angular frequency of ω_g . We can estimate $\omega_g \approx \frac{2\pi}{r}$ where r is the lens resolution in the focal plane by Rayleigh's criterion. The gradient can now be computed as:

$$i'(s) = \frac{\sin(\omega_g(s + \frac{D}{2}))}{\pi(s + \frac{D}{2})} - \frac{\sin(\omega_g(s - \frac{D}{2}))}{\pi(s - \frac{D}{2})} \quad (13)$$

An example graph of $i'(s)$ is shown in Fig. 13 (b). From this graph and Eq. 13 can be seen that maximum gradient strength G_{max} appears at $s = \pm \frac{D}{2}$ as long as D is large enough.

$$G_{max} = i'(s) = \lim_{s \rightarrow \pm \frac{D}{2}} i'(s) = \pm \frac{\omega_g}{\pi} \quad (14)$$

Small droplet sizes D with respect to optical resolution r will cause the two gradient peaks shown in Fig. 13 (b) to interfere. The maximum gradient strength G_{max} is proportional to the optical system resolution expressed as lp/mm. We can also conclude from analyzing the MTF curve obtained empirically that larger distance from the optimal focus will result in lower resolution. Fig. 14 shows the resolution depending on the distance from the optimal focus, when the measured MTF is 30 percent. If we achieve a measuring range of 0.2 mm empirically by edge detecting our test objects, according to Fig. 14, we need a resolution of at least about 17-18 cycles/mm to measure a particle. This also explains why we can use a gradient operator in combination with a threshold on gradient strength for the control of the measuring range.

C. Comparing Drops With Dots

In the study described in this paper we have assumed that a spherical object such as a water droplet in air will produce the same shadow image as a disc shaped dot printed on a sheet silicon glass.

The reason for making this assumption is first that despite the transparency, the refractive index of water makes the

droplet work as a spherical lens that will scatter almost all of the light that reaches the droplet from different directions.

Some of the light will also be absorbed, albeit the absorption of a single water droplet is negligible due to its small volume and because water absorb very little in the visible spectrum. The combined effect of scattering and absorption is the extinction [29]. By using a telecentric lens for imaging, the amount of scattered light that will reach the camera is very small compared with the background illumination. This makes the droplet, despite being almost transparent, to appear as a black disc against the bright background.

Irregularities and dirt on the surface of the glass sheet will add uncertainty to the measurement of the reference object. The smallest dot measured, two micrometer in diameter, was even difficult to find as some disturbances close to it were equal in size or larger.

For larger droplets the light passing straight through the center of the drop is visible, and a function may be needed to handle this.

D. Measuring Droplets

A real distribution of water droplets was created by an ultrasonic fog generator. As they were not contained in a closed environment the droplets evaporated quickly after exiting the generator tube, making the true sizes difficult to verify. But from the calibration tables shown in Fig. 7 and Fig. 10 we can estimate the MVD and LWC for one sample image.

As mentioned previously, there may be cases where two droplets are close enough to appear as one much larger drop. A solution that was tried was to make a measurement of the droplet's circularity and add this as selection criteria. This solution may also work as a filter for ice or snow particles. Unfortunately this also reduces the measured number of particles, resulting in an underestimation of LWC. To deal with this there are at least a few alternatives, e.g. improving the circularity measurement [37].

Droplets that are very close are likely to coalesce, thereby decreasing the number concentration at a rate that appears to increase for larger droplets and more complex droplet size distributions [43]. Therefore we expect the likelihood of finding two droplets close to each other in a natural distribution to be low. A realistic fog with $LWC = 0.4 \text{ g/m}^3$ and droplet size five μm has the number concentration $6 \cdot 10^9 \text{ m}^{-3}$. With this concentration, only nine droplets, on average, are expected in a sample volume corresponding to one image with our system.

The accuracy and precision will depend on the number of droplets sampled. This means that for a population of droplets with large diameters, many more images are needed to get the same accuracy, than for a population of droplets with small diameters, given the populations have the same LWC.

E. Particle Size

The particle size is determined by the area bounded by the edge detection algorithm illustrated by the filled white blob in Fig. 2 (lower left). If a threshold is set relative to the background level that has a value below a given threshold

limit, the measured area could be determined by the darkness of the object's shadow. This alternative could improve the accuracy of size for small droplets.

The size accuracy in general is limited by the resolution of the optical system and the effect of the diffracted light on the edge detection. In Fig. 11 one can see that the coefficient of variation for a $100 \mu\text{m}$ dot is very low and that it increases with decreasing diameter. This effect is likely caused by the diffraction patterns. Although the optical resolution is too low to distinguish the diffraction patterns, it adds an uncertainty to the size measurement of small droplets.

The calibration is based on the mean measured size of any particle in the measuring range. Therefore the coefficient of variation in Fig. 11 is based on the measured diameter of all detected z-positions within the measuring range.

F. Measuring Volume

As can be seen in Fig. 7 and Fig. 8, the SNR is more important for small droplets. A high SNR gives a lower coefficient of variation for the measurement range and thus a more precise measurement of the LWC according to (11). It also means that the higher SNR we can achieve, the smaller the droplets we can find in the measuring range.

One should consider that the measurement volume is very small compared with the population of water particles in e.g. a cloud or a fog, and that the distribution of water may vary a lot in the physical surroundings. To get a good average value of the MVD and LWC, the number of counted particles needs to be large.

Sometimes the concentration of particles varies a lot within the same cloud or fog. Whether it is the average over a certain time, or the momentous maximum of LWC/MVD that is the most important to measure with regards to icing, future studies may reveal.

G. LWC Precision

We estimate the precision (coefficient of variation) of a measured value of the LWC based on two of the dots of known size (10 and $25 \mu\text{m}$) of the micrometer scale. Here we assume that all the imagined measured droplets are of equal shape and have only one size and that the distribution is even. I.e. all m_j and V_j are equal for any j so we skip the index j for m and V .

From this assumption and equation (7):

$$LWC = n \frac{m}{V} \quad (15)$$

$$|\Delta LWC| \leq n \left| \Delta \frac{m}{V} \right| \quad (16)$$

Assuming that the relative errors of m and V are small and using the triangle inequality we get:

$$\left| \frac{\Delta LWC}{LWC} \right| \lesssim \left| \frac{\Delta m}{m} \right| + \left| \frac{\Delta V}{V} \right| \quad (17)$$

By calculating the mass of water using a density ρ of 1g/cm^3 we get the mass from the true diameter d^T :

$$m_i = \rho V_i = \frac{4\pi (d^T/2)^3}{3} = \frac{\pi}{6} (d^T)^3 \quad (18)$$

After logarithmic derivation we get:

$$\left| \frac{\Delta m}{m} \right| = 3 \left| \frac{\Delta d^T}{d^T} \right| \quad (19)$$

From Fig. 8 and Fig. 10 we read an approximate value of the variation coefficient for the case with 25 μm droplets and SNR level >27 dB:

$$\left| \frac{\Delta V}{V} \right|_{25\mu\text{m}} < 1.4\% \quad (20)$$

$$\left| \frac{\Delta d^T}{d^T} \right|_{25\mu\text{m}} < 0.05\% \quad (21)$$

$$\left| \frac{\Delta LWC}{LWC} \right|_{25\mu\text{m}} \lesssim 1.4\% + 3 \times 0.05\% = 1.6\% \quad (22)$$

The same calculation for 10 μm droplets, again at an exposure case with SNR >27dB, gives a larger statistical error:

$$\left| \frac{\Delta V}{V} \right|_{10\mu\text{m}} < 1.8\% \quad (23)$$

$$\left| \frac{\Delta d^T}{d^T} \right|_{10\mu\text{m}} < 0.2\% \quad (24)$$

$$\left| \frac{\Delta LWC}{LWC} \right|_{10\mu\text{m}} \lesssim 1.8\% + 3 \times 0.2\% = 2.4\% \quad (25)$$

The larger the statistical mass, i.e. the number of droplets measured, the closer the measured variations should be to the calculated variations. These calculations may not reveal the effect of digital aliasing, which would be higher for smaller droplets.

H. Illumination Power Required at High Wind Speed

Since the instrument is intended to image droplets moving with the air, a shorter and stronger illumination pulse than the one in the laboratory is required. From the results we see that we get the highest SNR at the highest energy, 34 nJ. To get a good image of a droplet only a few micrometers in diameter, it should move as little as possible during the exposure. As the risk of icing increases with increasing wind speed [44], it is important that the droplets are correctly measured also at higher wind speeds. Assuming that the highest possible wind speed is 50 m/s and the droplet can move at most one micrometer for a correct measurement, the exposure time should be no more than 20 ns. In this case, to get the highest SNR we need an average illumination power on the total area of view of 1.7 W. But this power may be difficult to achieve with an LED.

The highest emitted power tested with the 455nm Mightex LED was 348 mW at 2.5 Ampere driving current. As the collimated beam is about ten times ten millimeters, and the field of view is only three times three, only about one ninth of the emitted power is used for the exposure. This makes the system less sensitive to misalignment, but also quite inefficient. Since the area in view is nine times smaller than the collimated light beam this would mean 39 mW in the view area, which is about 44 times lower than the required, 1.7 W power for example above. But to make the light beam size smaller one

would either have to use a lens of shorter focal length, which would lower the degree of collimation, or use a different light source with a smaller emissive area, which may not be possible with the required power. This is clearly a limitation of the LED when used to produce collimated light.

If we can use a lower SNR and still get useful images we would need less energy. If we e.g. set a higher camera gain (G4MG200 would require only 6 nJ of light energy), and if the wind speed can be reduced to 10 m/s, only 60 mW illumination power is required. In this case it should be possible to use the same LED to study droplets in a realistic environment.

Unfortunately, reducing the wind speed artificially by adding aerodynamic brakes will affect the air flow and this can change the properties of the measured particles [16]. It will also likely be more difficult to keep the instrument itself free from ice during the measuring.

I. Choice of Camera, Lens and Illumination

The camera is a c-mount CMOS camera with 2048×2048 resolution. The pixel size is 5.5 μm . Due to the strong commercial interest in this field, we expect this type of camera or similar to be available in large volumes and at even lower prices in the future. There are cameras with higher resolutions, but a higher resolution would not necessarily give better result since the lens resolution needs to match, and this would mean a higher system price. Smaller pixel sizes would also mean lower SNR, mainly due to the lower fill factor of the sensor. Lower SNR would then give a smaller measuring volume, following the results in Fig. 7 and Fig. 8.

The lens was chosen to fit the camera size and resolution. A lower magnification would increase the measuring volume, but raise the limit of the smallest particles possible to detect. A higher magnification puts higher requirements on the optics, resulting in a higher material cost.

Initially, two LED with different peak wavelengths (455 nm and 850 nm) were tested, but since both the signal to noise ratio (SNR) and sharpness seemed better for the shorter wavelength, the 455 nm LED was used throughout the study. An 11 mm collimating lens was also tried. This lens is able to concentrate the beam more, but since the focusing distance becomes much shorter, which might cause a problem for the flow of particles, and the beam divergence is doubled, we chose only to use the 22 mm lens in the study.

J. Ambient Light

The background radiation was measured by imaging the generated fog in ambient daylight (22,000 lux) and (for a worst case scenario) in direct sunlight (80,000 lux). The result shows that unless the camera is pointed directly at the sun, an exposure time less than 0.2 ms will give no significant effect in daylight.

V. CONCLUSIONS

LWC and MVD can be derived from digital images of the droplets by using a shadowgraph imaging system with a collimated LED and a telecentric lens.

By comparing with dots of known sizes printed on a glass plate, we predict the LWC coefficient of variation to be less

than 1.6 percent for droplets 25 μm in diameter, and less than 2.4 percent for droplets 10 μm in diameter. This error increases with decreasing droplet diameter.

A comparative study of the system with a reference instrument on a larger homogenous aerosol will show if the accuracy is good enough to predict icing.

REFERENCES

- [1] N. Dalili, A. Edrisy, and R. Carriveau, "A review of surface engineering issues critical to wind turbine performance," *Renew. Sustain. Energy Rev.*, vol. 13, pp. 428–438, Feb. 2009.
- [2] S. Fikke *et al.*, "COST 727: Atmospheric icing on structures," *Meas. Data collection Icing, State Art, Publication MeteoSwiss*, vol. 75, no. 110, pp. 1381–1422, 2006.
- [3] M. C. Homola, M. S. Virk, P. J. Nicklasson, and P. A. Sundsbø, "Performance losses due to ice accretion for a 5 MW wind turbine," *Wind Energy*, vol. 15, no. 3, pp. 379–389, 2012.
- [4] W. J. Jasinski, S. C. Noe, M. S. Selig, and M. B. Bragg, "Wind turbine performance under icing conditions," *J. Solar Energy Eng.*, vol. 120, no. 1, pp. 60–65, 1998.
- [5] L. Makkonen, T. Laakso, M. Marjaniemi, and K. Finstad, "Modelling and prevention of ice accretion on wind turbines," *Wind Eng.*, vol. 25, no. 1, pp. 3–21, 2001.
- [6] J. Shin and T. H. Bond, "Results of an icing test on a NACA 0012 airfoil in the NASA Lewis icing research tunnel," Lewis Research Center, Cleveland, OH, USA, NASA Tech. Memo. 105374, AIAA-92-0647, prepared for the 30th Aerosp. Sci. Meeting Exhibit sponsored by the Amer. Inst. Aeronaut. Astronaut., Reno, NV, USA, Jan. 6–9, 1992.
- [7] G. Thompson, B. E. Nygaard, L. Makkonen, and S. Dierer, "Using the weather research and forecasting (WRF) model to predict ground/structural icing," in *Proc. 13th Int. Workshop Atmos. Icing Struct. METEOTEST*, Andermatt, Switzerland, 2009, pp. 1–8.
- [8] B. E. K. Nygaard, J. E. Kristjánsson, and L. Makkonen, "Prediction of in-cloud icing conditions at ground level using the WRF model," *J. Appl. Meteorol. Climatol.*, vol. 50, pp. 2445–2459, Dec. 2011.
- [9] O. Parent and A. Ilina, "Anti-icing and de-icing techniques for wind turbines: Critical review," *Cold Regions Sci. Technol.*, vol. 65, no. 1, pp. 88–96, 2011.
- [10] L. Makkonen, "Analysis of rotating multicylinder data in measuring cloud-droplet size and liquid water content," *J. Atmos. Ocean. Technol.*, vol. 9, pp. 258–263, Jun. 1992.
- [11] W. R. Sand, W. A. Cooper, M. K. Politovich, and D. L. Veal, "Icing conditions encountered by a research aircraft," *J. Climate Appl. Meteorol.*, vol. 23, pp. 1427–1440, 1984.
- [12] S. G. Cober, G. A. Isaac, and J. W. Strapp, "Characterizations of aircraft icing environments that include supercooled large drops," *J. Appl. Meteorol.*, vol. 40, pp. 1984–2002, 2001.
- [13] M. C. Homola, M. S. Virk, T. Wallenius, P. J. Nicklasson, and P. A. Sundsbø, "Effect of atmospheric temperature and droplet size variation on ice accretion of wind turbine blades," *J. Wind Eng. Ind. Aerodyn.*, vol. 98, no. 12, pp. 724–729, 2010.
- [14] R. F. Ide, *Comparison of Liquid Water Content Measurement Techniques in an Icing Wind Tunnel*, document NASA/TM-1999-209643, ARL-TR-2134, U.S. Army Res. Lab., Glenn Res. Center, Cleveland, OH, USA, 1999.
- [15] D. Baumgardner, "An analysis and comparison of five water droplet measuring instruments," *J. Climate Appl. Meteorol.*, vol. 22, pp. 891–910, May 1983.
- [16] D. Baumgardner *et al.*, "Airborne instruments to measure atmospheric aerosol particles, clouds and radiation: A cook's tour of mature and emerging technology," *Atmos. Res.*, vol. 102, pp. 10–29, Oct. 2011.
- [17] P. Kulkarni, P. A. Baron, and K. Willeke, Eds., *Aerosol Measurement: Principles, Techniques, and Applications*. New York, NY, USA: Wiley, 2011.
- [18] M. C. Homola, P. J. Nicklasson, and P. A. Sundsbø, "Ice sensors for wind turbines," *Cold Regions Sci. Technol.*, vol. 46, no. 2, pp. 125–131, 2006.
- [19] J. K. Spiegel, P. Zieger, N. Bukowiecki, E. Hammer, E. Weingartner, and W. Eitinger, "Evaluating the capabilities and uncertainties of droplet measurements for the fog droplet spectrometer (FM-100)," *Atmos. Meas. Technol.*, vol. 5, no. 9, pp. 2237–2260, 2012.
- [20] R. D. Cohen, "Shattering of a liquid drop due to impact," in *Proc. Math. Phys. Sci.*, vol. 435, no. 1895, pp. 483–503, 1991.
- [21] A. V. Korolev, S. V. Kuznetsov, Y. E. Makarov, and V. S. Novikov, "Evaluation of measurements of particle size and sample area from optical array probes," *J. Atmos. Ocean. Technol.*, vol. 8, pp. 514–522, Aug. 1991.
- [22] M. Wendisch and J.-L. Brenguier, Eds., *Airborne Measurements for Environmental Research: Methods and Instruments*. Weinheim, Germany: Wiley, 2013.
- [23] R. G. Knollenberg, "The optical array: An alternative to scattering or extinction for airborne particle size determination," *J. Appl. Meteorol.*, vol. 9, pp. 86–103, Feb. 1970.
- [24] J. E. Dye and D. Baumgardner, "Evaluation of the forward scattering spectrometer probe. Part I: Electronic and optical studies," *J. Atmos. Ocean. Technol.*, vol. 1, pp. 329–344, Dec. 1984.
- [25] G. Mie, "Beiträge zur Optik trüber Medien, speziell kolloidalen Metalloxösungen," *Ann. Phys.*, vol. 330, no. 3, pp. 377–445, 1908.
- [26] D. Baumgardner, H. Jonsson, W. Dawson, D. O'Connor, and R. Newton, "The cloud, aerosol and precipitation spectrometer: A new instrument for cloud investigations," *Atmos. Res.*, vols. 59–60, pp. 251–264, Oct./Dec. 2001.
- [27] R. P. Lawson and R. H. Cormack, "Theoretical design and preliminary tests of two new particle spectrometers for cloud microphysics research," *Atmos. Res.*, vol. 35, pp. 315–348, Jan. 1995.
- [28] J. Henneberger, J. P. Fugel, O. Stetzer, and U. Lohmann, "HOLIMO II: A digital holographic instrument for ground-based *in-situ* observations of microphysical properties of mixed-phase clouds," *Atmos. Meas. Technol.*, vol. 6, no. 3, pp. 4183–4221, 2013.
- [29] C. F. Bohren and D. R. Huffman, *Absorption and Scattering of Light by Small Particles*. New York, NY, USA: Wiley, 2008.
- [30] A. D. Ward, M. Zhang, and O. Hunt, "Broadband Mie scattering from optically levitated aerosol droplets using a white LED," *Opt. Exp.*, vol. 16, no. 21, pp. 16390–16403, 2008.
- [31] J. Estevadeordal and L. Goss, "PIV with LED: Particle shadow velocimetry (PSV)," in *Proc. 43rd AIAA Aerosp. Sciences Meeting Exhibit.*, 2005, pp. 12355–12364.
- [32] C. Willert, B. Stasicki, J. Klinner, and S. Moessner, "Pulsed operation of high-power light emitting diodes for imaging flow velocimetry," *Meas. Sci. Technol.*, vol. 21, no. 7, p. 075402, 2010.
- [33] R. J. H. Klein-Douwel, P. J. M. Frijters, L. M. T. Somers, W. A. de Boer, and R. S. G. Baert, "Macroscopic diesel fuel spray shadowgraphy using high speed digital imaging in a high pressure cell," *Fuel*, vol. 86, nos. 12–13, pp. 1994–2007, 2007.
- [34] P. J. Connolly, M. J. Flynn, Z. Ulanowski, T. W. Choularton, M. W. Gallagher, and K. N. Bower, "Calibration of the cloud particle imager probes using calibration beads and ice crystal analogs: The depth of field," *J. Atmos. Ocean. Technol.*, vol. 24, pp. 1860–1879, Nov. 2007.
- [35] D. Marr and E. Hildreth, "Theory of edge detection," *Proc. Roy. Soc. London. B. Biol. Sci.*, vol. 207, pp. 187–217, Feb. 1980.
- [36] R. C. Gonzalez and R. E. Woods, *Digital Image Processing*, 2nd ed. Englewood Cliffs, NJ, USA: Prentice-Hall, 2002.
- [37] R. S. Montero and E. Bribiesca, "State of the art of compactness and circularity measures," *Int. Math. Forum*, vol. 4, no. 27, pp. 1305–1335, 2009.
- [38] K. J. Finstad, E. P. Lozowski, and L. Makkonen, "On the median volume diameter approximation for droplet collision efficiency," *J. Atmos. Sci.*, vol. 45, pp. 4008–4012, Dec. 1988.
- [39] C. Akcay, P. Parrein, and J. P. Rolland, "Estimation of longitudinal resolution in optical coherence imaging," *Appl. Opt.*, vol. 41, no. 25, pp. 5256–5262, 2002.
- [40] O. Veledar, P. O. Byrne, S. Danaher, J. I. Allen, L. F. Thompson, and J. E. McMillan, "Simple techniques for generating nanosecond blue light pulses from light emitting diodes," *Meas. Sci. Technol.*, vol. 18, no. 1, p. 131, 2007.
- [41] H. Tanaka, Y. Umeda, and O. Takyu, "High-speed LED driver for visible light communications with drawing-out of remaining carrier," in *Proc. IEEE Radio Wireless Symp. (RWS)*, Jan. 2011, pp. 295–298.
- [42] J. Cannby, "A computational approach to edge detection," *IEEE Trans. Pattern Anal. Mach. Intell.*, vol. 8, no. 6, pp. 679–698, Nov. 1986.
- [43] R. Bordás, T. Hagemeier, B. Wunderlich, and D. Thévenin, "Droplet collisions and interaction with the turbulent flow within a two-phase wind tunnel," *Phys. Fluids*, vol. 23, no. 8, p. 085105, 2011.
- [44] L. Makkonen, "Models for the growth of rime, glaze, icicles and wet snow on structures," *Philos. Trans. Roy. Soc. London A. Math. Phys. Sci.*, vol. 358, no. 1776, pp. 2913–2939, 2000.



Staffan Rydbom received the M.S. degree in applied physics and electrical engineering from Linköping University, Sweden, in 2001. He is currently pursuing the Ph.D. degree with Mid Sweden University. From 2002 to 2009, he was with Bombardier Transportation, involved in the design of train control systems and engineering bid management. He did engineering project management at Permotrol from 2009 to 2011, and was with ABB Service from 2012 to 2013.

His research interests include measuring techniques for atmospheric icing on structures and real-time image processing.



Benny Thörnberg received the degree in electronics design, the B.Sc. degree in electrical engineering, and the Licentiate(Tech.) and Ph.D. degrees from Mid Sweden University, Sundsvall, Sweden, in 1988, 2001, 2004, and 2006, respectively. He was with Regam Medical Systems AB, Sundsvall, from 1990 to 1997, where he was involved in a camera design for intraoral X-ray imaging. He is currently an Assistant Professor with the Department of Electronics Design, Mid Sweden University. His current research interests include machine vision, metrology, design methods for embedded systems and, in particular, real-time video processing and analysis.

Paper II

Droplet Imaging Instrument - Metrology Instrument for Icing Condition Detection

S. Rydblom, B. Thörnberg

Droplet Imaging Instrument

Metrology Instrument for Icing Condition Detection

Staffan Rydholm

Mid Sweden University
Sundsvall, Sweden

Benny Thörnberg

Mid Sweden University
Sundsvall, Sweden

Abstract—An instrument for measuring water droplets is described and constructed. It is designed to measure the volume concentration and the size distribution of droplets in order to detect icing conditions in a natural fog. The instrument works by shadowgraph imaging, with a collimated blue LED as background illumination. We show how to use a reference object to obtain a calibration of the droplet size and the measurement volume. These properties are derived from a measurement of the object's shadow intensity and its edge second derivative. From the size of every measured droplet and its expected detection volume, a measure of the liquid water content (LWC) and the median volume diameter (MVD) can be estimated. The instrument can be used for continuous measurement in a remote weather-exposed location and is tested in a small environment chamber. We also describe this chamber and how we can change the LWC using an ultrasonic fog generator and a fan.

Keywords—*machine vision; image analysis; atmospheric measurements; liquid water content; fog chamber*

I. INTRODUCTION

Measuring and controlling the properties of a fog of water droplets has been the interest and focus of many studies during at least half a century. Applications range from atmospheric studies, aircraft safety to military and commercial applications. Recent developments of fog climate chambers, like e.g. the new fog chamber at Sandia National Laboratories (2015) shows that the interest has not decreased.

A method to measure droplets in order to detect icing has been suggested [1]. The method use shadowgraph imaging and image analysis to determine the size and the measuring volume of each individual droplet. Based on this technique, we construct an instrument suited for remote reading and measurement at a weather exposed location. In this document we describe the instrument and its major limitations.

Using the new instrument, we also show that we can control the liquid water content in the fog chamber by using an ultrasonic fog generator and a speed controlled fan.

A. Measurement Object

Icing is mostly caused by cloud droplets measuring between 10 μm and 30 μm in diameter [2-4]. Meta studies of droplet distributions in low altitude clouds [5, 6] show that the liquid water content (LWC) is highly variable, even during the same measurement. Icing may start with LWC as low as 0.1 g m^{-3} but will be more severe the higher the LWC.

Since the LWC is proportional to the diameter with a power to three, the number concentration of droplets will vary significantly depending on the size of the droplets. A monosized ensemble of 10 μm droplets would e.g. contain 1000 as many droplets per volume unit air as one of 100 μm droplets at the same LWC. It means that the speed with which we can measure a certain volume of air is an important design factor. This is a limiting, but improvable factor for the constructed instrument that will be discussed.

B. Working Principle

We use a shadowgraph system consisting of a monochrome digital image sensor with a telecentric lens and a collimated LED illumination. See Fig. 1. Droplets are identified from the image background using edge detection to form a closed boundary around each droplet. The size of each droplet is measured using the size of the closed boundary adjusted by a weighted average of the pixel intensities within it.

C. Calibration

Calibration of both size and measuring volume is done using a number of fixed size silicon dots printed on a glass. The measured dot size is converted to a calibration function depending on measured size and the edge's sharpness. The measurement volume is estimated by measuring the range where the edge detection results in a closed curve, resulting in a detected object, while the area field of view can be considered as constant.

II. MATERIALS AND METHODS

The system consists of three main physical modules; the camera, the processing computer and the illumination. The camera and the illumination are mounted at a fixed distance and position, allowing air to pass between the lenses.

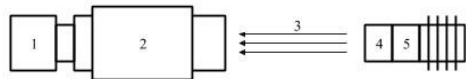


Fig. 1. The shadowgraph principle: 1) Camera, 2) Lens 3) Light beam, 4) Collimating lens, 5) LED including heat sink.

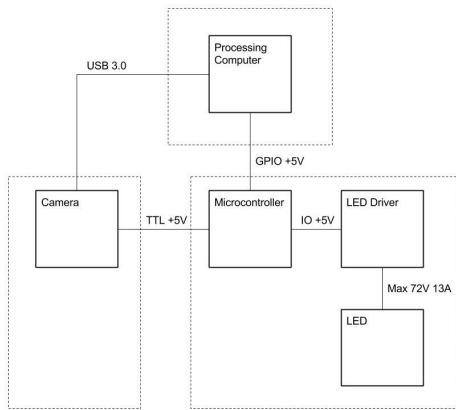


Fig. 2. Electrical Interfaces.

Fig. 2 shows the main components of the system. The camera is triggered by the software in the processing computer. The camera's flash output is connected to the microcontroller, which controls the length of the flash pulse to the LED driver. After exposure, the image is transferred through the USB 3.0 connection. The exposure level is checked and if it is ok, the image is analyzed, and the data is stored. If the exposure is too high or too low, one of two GPIO signals is set to the microcontroller. One to increase and one to decrease the length of the flash pulse for the next flash.

A. Camera and Illumination

The camera is a uEye UI-3370CP-NIR. Its sensor has 2048x2048 active pixels on a 5.5 μm pitch and pipelined global shutter pixels which allow exposure during read out.

The lens in use is Opto Engineering TC4M004-C, with 4x magnification. With the described camera sensor it gives an object field of view of approximately 2.8 times 2.8 mm.

The background illumination is a Mightex LCS-0455-03, with a 22 mm collimating lens. The LED produces low-coherent light in a spectra with its peak intensity at 455 nm (blue). The 22 mm lens projects the light into a square beam approximately 8 times 8 mm at the point of the object plane.

B. Flash Driver

The LED is powered by a Picolas LDP-V 10-70 driver module. The driver is used to produce 12 A current which is enough to get an exposure in our system by a 200-300 ns long pulse.

The pulse length is controlled using a FreeSoC2 (System on Chip) development board from SparkFun. The shortest pulse possible is one clock cycle, which is 13 ns. It uses two GPIO inputs, one to increment and the other to decrement the length of the control pulse. One input is used to trigger the pulse from the camera and one output is connected to the LED driver.

C. Casing

The camera and the illumination are weather protected by two IP 66 camera housings (Bosch UHO-HBGS-51). The

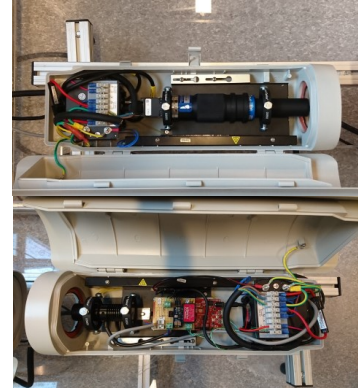


Fig. 3. Opened camera housings. Upper image shows the camera and the telecentric lens. Lower image shows the illumination including the current driver and the (partly hidden) microcontroller card.

housing are mounted on a 40 mm aluminum boom, fixing the distance between the housings. The space between the front glasses, approximately 113 mm wide, is where the stream of air may pass. The housings have thermostatic regulated heating both inside the casing and a heating element on the front glass, extending the lower temperature to -40 °C. They also contain a fan that continuously circulates the air inside the housing. See Fig. 3.

D. Calibration

To calculate the liquid water content, droplet mass and the total measuring volume is needed. Depending on how the size measurement is done, different size calibration curves will be achieved. We use a stage micrometer scale with dots printed in chrome on a silicon glass as reference object. The pattern scale feature printed dots in diameters of 2 μm , 3 μm , 4 μm , 5 μm , 6 μm , 7 μm , 8 μm , 9 μm , 10 μm , 25 μm , 50 μm , 75 μm and 100 μm . See Fig. 4 left.

A linear translation stage, see Fig. 4 right, is used to move each of the calibration dots in and out of focus. From the image analyze we get the measured size d^M of these dots and a value of the edge sharpness, x .

We use the Matlab "fit" command to create two second degree approximation surfaces. z_1 approximates dot diameters from 2 to 10 micrometers, and z_2 for diameters from 10 to 100 micrometers. See equations (1) and (2).

$$z_1 = p_{00} + p_{10}x + p_{01}d^M + p_{20}x^2 + p_{11}xd^M + p_{02}(d^M)^2 \quad (1)$$

$$z_2 = q_{00} + q_{10}x + q_{01}d^M + q_{20}x^2 + q_{11}xd^M + q_{02}(d^M)^2 \quad (2)$$

p_{xx} and q_{xx} are the constants derived from the calibration.

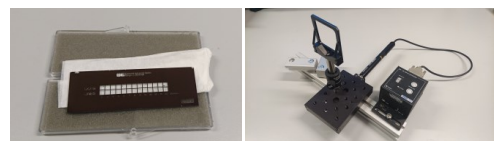


Fig. 4. The stage micrometer scale used for calibration (left) and the translation stage (right).

Since the derivative of the edge depends on how much out of focus the object is, there will only be a discrete number of images throughout the z-direction, where the gradient is strong enough to detect the edge. The number of images times the distance between each image we call the measuring range, z_{range} . See Fig. 5.

The resulting z_{range} depends on the size of the dot and is approximated by an exponential function (3).

$$z_{range}(d^T) = k_1 e^{k_2 d^T} + k_3 e^{k_4 d^T} \quad (3)$$

k_1, k_2, k_3 and k_4 are constants calculated from the calibration measurement and d^T is the true diameter.

E. Image Processing and Droplet Measurement

The image processing is implemented on an Advantec ARK-1123 embedded box PC with an Intel Atom E3825 DC chip running at 1.3GHz. The algorithms are coded in C++ partly using the OpenCV (Open Source Computer Vision) library under Linux Ubuntu 14.04 LTS.

Droplets are detected by selecting closed curves created by an edge detection algorithm. The edge detection is done by a 13x13 pixel Laplacian of Gaussian [7] convolution kernel. The threshold of 0.002 is based on normalized (0,1) image. After edge detection, a boundary fill function is used to filter out unbounded contours. See Fig. 6. This method is described thoroughly in [1].

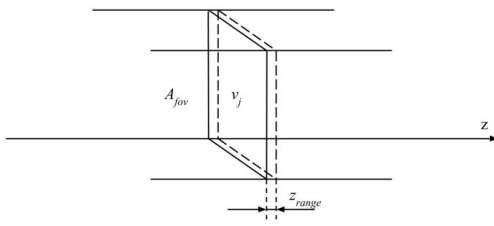


Fig. 5. Measurement volume v_j is the z_{range} multiplied by the area field of view A_{fov} .

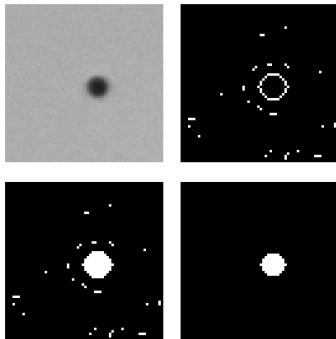


Fig. 6. Ten micrometer dot (upper left), edge detected (upper right), filled (lower left) and subtracted to a single blob (lower right) [1].

All pixels within the edge detected boundary are counted, corresponding to an area in the object plane. As was seen in [1], this area diverts quite a lot from the real cross sectional area of a particle, especially for diameters less than ten micrometers. Therefore we instead use the size of the shadow, and a value of the second derivative of the edge to estimate the true diameter.

To get a value of the size of the shadow, we try to find an approximation of the shadow impact based on the negative intensity within the edge detected boundary. First we measure the background intensity, $I_{background}$, to compensate for different intensities in different parts of the image. The shadow area is adjusted by a division between the sum intensity of the pixels inside the area and the average background intensity (4).

$$a_{adjusted} = a_{pixels} - \frac{\sum I_{center}}{I_{background}} \quad (4)$$

This means that a dark shadow in a dark area of the image appears similar to a light shadow in a light area. It also means that a particle that is right in focus and has sharp edges will get similar impact as the same size of particle out of focus which shadow is smeared out.

The measured diameter is then calculated by assuming a circular disc (5).

$$d^M = 2 \sqrt{\frac{a_{adjusted}}{\pi}} \quad (5)$$

The true diameter d^T can be seen as a function of the measured diameter d^M and the edge sharpness (maximum second derivative), x . d^T follows z_1 or z_2 for true diameters below or above 10 micrometers, respectively. To smooth out the transition from z_1 to z_2 we calculate a flat surface, z_3 , between $7 < d^M < 13$ so that d^T (6).

$$d^T = \begin{cases} \frac{1}{2}(\min(z_2, z_1) + z_3), & 7 \leq d^M < 13 \\ z_1, & 3 \leq d^M < 7 \\ z_2, & 13 \leq d^M < 100 \end{cases} \quad (6)$$

F. LWC and MVD Calculation

When we have the true diameter d^T it is possible to estimate the range where the droplets of this diameter would be detected. The measurement range calibration gave a value for each of the measured dots with known size. To get the measurement range for any size, we use the approximation (3) of the measured ranges.

The mass m_j of each droplet j is calculated by using the volume of a sphere with diameter d_j and the water density 1 g/cm^3 to calculate the mass. The measuring volume V_j is the measuring range times the area field of view. The LWC is calculated for each image as the sum of all droplets masses in the image divided by their expected measuring volume. To increase the measurement volume, each droplet's contribution to the LWC is accumulated during the last ten images, and the true LWC is the total sum divided by ten.

The median volume diameter, MVD, is given at the point where half of the total volume of liquid content in a fixed air volume consists of droplets with diameters larger and the other half has smaller diameters. To get the MVD from one image,

we first calculate the LWC for that image. Then we sort all $\frac{m_j}{v_j}$ and count the index number j until we get the sum $LWC/2$. The MVD is given by the mean of the last counted particle's diameter and the diameter of the next uncounted particle.

To average the MVD of several images we need to weigh the MVD with the LWC for each image. If we have m images, and give the properties of each image the index k , the average MVD for all images is:

$$MVD = \frac{\sum_{k=1}^m (MVD_k LWC_k)}{\sum_{k=1}^m LWC_k} \quad (7)$$

G. Fog Chamber

The fog chamber is needed partly for practical reasons since natural fogs tend not to occur just when we are ready to test. It gives an indication of how the instrument will behave in a real measurement. It is also a verification of the instrument's water ingress resistance.

The chamber has a frame made of 30 mm aluminum profiles, fitted with transparent 6 mm polycarbonate walls on all sides using rubber sealing strips. The droplets are produced using an ultrasonic fog generator pushing the droplets to the chamber through a flexible tube approximately 30 mm in diameter and 500 mm long. Next to the fog inlet, there is a dry air inlet with a speed adjustable fan. See Fig. 7. On the back of the chamber there is a similar sized outlet for air and moisture.

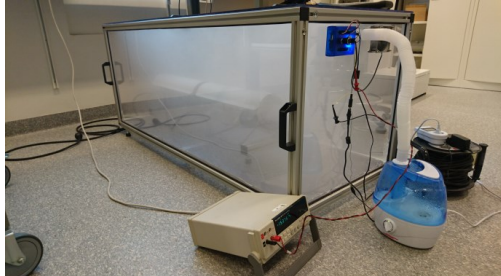


Fig. 7. Fog chamber with connected droplet generator (blue container) and a multimeter used for fan power measurement. A Beaglebone Black microcontroller (blue box) is used for fan speed regulation.

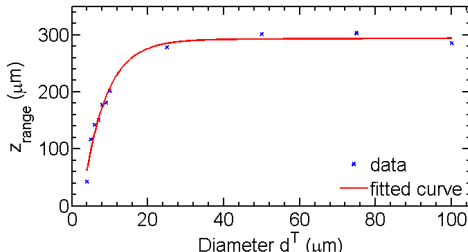


Fig. 8. Results from the calibration of the measuring range using a stage micrometer scale. Blue "x" represent the range in which the dot of each given diameter is detected with the droplet detection algorithm. The red line is the approximation curve implemented in the sensor.

III. RESULTS

A. Calibration

The translation stage was moved in steps of one micrometer in the z-direction and one image was analyzed for every step and every dot on the stage micrometer. The result was fitted in the approximation curves (1-3).

Fig. 8 shows the measuring range calibration measurements (blue "x") and the fitted approximation curve (red line).

B. Weather Protection

The moisture resistance of the measurement system was tested by placing the probe in the fog chamber. Although the bottom of the chamber was quickly wet by condensation, the front glass of the camera houses remained dry, even with LWC occasionally as high as 8 g m⁻³. See Fig. 9.

C. Droplet Distribution and Step Response

By using the constants derived from the calibration in (1) and (2), a diameter value was estimated for each droplet. A histogram of a sample distribution, together with a fitted lognormal curve is shown in Fig. 10.

The system was tested by changing the effect of the fog generator and changing the drive current of the fan. All droplets were measured and the data of each individual droplet was stored. Examples of measurement of MVD and LWC are shown in Fig. 11-14.



Fig. 9. Front of the probe during measurement. Water is visible on the bottom of the fog chamber and on parts of the camera housings, but not on the glass.

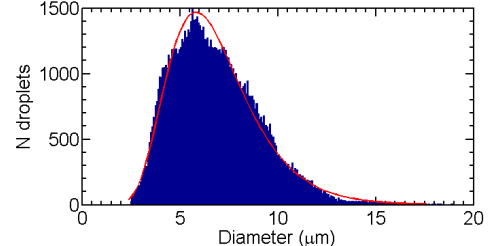


Fig. 10. Histogram of 99188 measured droplets in a one hour run with constant water and air input. The diameters d^T were calculated using the calibration formulae (3). The distribution is compared with a lognormal curve using the "histfit" function in Matlab. Diameters less than three micrometers were excluded.

A step increase in LWC by changing the effect of the water droplet generator gave a rise time of 234 seconds to the mean LWC 1.8 g m^{-3} with a 44 percent overshoot. See Fig. 11.

A step increase in the LWC by changing the fan speed gave a rise time of 174 seconds to the new mean LWC at 7.1 g m^{-3} with an overshoot of 22 percent. See Fig. 13.

Fig. 11 and Fig. 12 show a step increase of power to the water droplet generator starting from zero Watt. Fig. 13 and Fig. 14 show results of a step decrease in fan power.

D. Speed

The speed was measured over a sequence of 11500 analyzed images. This series took 22400 seconds to finish, giving an average time of 1.95 seconds per analyzed image. Approximately 0.12 s (6 percent) of this time is the transfer time of the image from the camera to the computer memory and 1.83 s (94 percent) is used for image processing.

IV. DISCUSSION

A. Weather Protection

The camera housings are classed with the ingress protection rating IP-66 meaning they should withstand water projected in powerful jets. This was not fully tested, but since the concentration of water inside the fog chamber was more than enough to damage the electrical components, should it have entered the housings, we believe the ingress protection is good enough. The heating also made the front glass clear from condensed water during all tests.

The heating is temperature controlled, so in freezing temperatures the heating power will increase. During all measurements, no condensed water was observed on the front

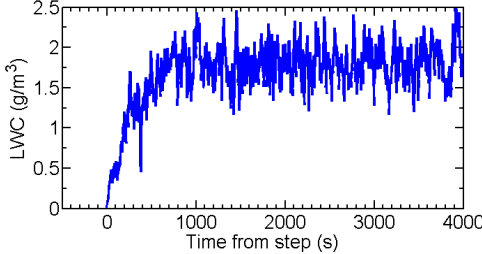


Fig. 11. A step increase in the LWC by increasing the power of the water droplet generator from zero to 14 W. Fan power was constant.

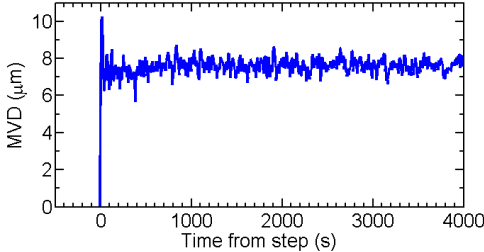


Fig. 12. MVD measured during a step increase of the power of the water droplet generator from zero to 14 W. Fan power was constant.

glasses. But in very strong icing conditions, the heating may not be enough prevent possible build-up of ice from affecting the measurement.

B. Droplet Distribution

The lognormal is often used as approximation of a natural distribution of fog droplets. Therefore we see how the measured droplet distribution fit in a curve approximation. The probability density function of the lognormal distribution is defined in (8).

$$f(d^T | \mu, \sigma) = \frac{1}{d^T \sigma \sqrt{2\pi}} \exp \left\{ \frac{-(\ln d^T - \mu)^2}{2\sigma^2} \right\} \quad (8)$$

Here e^μ is the median diameter and e^σ is the standard deviation of the distribution.

In Fig. 10, we see that the measured distribution seems to fit very closely to a lognormal distribution with the median diameter 6.5 um and the standard deviation 1.4 um.

The MVD did not vary as much as the LWC during the test runs. At some rare occasions, one droplet was measured that was significantly larger than others, e.g. 20 micrometers in diameter, thus increasing the MVD and LWC momentarily. Usually there seemed to be a small negative dependency, i.e. that the MVD decreased slightly with higher LWC.

C. Image Processing

The main technique to detect droplets and to find the measuring range was using edge detection by the Laplacian of Gaussian, and selecting closed curves by flood filling the background.

Since the background illumination was created by a collimated LED source, the background intensity was not completely even. Therefore simple thresholding would not work

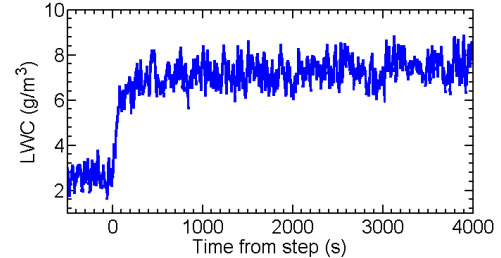


Fig. 13. Step increase in LWC by decreasing the fan power from 0.6 to 0.1 W. Water droplet generator power was constant.

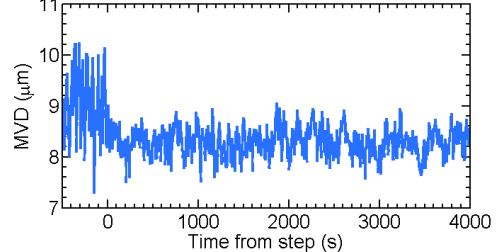


Fig. 14. MVD measured during the step decrease of the fan power from 0.6 to 0.1 W. Water droplet generator power was constant.

directly to find droplets. But thresholding could be used for pre-processing if used in combination with a flat-field correction.

D. Speed

The measurement volume for one image is not constant since the measurement range depends on the size of the droplet. But to get an approximation of the sampling rate we can assume we have ten micrometer particles and a measurement range of 0.2 mm. This gives a sampling volume of approximately 1.5 mm^3 .

Using an image speed of 0.5 images per second we get a sampling rate of $0.8 \text{ mm}^3\text{s}^{-1}$. This is much lower sampling rate than e.g. the HOLODEC's $5 \text{ cm}^3\text{s}^{-1}$ [8]. Like the HOLODEC, but unlike techniques based on laser spectrometry, the imaging instrument's sampling rate is not depending on the speed of the air flow.

In this project, the processing computer was shown to be rather slow for image processing. Sampling speed may be increased a lot by using a dedicated image processing and data transfer hardware. Parallel computing on field programmable gate arrays (FPGA) is a known method for hardware acceleration of image processing [9]. The image sensor used has a maximum frame rate of 180 frames per second in full resolution.

The sampling rate could also be increased by changing the optics to get a lower magnification. This would both increase the area field of view and the measurement range according to the optical analysis in [1], albeit on the cost of a lower resolution in the object plane.

E. Fog Chamber

We are able to control the liquid water content, simply by adjusting either the inlet of dry air or the power of the fog generator. By comparing the two step responses, we see that decreasing the air speed of the dry air is 60 seconds faster than increasing the water inlet.

We also see that the instrument's heating is enough to keep the lens glass free from water in high LWC conditions.

Unfortunately the chamber we built is slightly too small to enclose a second instrument. A similar but larger chamber can be built, but it may still not be suitable for other measuring instruments. Devices based on forward scattering require a measurable wind speed and rotating cylinders require freezing temperatures.

F. Future Work

When measuring droplets in the real world, a comparative study should be done.

The calibration is done using a single reference object. At least one other object, like dripping water droplets or a calibrated distribution of glass beads should be used for comparison. When using a fixed stage micrometer one should also consider possible differences depending on how close or far from the optical center the dot is measured.

The measuring speed is important, therefore considerations of the hardware design should be done. Image processing methods could also be improved.

Further testing should be done outside or in a test facility capable of controlling temperature and wind speeds. The tests should be done at wind speeds and temperatures close to those experienced by wind turbines in cold climates.

V. CONCLUSIONS

The described instrument was proven to withstand and function in a very humid environment inside the fog chamber. We also proved we could control the LWC in the fog chamber using a fan and ultrasonic humidifier.

There was no wind produced inside the fog chamber and the tests were completely done in room temperature.

REFERENCES

- [1] S. Rydblom and B. Thornberg, "Liquid Water Content and Droplet Sizing Shadowgraph Measuring System for Wind Turbine Icing Detection," *IEEE Sensors Journal*, vol. 16, pp. 2714-2725, 2015.
- [2] S. G. Cober, G. A. Isaac, and J. W. Strapp, "Characterizations of aircraft icing environments that include supercooled large drops," *Journal of Applied Meteorology*, vol. 40, pp. 1984-2002, 2001.
- [3] L. Makkonen, "Analysis of Rotating Multicylinder Data in Measuring Cloud-Droplet Size and Liquid Water-Content," *Journal of Atmospheric and Oceanic Technology*, vol. 9, pp. 258-263, Jun 1992.
- [4] M. C. Homola, M. S. Virk, T. Wallenius, P. J. Nicklasson, and P. A. Sundsø, "Effect of atmospheric temperature and droplet size variation on ice accretion of wind turbine blades," *Journal of Wind Engineering and Industrial Aerodynamics*, vol. 98, pp. 724-729, 2010.
- [5] N. L. Miles, J. Verlinde, and E. E. Clothiaux, "Cloud droplet size distributions in low-level stratiform clouds," *Journal of the atmospheric sciences*, vol. 57, pp. 295-311, 2000.
- [6] W. R. Sand, W. A. Cooper, M. K. Politovich, and D. L. Veal, "Icing conditions encountered by a research aircraft," *Journal of climate and applied meteorology*, vol. 23, pp. 1427-1440, 1984.
- [7] D. Marr and E. Hildreth, "Theory of edge detection," *Proceedings of the Royal Society of London. Series B. Biological Sciences*, vol. 207, pp. 187-217, 1980.
- [8] J. P. Fugal and R. A. Shaw, "Cloud particle size distributions measured with an airborne digital in-line holographic instrument," *Atmospheric Measurement Techniques*, vol. 2, pp. 259-271, 2009.
- [9] J. Rettkowski and A. Boutros, "Real-time pedestrian detection on a xilinx zynq using the HOG algorithm," in *2015 International Conference on ReConfigurable Computing and FPGAs (ReConFig)*, 2015, pp. 1-8.

Paper III

Comparative Field Study of LWC and MVD using two Droplet Measuring Instruments and an NWP Model

S. Rydblom, B. Thörnberg

Comparative Field Study of LWC and MVD using two Droplet Measuring Instruments and a NWP Model

Staffan Rydblom, Benny Thörnberg

Mid Sweden University, Sundsvall, Sweden

Esbjörn Olsson

Swedish Meteorological and Hydrological Institute, Sundsvall, Sweden

Abstract

The Droplet Imaging Instrument (DII) is a new instrument for cost effective in-situ measurements of the size and concentration of water droplets. It is designed specifically for the detection of structural icing.

The droplet size distribution and the concentration of atmospheric liquid water are important parameters for the prediction of the formation of ice on wind turbines and other structures. To improve current weather models and to predict icing at a number of specific locations there is a need to explore cost effective solutions using standard methods and off-the-shelf hardware.

This paper describes a study of the atmospheric liquid water content (LWC) and the median volume diameter (MVD) of the droplets using the DII and a reference instrument (The CDP-2 from Droplet Measurement Technologies Inc.). It is done at the weather measurement station of the Swedish Meteorological and Hydrological Institute (SMHI) on top of Klövsjö mountain in mid-Sweden.

The instruments are installed on a mast constructed to rotate with the direction of the wind. For a second validation, we carry out weather simulations around the site using the HARMONIE-AROME numerical weather prediction (NWP) model.

The study shows that there is a systematic difference between the two compared instruments. Probable reasons for the difference are discussed.

The LWC and MVD predicted by the HARMONIE-AROME model at a site with complex topology gives good agreement when a special domain with 500 meters horizontal resolution is used, but less agreement when 2.5 km resolution is used. It also shows that the MVD increases significantly when

droplets larger than $50 \mu\text{m}$ in diameter are measured, which the model data does not predict. This indicates the importance of measuring the whole range of droplet sizes for in situ verification of model data and for the prediction of icing on structures.

Keywords: Icing, Wind Power, Cold Climates, Liquid Water Content, Machine Vision, Droplet Imaging Instrument, Cloud Droplet Probe, HARMONIE-AROME, Numerical Weather Prediction

1. Introduction

Icing is caused by atmospheric liquid water freezing on the surface of a structure, such as the blades of a wind turbine, power line or another weather exposed structure. The severity of the icing depends on many factors, e.g. the duration, the shape and surface of the structure, the wind speed, the atmospheric concentration of liquid water, the size distribution of water droplets and the mix of ice and snow [1, 2, 3, 4, 5].

The Liquid Water Content (LWC) in atmospheric studies is usually given in $\text{g} \cdot \text{m}^{-3}$ [6]. The size distribution of droplets when considering the collision efficiency is most effectively estimated by the Median Volume Diameter (MVD) [7]. The MVD is the point in the distribution of droplet diameters where half of the total amount of water in the distribution of droplets is above the diameter, while the other half is below. Weather models today include the LWC and the MVD, making it possible to estimate the risk of icing based on general weather data [8]. The LWC and the MVD at ground level depends very much on the local geographical topology, and measurements using in situ instruments are quite rare. There have been trials to verify NWP models using in-situ data [9]. The LWC and the MVD e.g. can be measured by analyzing satellite or radar images. In-situ measurements, using optical or collecting devices, are unfortunately still quite rare due to the instrument cost and other practical issues.

The Droplet Imaging Instrument (DII) is designed to find a simple, cost effective and robust technique to measure LWC and MVD in order to predict icing on structures [10, 11]. An automatic sensor based on this technique could be used to trigger ice protection systems used for wind turbines in cold climates [12]. Shadowgraphy is a technique commonly used in various particle and particle flow studies. The system continuously images a defined space using a light sensitive CMOS camera equipped with a telecentric lens. It is

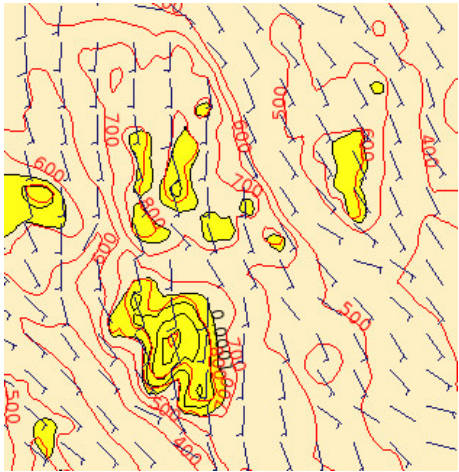


Figure 1: Graphical presentation of data from the HARMONIE-AROME weather model covering Klövsjö and the surrounding mountains at a specific point in time using 500 m resolution. Yellow areas are where the model predicts an LWC more than $0.1 \text{ g} \cdot \text{kg}^{-1}$ (Grams of water per kg air.)

calibrated using a micrometer dot scale with dots of verified sizes printed on a transparent glass. Since the instrument is new, the sizing is verified using four samples of polymer microspheres, calibrated in size by the National Institute of Standards and Technology (NIST). The functional simplicity and robustness of the DII opens the possibility to mass produce and distribute Internet connected instruments based on this technique on a larger geographical scale.

During the winter of 2016-2017, the prototype instrument was placed on the Klövö mountain, Sweden, at one of the Swedish Meteorological and Hydrological Institute's (SMHI) measuring stations, position $62^{\circ}29'41''\text{N}$, $14^{\circ}9'27''\text{E}$, 802 meters above sea level. Measurements are available from November 2016 to March 2017. Results from these are presented. A parallel measurement of LWC and MVD was done using a Cloud Droplet Probe CDP-2 (CDP) from Droplet Measurement Technologies Inc. (DMT). The results from the two instruments have been compared.

During the period 1 December, 2016 to 10 March, 2017 there were four instances of severe fog at the measurement site: 11 December 2016, 3-6 February 2017, 10 February 2017 and 28 February to 7 March, 2017.

1.1. Scientific Contribution

Long term field studies of the LWC and the MVD using in-situ instruments are not very common. To our best knowledge there is no previous similar study comparing two instruments that measure the same droplet size range using two different measurement techniques and comparing the results with the values predicted by a NWP model in two resolutions.

The study shows that the DII, which is a new instrument, measures LWC accurately using a 30-minute average, but that there is a systematic difference between the two compared instruments, both in size and concentration measurement. The measurement using NIST calibrated polymer microspheres shows that the DII measures the diameter of spherical particles well in the range from five to 50 μm .

Data from the field study of LWC and MVD shows that there is a difference between model predicted and measured LWC, and that this difference can be reduced by using a higher NWP model resolution. Assuming that structural icing can be predicted by measuring the LWC and the MVD, the study shows that the DII is an instrument that can be used for this purpose. It also shows that the technique can be used for NWP model data verification and assimilation.

1.2. Related Instruments and Techniques

Optical measurement of cloud particles is a field of research that has evolved over the decades. In 1970 Knollenberg described the Optical Array Probe, a system used to make two-dimensional images of droplets as they pass a laser-illuminated array of photodetectors [13]. Using modern camera techniques, ice and liquid water particles can be imaged with a much higher level of detail. The Cloud Particle Imager (CPI) and 2D-S by SPEC Inc., the Cloud Imaging Probe (CIP) and Precipitation Imaging Probe (PIP) by DMT are examples of a commercially available instruments designed for the conditions of aircraft flight.

The Ice Crystal Imaging [14] probe is a recently developed imaging instrument for measurement and classification of ice and water particles. Like many other ground-based instruments it makes use of active ventilation to draw air and particles into a region of controlled flow. The illumination is a

background bright field similar to the DII and a few other particle imaging systems.

Shadowgraph systems for industrial and other applications are e.g. the ParticleMaster by Lavision GmbH and the VisiSize by Oxford Lasers Ltd..

In-line holography is a related technique of reconstructing droplets from images of the interference patterns created when using a coherent light source [15]. The working principle is similar to imaging and shares most of the pros and cons. Holographic systems can also be implemented using low cost material [16]. Since the interference patterns will be created for all particles in the illuminated area, a larger volume could be used in each image compared to an imaging system, which is limited by the optical depth of field [17, 18, 19]. Using a greater part of the distance between the camera and the illumination means that the air flow dynamics will affect the sample. Instruments using in-line holography for both airborne and ground based use exist and are described in papers [18, 19, 20, 21].

2. Materials and Methods

2.1. Measurement Object and Environment

Icing is mostly caused by cloud droplets measuring between 10 μm and 30 μm in diameter [22, 23, 4]. Meta studies of droplet distributions in low altitude clouds [24, 25] show that the LWC is highly variable, even during the same measurement. Icing may start with LWC as low as 0.1 $\text{g} \cdot \text{m}^{-3}$ but will be more severe with higher LWC. Icing also often occurs in mixed phase conditions, when both ice crystals and liquid water co-exist.

Since our focus is on measuring liquid water particles, the morphological problem is less complicated than determining the size and weight of ice crystals. The diameter of a spherical object can be found by assuming that the shadow of a sphere is similar to a solid disc. By using the gray scale information of the edge pixels, a sub-pixel precision can be achieved.

2.2. The Droplet Imaging Instrument

The system works by shadowgraph imaging using a high speed digital camera and LED background illumination. The camera and lens is mounted in an aluminum housing with heated front glass. Facing the camera in an identical housing is a blue LED that produces a short flash of collimated light directed towards the camera. Particles passing between the camera and the illumination appear as dark shapes against the bright background. Each image is scanned for particles. If a particle is detected, it is evaluated for roundness according to ISO 12181 [26]. A particle is only measured if the value of roundness is ≥ 0.85 .

Calibration of the instrument is done using a micrometer scale of printed dots on a silicon glass. The dots on the micrometer scale were measured visually using a Leica microscope connected to a digital camera using lenses with two different magnifications: 40x and 100x. The average diameters of the dots, with the exception of the 100 μm dot were found to be within $\pm 0.2 \mu\text{m}$ of their nominal diameter. The size is estimated by measuring the relative blackness of the shadow, excluding the light passing through the middle of the droplet compared with the background light. This value and a measure of the sharpness of the edge is used as input to a calibration function.

The edge detection algorithm uses a Laplacian of Gaussian operator [27, 28] to create a binary image of a closed circular curve for edges of droplets where the edge is in focus. A functional description of the principle can be

found in [10]. The weather protected prototype instrument is described in [11].

2.3. Microspheres Measurement

Four different sizes of calibrated microspheres were tested. The microspheres are manufactured by Thermo Scientific. The mean diameters are calibrated traceable to the “Standard Meter” through the NIST. The composition is polystyrene DVB (divinylbenzene). The index of refraction is 1.59. The stated mean diameters are calibrated by the manufacturer using optical microscopy and a stage micrometer calibrated by NIST (SRM 2800 SN411).

The microspheres were dispensed by blowing compressed air through a glass container with dry microspheres. See Figure 2.

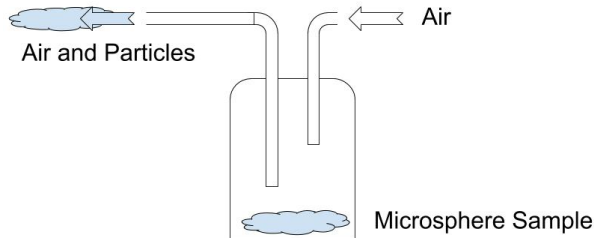


Figure 2: Dispenser for Microspheres.

2.4. The Cloud Droplet Probe

The CDP-2 belongs to a category of instruments measuring the light scattered forward by single particles [29, 30]. These work by illuminating a small region with a focused laser beam and measuring the intensity of the light scattered by passing particles. A water droplet can be seen as a transparent lens. Assuming the droplet is spherical and the refractive index is known, the signature of the scattered light of a defined wavelength and scattering angle can be calculated analytically by the Mie solution to Maxwell's equations [31, 32]. Particles passing the beam that are classified

as droplets within the sampling space will be measured according to their phase signature and counted in a number of predefined size bins.

There are also some uncertainties in particle sizing that are common for all instruments using forward light scattering. Due to the nonmonotonic relation between particle size and the scattering cross section, particles of different diameters can have the same optical diameter [31, 33, 29, 34]. Other uncertainty factors are e.g. particle coincidence and non-uniformity or misalignment of the laser. Suggestions have been made to decrease the Mie scattering error by moving the bin thresholds [35, 34]. In this measurement we have kept the default bin sizes. The default bin sizes are 2-3 μm , 3-4 μm etc. up to 15-16 μm , after which they are 16-18 μm , 18-20 μm etc. up to 48-50 μm . Particles generating a higher signal are counted in an overflow size bin.

The sampling volume primarily depends on the speed of the passing air/particle flow and the uniformity of the laser beam. Small particles can only be counted where the laser intensity is highest and large particles are more likely to cross the beam edge, thus being disqualified.

The wind speed is not measured by the CDP itself. In order to calculate the LWC we use a separate anemometer, included in the combined weather sensor Eolos-Ind from Lambrecht meteo GmbH. The Eolos-Ind also includes sensors for wind direction, temperature, humidity and barometric pressure. The wind direction is used as input to control the direction of the DII and the CDP.

A functional description of the CDP and many other related instruments can be found in e.g. [30].

2.5. Installation

Figure 3 shows the installation. The two camera houses of the DII are placed on top and below the smaller CDP below. The Lambrecht Eolos weather sensor is placed to the far left, mounted on a horizontal boom. In the middle, to the right of the Eolos, there is a mobile communication antenna. In the bottom center, the top of the shortened lattice mast can be seen, and behind it, the box containing the DII processing computer, the CDP data collection computer and the communications router. The complete installation measures approximately five meters in height. An electric servomotor mounted at the base of the pole inside the lattice mast rotates the two instruments automatically to follow the horizontal direction of the wind.



Figure 3: Image of the complete installation at the SMHI weather station in Klövsjö.

2.6. Data Presentation

The sampling volume of the CDP is significantly larger than the DII's in its current configuration. To be able to compare the data from the two instruments and the data from the NWP model we chose to combine the data using a moving average window of 30 minutes (± 15 min) and a step size of one minute.

2.7. The HARMONIE-AROME NWP

AROME (Application de la Recherche à l'Opérationnel à Meso Echelle) is the mesoscale (2.5 km resolution) version of the large scale ALADIN model (Aire Limitée Adaption Dynamique International) [36]. ALADIN (including AROME) shares code with the global ECMWF IFS (European Centre for Medium-Range Weather Forecasts, Integrated Forecasting System). ALADIN is a spectral limited area weather forecast model and has been developed to use the full non-hydrostatic equations (Euler elastic forms of the Navier Stoke's- equations). All meso-scale models are formulated in this way since the vertical velocities are large at the resolved scales due to convection and orographic forcing.

AROME has an advanced meso-scale physics parameterisation and has prognostic equations for rain, snow, graupel, cloud water and cloud ice. The microphysics is explicit and uses the Meso-NH ICE3 scheme where slow processes are separated from fast adjustment. There is a turbulence TKE (Turbulent Kinetic Energy) scheme. The radiation scheme is of the two-stream type and surface slopes are taken into account. HARMONIE-AROME (HIRLAM-ALADIN Research on Mesoscale Operational NWP in Europe) is an adaptation and improvement of the model configuration to fit conditions in northern and southern Europe. It can be distinguished from the AROME-France model [37, 36].

To be able to give a detailed description of the conditions at the site, SMHI agreed to run a special model domain locally with 500 meters horizontal resolution for a limited time. The operational forecasts are run at 2.5 km horizontal resolution, and they were used as initial conditions and lateral boundaries for the detailed simulations.

The deep convection is resolved, but there is a shallow convection scheme due to moist turbulence from the atmospheric boundary layer of the Kain-Fritsch [38] mass flux type.

The surface scheme considers exchange of energy (momentum, temperature, humidity) and water between the atmosphere and the surface. The surface properties have details from the Ecoclimap [39] data sets and a high resolution topography.

At SMHI, the HARMONIE-AROME model is used for short range operational forecasting. It is run in cooperation with the Norwegian Meteorological Institute. The initial conditions and boundaries for the operational forecasts are provided by the ECMWF global model.

Figure 4 shows the HARMONIE-AROME area that is used for the operational forecasts. For the detailed simulations around Klövsjö, the area shown in Figure 5 was used. The model ran for one month starting 3 November. A 12-hour forecast was produced four times every day beginning at 00, 06, 12 and 18 UTC. No assimilation of observations was used. From these forecasts it is possible to construct time series of the relevant parameters with an hourly time resolution. It can take a few hours for the different hydrometeor parameters, i.e. rain, snow, graupel and fog, to come to a balance with each other. To minimize these so-called spin-up problems, we chose to use the 7-12 hour forecast.

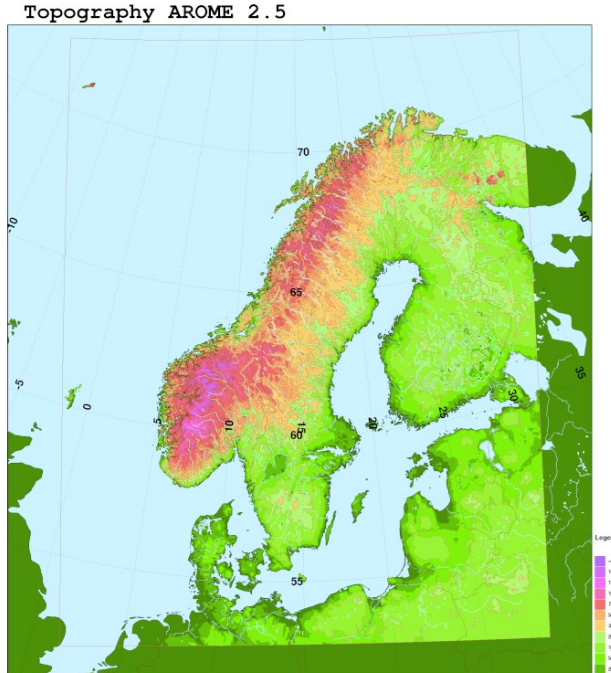


Figure 4: SMHI/Met Norway operational HARMONIE-AROME area, 2.5 km resolution.

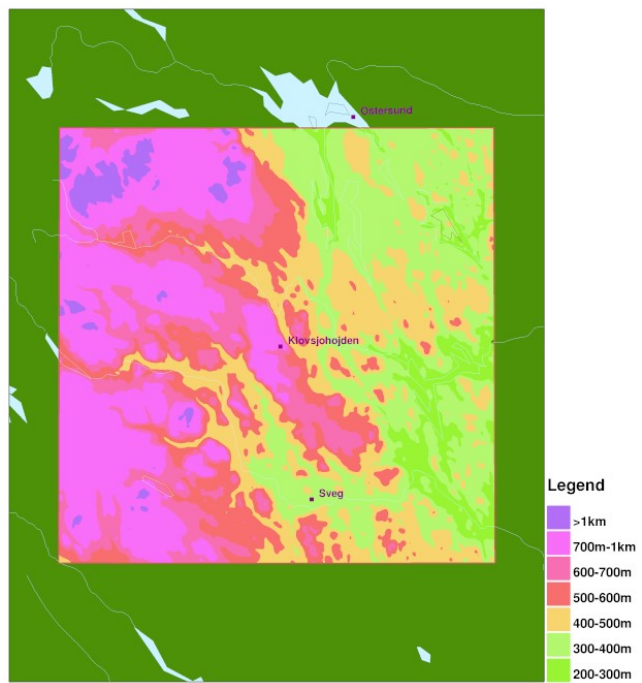


Figure 5: HARMONIE-AROME Klövsjö area, 500 meter resolution. Model topography.

3. Results

3.1. Measurement of Polymer Microspheres

Four NIST calibrated distributions of microspheres, approximately 5, 10, 20 and 50 μm in diameter were used, resulting in four different measured size distributions. All images were saved and visually inspected, resulting in some measurement outliers due to clogging of smaller particles or contamination of small particles among larger. The outliers that were identified as not of the real distribution are not included in the result shown. Histograms of the measurement can be found in Figure 6. A summary of the result is shown in Table 1.

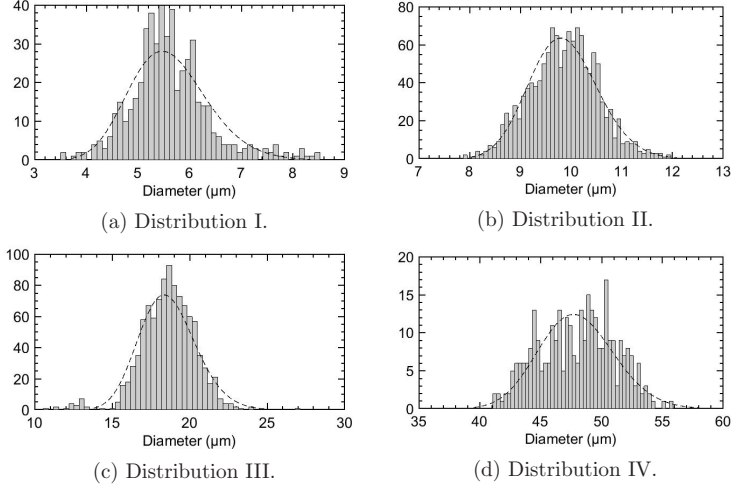


Figure 6: Histograms of the four measured distributions. The dashed line is a fitted lognormal of the weighted distribution.

3.2. Comparison of DII and CDP Data

We compare the instruments by studying the data from 28 February to 1 March. See Figure 7 and 8. Figure 7b shows the LWC measured by the CDP compared with LWC measured by the DII. Using the least square method

Distribution	I	II	III	IV
Stated Mean Diam.	5.3 (± 0.3)	10.3 (± 0.4)	19.1 (± 0.7)	49.4 (± 1.6)
Measured Mean Diam.	5.6	9.9	18.6	48.0
Stated Std dev	0.5	0.9	1.7	3.5
Measured Std dev	0.77	0.67	1.7	3.1

Table 1: Summary of the result from the measurement of NIST certified microspheres. All values are in μm .

on the whole data set gives an average quote of 0.27. The quote is drawn in the plot as a straight line from the origin.

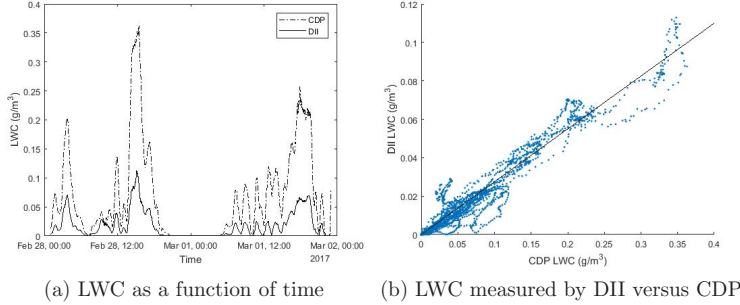


Figure 7: LWC measured by the DII and the CDP for 46 hours on 28-02-2017–01-03-2017.

Figure 8b shows the MVD measured by the CDP compared with the DII. The least squares method applied on the data set results in a quote of 0.77 and a very small offset of -0.3 μm .

The quote between the LWC values of the two instruments is plotted together with the wind speed in Figure 9. The least square average is plotted as a horizontal line at 3.65 (CDP LWC / DII LWC). The logarithmic scale is cropped with 238 quote values above 100 and 121 values below 0.1 of a total 2760.

3.3. Comparison of Measured and Modeled Data

Figure 10 shows the LWC and the MVD from the two instruments compared with the data from the HARMONIE-AROME model at 500 m resolution. The fog lasted for about 19 hours on 12-11-2016. The difference between

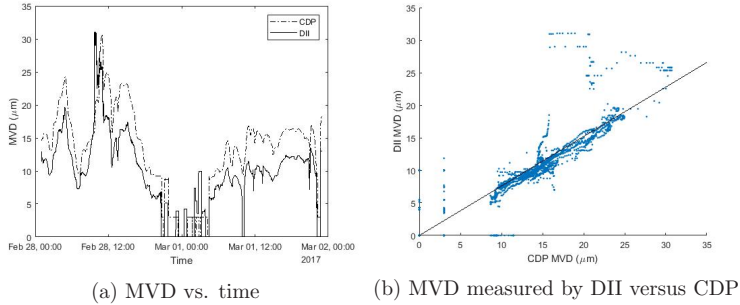


Figure 8: MVD minute values measured by the DII and the CDP for 46 hours on 28-02-2017-01-03-2017.

the two instruments follows the same systematic pattern as for other occasions. The HARMONIE-AROME model data of the LWC follows the general data of the LWC but fails to detect the large increase in LWC between 05:00 and 12:00. The predicted MVD of the model is closer to the actual values of the DII than the CDP.

Figure 11 shows the result from measurement 03-02-2017–06-02-2017. Unfortunately no data from the CDP was saved from this occasion due to a full memory. The double spike in the MVD diagram 11b at 04:17 and 04:41 on 05-02-2017 is mainly caused by two droplets, 51 and 74 μm (see Figure 14) in combination with a number of large droplets between 30 and 40 μm in diameter.

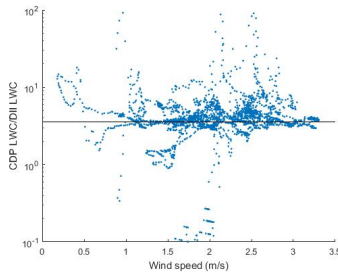


Figure 9: Relation between the wind speed and the quote between the LWC measured by the CDP and the DII. The vertical scale is cropped at 1 and 100. 238 values are above 100 and 121 below one out of a total of 2760.

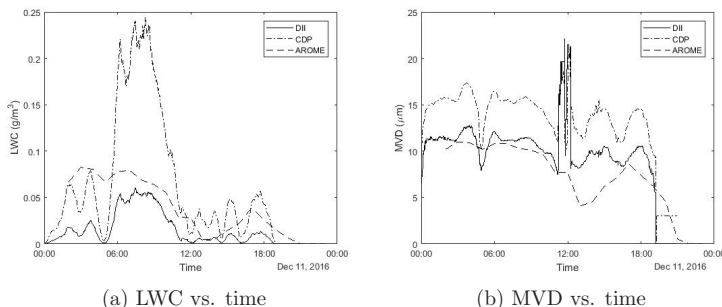


Figure 10: LWC and MVD measured by the DII and the CDP 11-12-2016. HARMONIE-AROME model data using 500 meter resolution.

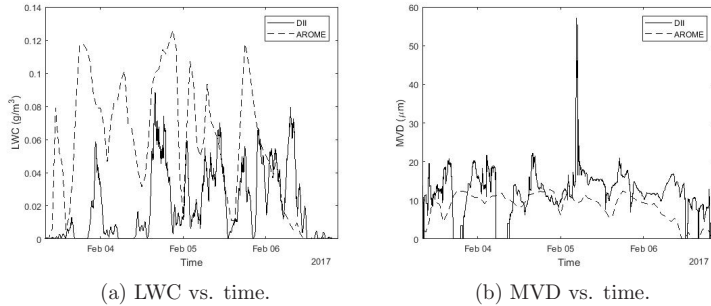


Figure 11: LWC and MVD measured 03-02-2017–06-02-2017 by the DII. HARMONIE–AROME model data using 2.5 km resolution, stored every 60 minutes.

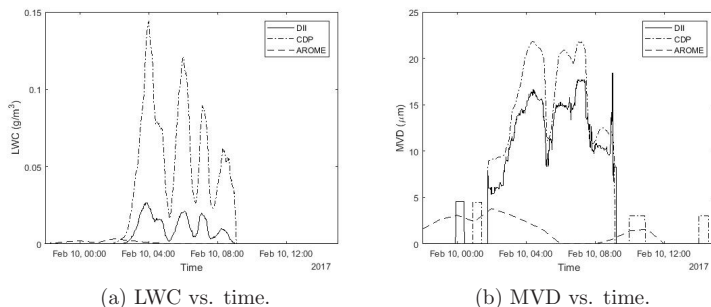


Figure 12: LWC and MVD measured by the DII and the CDP 10-02-2017. HARMONIE–AROME model data using 2.5 km resolution, stored every 60 minutes.

4. Discussion

4.1. Microspheres Measurement

Measured mean and standard deviation of all distributions are found to be within the stated calibrated values. This is a confirmation that the DII, calibrated by a micrometer dot scale measures the microsphere samples correctly.

The smallest microspheres tend to form larger clogs that are sometimes measured as single microspheres, probably due to static electricity. As can be seen in the five micrometer measurement, and Fig. 3, the result of some clogs becomes outliers in the expected distribution. This needs to be considered when solid microspheres are used as reference objects. Colliding liquid water droplets would of course coalesce into larger droplets, thereby changing the diameter.

The equipment and the dispenser was thoroughly cleaned between each measurement using compressed air. However, it is possible some microspheres or other contamination remained, thereby changing the size distribution slightly.

4.2. Roundness

A perfectly circular disc measured using an infinite resolution would have an expected roundness value equal to one. In practice, this is not possible to achieve in a digital image. But the contour is only used as detection criteria. Instead, the diameter is calculated using the negative shadow intensity. Therefore the contour roundness itself should not have very large impact on the accuracy.

The roundness criteria according to ISO 12181 [26] set at 0.85 in this measurement seems to work as expected. It excludes most irregular objects, like clogs in the polymer microspheres measurement. When measuring fog in cold climates, water droplets will be mixed with ice crystals. Most larger crystals will be sorted out by the roundness criteria. Small crystals, a few micrometer in diameter or less, are impossible to distinguish from liquid water droplets unless they are very different in shape.

A number of ice particles were observed. The DII is configured to measure the imaged area of all objects, both droplets and crystals and images that include large objects are saved. Examples of imaged ice particles can be seen in Figure 13. Ice particles are not part of the LWC, but may play an important role in the determination of the severeness of the icing.

4.3. Droplet Size Measurement

The CDP does not measure droplets larger than $50\ \mu\text{m}$. The detection of large droplets has a great impact on the MVD, which can be seen in Figure 10b and Figure 11b.

With a higher sampling speed than the speed achieved, it should be possible to reduce the time window while achieving the same precision.

4.4. Cause of Systematic Difference

The measured LWC of the DII and the CDP in Figure 7b differs by a factor of approximately 3.65 (CDP LWC / DII LWC). There may be several reasons for this difference.

Comparing the measured MVD of the DII and the CDP we get a quote between the two instruments of 0.77. This means that the MVD of the CDP is on average 30 percent higher than the DII. Since the LWC is proportional to the third power of the droplet size, an increase in the diameter of 30 percent will increase the LWC by $1.3^3 = 2.2$. Unless the droplets are affected by the instruments themselves, there are two possible explanations. One is that the two instruments measure the sizes of the droplets differently. The other is that the sampling volume differs depending on the size of each droplet for one or both instruments.

The CDP and its predecessors, have shown a tendency of oversizing droplets when calibrated by glass or polymer spheres [40, 35]. This could still explain some of the difference. The precision of the CDP size measurement is also limited by the fixed size bins, and by the pulse amplitude of the scattered light calculated from Mie theory [35, 32]. A small disturbance, like a slight misalignment of the laser beam, may cause a shift in the optical response pushing the size to the next or previous size bin [35]. The sampling area, i.e. the illuminated area that the particles must pass through to be recorded, is an average value given by the manufacturer on delivery.

From Figure 9 we conclude that there is no relation between the difference between the two instruments and the wind speed when the wind speed is below four meters per second.

The LWC of the DII of course depends on an accurate estimation of the sampling volume. While the image area can be determined accurately, the detection depth depends on the optical diffraction of the lens, which likely depends on the distance to its optical center. The sampling volume of the DII is then smaller than previously calculated because the calibration of the measurement range was only done at one location in the image, close to

the optical center, for each dot size. If this is the case, the error could be mitigated by adding the distance from the measured droplet to the center to the measurement range calculation.

4.5. Model Data

By comparing the results from 11. December with other dates, it seems that the high resolution gives values of LWC that are close to the measured, while the low resolution gives a LWC that indicates fog, but fails to accurately predict the amount or the time of occurrence. To predict icing at a particular location, the 500 m model resolution gives better agreement than the 2.5 km resolution. It is likely that the difference is caused by the complex topography at and around the measurement site.

4.6. Ice Crystals and Snowflakes

The main objective of the project was to measure the LWC in order to detect icing conditions for wind turbines and similar sensitive structures. But as shown [4], conditions when liquid water droplets are mixed with ice or snow may alter and worsen the ice build-up. Several particles of frozen water were imaged by the DII during the measurements. Figure 13 shows a sample.

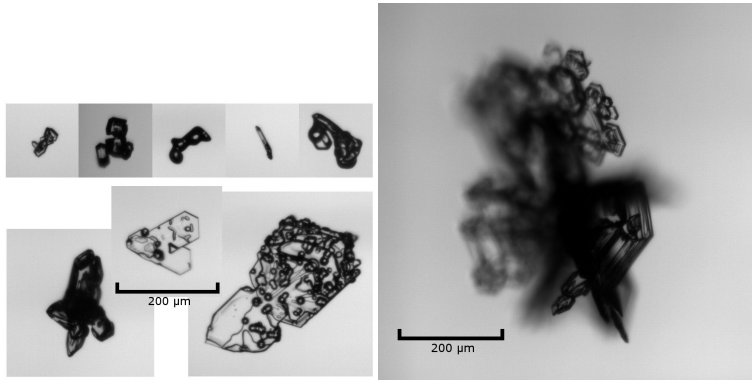


Figure 13: Ice particles imaged at different times.

4.7. Physical Design and Wind Speed

Clouds are present in both calm and windy conditions. To measure the LWC in a non-moving air mass using a dynamic sampling of passing particles, like the CDP, the instrument need to either be moved through the air or an active ventilation must be applied, otherwise it is difficult to know the concentration of particles. Usually, there is enough wind for the measurement to work. In any case the instrument may affect the measurement.

Altering the air flow will cause a local change in air pressure and concentration of particles around the instrument. It will also change the size distribution since large particles, due to their inertia, have less tendency to follow a Stokes flow. Particles, especially larger ones, may also collide with parts of the instrument. Many designers of droplet measuring instruments struggle with this problem.

The CDP is designed to measure droplets at high wind velocities, while the DII is not. Therefore we were concerned that the wind speed would affect the comparison. During the measurements in Klövsjö, the wind speed was usually only between one and four meters per second, at times close to zero. Plotting the quote between the measured LWC of both instruments against the wind speed confirms that for weak wind speeds, the aerodynamic design is less important. See Figure 9.

4.8. Sampling Speed and Volume

The sampling speed, i.e. the processed volume of air per second, of the CDP is linearly dependent on the wind speed. The sample area also depends on the size of the measured droplets, but the factory calibration value is given for all sizes. The sampling speed of the DII depends primarily on the image frame rate and the measurement range for each droplet size. At a wind speed of 2 m/s, the sampling speed of the CDP is $4.1 \cdot 10^{-7} \text{m}^3 \cdot \text{s}^{-1}$. This is 39 times higher than the sampling speed of the DII for 20 μm particles. To achieve the same sampling speed, the frame rate of the DII would need to be almost 200 s^{-1} . Different ideas to increase the sampling speed of the DII have been discussed in [10] and [11].

Despite the relatively low sampling speed and the small sampling volume of the DII, it seems that by averaging the LWC and the MVD over a period of 30 minutes, enough precision is achieved to be able to compare the two instruments. Since the purpose of the DII is primarily to detect conditions for icing on wind turbines, and provide in-situ observational data for NWP models, the achieved sampling speed may even be good enough, at least for

the latter. If the speed is good enough to decide when to switch on de-icing on the blades depends on how quickly the ice builds up, and what de-icing method is used. During icing, high LWC and high MVD are expected.

When comparing the 30 min moving average values for the period 28 February – 1 March, shown in Figure 7a and Figure 8a, there is very good agreement between the curves, with the exception of 11.30-12.00 when at least ten droplets 25-35 μm in diameters were measured by the DII, resulting in a significantly higher MVD and LWC measured by the DII than the CDP. The reason why the CDP did not measure any similarly sized particles on this particular occasion is not known. There is also a difference in the MVD when the LWC is very low resulting in a small number of measured droplets.

The drop size distribution of cloud droplets 3-50 μm in diameter have usually been considered to follow a lognormal or gamma curve [24, 41, 6]. This also applies to rain [42]. However, more recent measurements of drop size distributions show that the distribution greatly varies [43, 44, 45, 46]. Consequently, the results will depend on the measurement method and the sampling volume.

4.9. Large Droplets

The CDP does not measure particles larger than 50 μm . But if the distribution of droplets was following a lognormal, or gamma curve [24, 41] also for particles larger than 50 μm , enough large droplets should have been detected by the CDP to see an increase in the measured MVD. As demonstrated, this was not always the case. A possible explanation is that the larger cloud droplets do not follow the lognormal distribution when they are above a certain size. If this is true, the predicted MVD may be less useful for the description of a cloud aerosol distribution, as well as for conclusions about possible icing. In the case with supercooled large droplets, the LWC may be more important to measure than the MVD. But to fully understand this, a parallel measurement using an ice load instrument is required.

Figure 14 and Figure 15 show supercooled large droplets measured during the fog on 05-02-2017.

4.10. Icing and Future Works

During the study there were several instances when the LWC and MVD was high enough to lead to icing. A study to further investigate the connection between these parameters and the ice load according to ISO 12494 [47] should be carried out. An ice monitoring device, like the Combitech

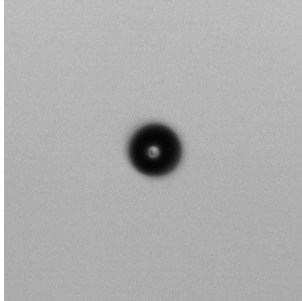


Figure 14: A $74 \mu\text{m}$ droplet detected at 04:41 on 05-02-2017.

IceMonitor [48, 49] can be used for this. This should preferably be done in combination with a third independent LWC and MVD measurement, e.g. by using rotating cylinders [23, 50]. A heated hygrometer measuring the true water content (TWC) can be used as an alternative verification of the LWC measurement when all the atmospheric water is in liquid form [34].



Figure 15: Two droplets, 19 and 62 μm in diameter detected in the same image at 16:48 on 05-02-2017.

5. Conclusions

The test using polymer microspheres confirms that the DII, calibrated by a micrometer dot scale measures the size of the tested samples correctly. The size distributions achieved by this instrument are within the tolerances specified by the manufacturer of the microspheres.

Both the CDP and the DII make precise measurements of the LWC using a 30 minute average window. Supercooled droplets with diameters above 50 μm exist in fogs where MVD is lower than predicted.

The CDP achieves higher values of the droplet diameters compared with the DII. This leads to an even higher difference in the measured LWC.

A calibration of the measurement range depending on the distance from the measured particle to the optical center is needed in order to get a better estimation of the measurement volume.

The predicted LWC and MVD data from HARMONIE-AROME have better agreement with the measured values when using a 500 meter horizontal resolution than the usual 2.5 km resolution.

No connection was observed between the wind speed and the difference in the measured LWC. The less aerodynamic shape of the DII compared with the CDP has no noticeable effect on the measurement at wind speeds as low as 1-4 $\text{m} \cdot \text{s}^{-1}$.

The DII proved to be fully operational without site attendance for four months of continuous measurement. The instrument speed and resolution seems to be good enough to detect and measure the conditions for icing. The data can be used to verify and validate NWP models.

Large droplets are important to understand the total size distribution of liquid water droplets and may play an important role during icing.

6. Acknowledgements

The authors would like to give special thanks to Patrik Jonsson, Björn Ollars and Olof Carlsson at Combitech AB for the physical integration of the two instruments and the CDP data processing and Lisa Velander at Mid Sweden University for the language check. The work was funded by the Swedish Energy Agency.

References

- [1] B. E. Kringlebotn Nygaard, J. E. Kristjánsson, L. Makkonen, Prediction of in-cloud icing conditions at ground level using the wrf model, *Journal of Applied Meteorology and Climatology* 50 (2011) 2445–2459.
- [2] L. Makkonen, Models for the growth of rime, glaze, icicles and wet snow on structures, *Philosophical Transactions of the Royal Society of London A: Mathematical, Physical and Engineering Sciences* 358 (2000) 2913–2939.
- [3] L. Makkonen, T. Laakso, M. Marjaniemi, K. Finstad, Modelling and prevention of ice accretion on wind turbines, *Wind Engineering* 25 (2001) 3–21.
- [4] M. C. Homola, M. S. Virk, T. Wallenius, P. J. Nicklasson, P. A. Sundsbø, Effect of atmospheric temperature and droplet size variation on ice accretion of wind turbine blades, *Journal of Wind Engineering and Industrial Aerodynamics* 98 (2010) 724–729.
- [5] Y. Han, J. Palacios, S. Schmitz, Scaled ice accretion experiments on a rotating wind turbine blade, *Journal of Wind Engineering and Industrial Aerodynamics* 109 (2012) 55–67.
- [6] J. H. Seinfeld, S. N. Pandis, K. Noone, *Atmospheric chemistry and physics: from air pollution to climate change*, 1998.
- [7] K. J. Finstad, E. P. Lozowski, L. Makkonen, On the median volume diameter approximation for droplet collision efficiency, *Journal of the atmospheric sciences* 45 (1988) 4008–4012.
- [8] G. Thompson, B. E. Nygaard, L. Makkonen, S. Dierer, Using the weather research and forecasting (wrf) model to predict ground/structural icing, in: 13th International Workshop on Atmospheric Icing on Structures, METEOTEST, Andermatt, Switzerland.
- [9] H. Bergström, E. Olsson, S. Söderberg, P. Thorsson, P. Undén, *Wind power in cold climates: Ice mapping methods*, Elforsk AB, 2013.
- [10] S. Rydblom, B. Thornberg, Liquid water content and droplet sizing shadowgraph measuring system for wind turbine icing detection, *IEEE Sensors Journal* 16 (2015) 2714–2725.

- [11] S. Rydholm, B. Thörnberg, Droplet imaging instrument metrology instrument for icing condition detection, in: Imaging Systems and Techniques (IST), 2016 IEEE International Conference on, IEEE, 2016, pp. 71–76.
- [12] F. Lamraoui, G. Fortin, R. Benoit, J. Perron, C. Masson, Atmospheric icing impact on wind turbine production, *Cold Regions Science and Technology* 100 (2014) 36–49.
- [13] R. G. Knollenberg, The optical array: An alternative to scattering or extinction for airborne particle size determination, *Journal of Applied Meteorology* 9 (1970) 86–103.
- [14] T. Kuhn, I. Grishin, J. Sloan, Improved imaging and image analysis system for application to measurement of small ice crystals, *Journal of Atmospheric and Oceanic Technology* 29 (2012) 1811–1824.
- [15] D. Gabor, A new microscopic principle, *Nature* 161 (1948) 777–778.
- [16] T. E. Chambers, M. W. Hamilton, I. M. Reid, A low cost digital holographic imager for calibration and validation of cloud microphysics remote sensing, in: SPIE Remote Sensing, International Society for Optics and Photonics, 2016, pp. 100010P–100010P–10.
- [17] R. Lawson, R. Cormack, Theoretical design and preliminary tests of two new particle spectrometers for cloud microphysics research, *Atmospheric research* 35 (1995) 315–348.
- [18] J. P. Fugal, R. A. Shaw, E. W. Saw, A. V. Sergeyev, Airborne digital holographic system for cloud particle measurements, *Applied optics* 43 (2004) 5987–5995.
- [19] J. Henneberger, J. Fugal, O. Stetzer, U. Lohmann, Holimo ii: a digital holographic instrument for ground-based in situ observations of microphysical properties of mixed-phase clouds, *Atmospheric Measurement Techniques* 6 (2013) 2975–2987.
- [20] V. A. Kaikkonen, D. Ekimov, A. J. Makynen, A holographic in-line imaging system for meteorological applications, *IEEE Transactions on Instrumentation and Measurement* 63 (2014) 1137–1144.

- [21] V. A. Kaikkonen, A. J. Mäkynen, A high sampling rate digital holographic imager instrument for the in situ measurements of hydrometeors, *Optical Review* 23 (2016) 493–501.
- [22] S. G. Cober, G. A. Isaac, J. W. Strapp, Characterizations of aircraft icing environments that include supercooled large drops, *Journal of Applied Meteorology* 40 (2001) 1984–2002.
- [23] L. Makkonen, Analysis of rotating multicylinder data in measuring cloud-droplet size and liquid water-content, *Journal of Atmospheric and Oceanic Technology* 9 (1992) 258–263.
- [24] N. L. Miles, J. Verlinde, E. E. Clothiaux, Cloud droplet size distributions in low-level stratiform clouds, *Journal of the atmospheric sciences* 57 (2000) 295–311.
- [25] W. R. Sand, W. A. Cooper, M. K. Politovich, D. L. Veal, Icing conditions encountered by a research aircraft, *Journal of climate and applied meteorology* 23 (1984) 1427–1440.
- [26] I. S. Organization, Iso 12181-1: 2011, geometrical product specifications (gps)-roundness-part 1: Vocabulary and parameters of roundness, 2011.
- [27] D. Marr, E. Hildreth, Theory of edge detection, *Proceedings of the Royal Society of London. Series B. Biological Sciences* 207 (1980) 187–217.
- [28] R. C. Gonzales, R. E. Woods, Digital image processing, 2-nd edition, 2002.
- [29] J. E. Dye, D. Baumgardner, Evaluation of the forward scattering spectrometer probe. part i: Electronic and optical studies, *Journal of Atmospheric and Oceanic Technology* 1 (1984) 329–344.
- [30] M. Wendisch, J.-L. Brenguier, Airborne measurements for environmental research : methods and instruments, Wiley Series in Atmospheric Physics and Remote Sensing, Wiley-VCH, Weinheim, 2013.
- [31] G. Mie, Beiträge zur optik trüber medien, speziell kolloidaler mettallösungen, *Annalen der physik* 330 (1908) 377–445.
- [32] C. F. Bohren, D. R. Huffman, Absorption and scattering of light by small particles, John Wiley & Sons, 2008.

- [33] J.-L. Brenguier, T. Bourrianne, A. A. Coelho, J. Isbert, R. Peytavi, D. Trevarin, P. Weschler, Improvements of droplet size distribution measurements with the fast-fssp (forward scattering spectrometer probe), *Journal of Atmospheric and Oceanic Technology* 15 (1998) 1077–1090.
- [34] J. K. Spiegel, P. Zieger, N. Bukowiecki, E. Hammer, E. Weingartner, W. Eugster, Evaluating the capabilities and uncertainties of droplet measurements for the fog droplet spectrometer (fm-100), *Atmospheric Measurement Techniques* 5 (2012) 2237–2260.
- [35] S. Lance, C. Brock, D. Rogers, J. Gordon, Water droplet calibration of the cloud droplet probe (cdp) and in-flight performance in liquid, ice and mixed-phase clouds during arcpac, *Atmospheric Measurement Techniques* 3 (2010) 1683–1706.
- [36] Y. Seity, P. Brousseau, S. Malardel, G. Hello, P. Bénard, F. Bouttier, C. Lac, V. Masson, The arome-france convective-scale operational model, *Monthly Weather Review* 139 (2011) 976–991.
- [37] L. Bengtsson, U. Andrae, T. Aspelien, Y. Batrak, J. Calvo, W. de Rooy, E. Gleeson, B. Hansen-Sass, M. Homleid, M. Hortal, The harmonie–arome model configuration in the aladin–hirlam nwp system, *Monthly Weather Review* 145 (2017) 1919–1935.
- [38] J. S. Kain, J. M. Fritsch, A one-dimensional entraining/detraining plume model and its application in convective parameterization, *Journal of the Atmospheric Sciences* 47 (1990) 2784–2802.
- [39] V. Masson, J.-L. Champeaux, F. Chauvin, C. Meriguet, R. Lacaze, A global database of land surface parameters at 1-km resolution in meteorological and climate models, *Journal of Climate* 16 (2003) 1261–1282.
- [40] M. Wendisch, A. Keil, A. Korolev, Fssp characterization with monodisperse water droplets, *Journal of Atmospheric and Oceanic Technology* 13 (1996) 1152–1165.
- [41] S. Lee, B. H. Kahn, J. Teixeira, Characterization of cloud liquid water content distributions from cloudsat, *Journal of Geophysical Research: Atmospheres* 115 (2010).

- [42] C. W. Ulbrich, Natural variations in the analytical form of the raindrop size distribution, *Journal of Climate and Applied Meteorology* 22 (1983) 1764–1775.
- [43] A. Jameson, A. Kostinski, What is a raindrop size distribution?, *Bulletin of the American Meteorological Society* 82 (2001) 1169–1177.
- [44] R. Shaw, A. Kostinski, M. Larsen, Towards quantifying droplet clustering in clouds, *Quarterly journal of the royal meteorological society* 128 (2002) 1043–1057.
- [45] G. Peters, B. Fischer, H. Münster, M. Clemens, A. Wagner, Profiles of raindrop size distributions as retrieved by microrain radars, *Journal of applied meteorology* 44 (2005) 1930–1949.
- [46] S. G. Cober, G. A. Isaac, Characterization of aircraft icing environments with supercooled large drops for application to commercial aircraft certification, *Journal of Applied Meteorology and Climatology* 51 (2012) 265–284.
- [47] L. Makkonen, P. Lehtonen, M. Hirviniemi, Determining ice loads for tower structure design, *Engineering Structures* 74 (2014) 229–232.
- [48] S. Fikke, G. Ronsten, A. Heimo, S. Kunz, M. Ostrozlik, P. Persson, J. Sabata, B. Wareing, B. Wichure, J. Chum, Cost 727: Atmospheric icing on structures, Measurements and data collection on icing: State of the Art, *Publication of MeteoSwiss* 75 (2006) 1422–1381.
- [49] P. Thorsson, S. Söderberg, H. Bergström, Modelling atmospheric icing: A comparison between icing calculated with measured meteorological data and nwp data, *Cold Regions Science and Technology* 119 (2015) 124–131.
- [50] D. Knezevici, R. Kind, M. Oleskiw, Determination of medium volume diameter (mvd) and liquid water content (lwc) by multiple rotating cylinders, in: 43rd AIAA Aerospace Sciences Meeting and Exhibit, p. 861.